Fernando Domingues Amaro

Ion Back-Flow Reduction in Gaseous Detectors with the Micro Hole and Strip Plate

Universidade de Coimbra

2010

Fernando Domingues Amaro

Ion Back-Flow Reduction in Gaseous Detectors with the Micro Hole and Strip Plate

Dissertation Submitted to the Faculty of Science and Technology of the University of Coimbra, for the degree of *Philosophiae Doctor* in Technological Physics, under the Supervision of Prof. Dr. Joaquim Marques Ferreira dos Santos and Prof. Dr. João Filipe Calapez de Albuquerque Veloso

Coimbra 2010

This work was supported by *Fundação para a Ciência e Tecnologia* and by the European Social Fund, through *Programa Operacional Potencial Humano* (POHP) in the form of the grant SFRH/30318/2006.

ACKNOWLEDGEMENTS

This work is much more that just the achievement of one person: it would be impossible to complete this task without the many contributions that were give, some of them not directly related with the work described in these pages, but nevertheless with great influence on its successful completion. In this way, I would like to particularly thank to:

Professor Joaquim Marques Ferreira dos Santos, for his orientation and constant encouragement that greatly motivated my work and were essential to its completion. A special thanks' for the patience and dedication in the revision of this manuscript.

Professor João Filipe Calapez de Albuquerque Veloso, for his co-orientation and insightful discussions that provided me with a better understanding of the physical processes involved in the complex world of radiation detection.

Professor Amos Breskin, for accepting me at his research laboratory during several periods that resulted in considerable progress, both personal and scientific. He was always the first to put at my disposal his immense knowledge and expertise and I'm very thankful for this.

Doctor Jorge Maia, for sharing his expertise in the initial stages of this work, a factor that greatly contributed to its success.

To Carlos Santos, for the work done on the Garfield simulations included in chapter 6.

To all the members of the Radiation Detection Lab in Israel, particularly to Rachel Chechick, Alexey Lyashenko, Marco Cortesi, Raz Alon, and Moshe Klin, for making me feel at home during the time I've spent there.

To my friends of the *Lamb Shift in the Muonic Hydrogen* collaboration. The moments I've spent between the control room, laser hut and zone will always be remembered with special care and with a feeling that is already growing inside me: "saudade". And yes, Aldo, I believe the record is still ours and, so far, no visible side effects.

To my colleagues and friends at the Grupo de Instrumentação Atómica e Nuclear: Alexandre Trindade, Ana Santos, Cristina Monteiro, Daniel Covita, Elisabete Freitas, Hugo Natal da Luz, José Matias, Liliana Carita, Luís Panchorinha, Pedro Basso and Sérgio do Carmo, for making of our lab a healthy and friendly place with all the necessary conditions for a successful work. A special thanks to Augusto Cordeiro and Carlos Carvalho, for the patience and dedication they've put in the production of the detectors and to Isabel Melo, Sónia Branco and Paulo Gomes for their support in the research activities.

À minha família, especialmente à minha mãe, que, muitas vezes com enormes sacrifícios, tudo fez para garantir o bem-estar dos seus filhos. É uma divida que sei que nunca poderei saldar, mas aqui fica um agradecimento muito especial.

To Sandra, for all the stolen sunny afternoons hidden in these pages. You have always been a source of inspiration and I can only say that I'm very lucky for having you by my side.

ABSTRACT

We've developed and tested a set of techniques for the reduction of the ion back flow in cascaded gaseous detectors. These techniques have in common the fact that they make use of the properties of the Micro-Hole and Strip plate, a micro-patterned gas electron multiplier that presents two sets of strip electrodes on one of its surfaces.

On a first approach to the problem of the ion back-flow reduction in gaseous detectors the Micro-Hole and Strip Plate was operated in reverse mode, trapping a fraction of the ions produced in the detector at its electrodes. The results have proven the efficiency of this method in trapping the ions in gaseous detectors but fell short in respect to the charge gain achievable. Nevertheless the validity of the method was proven and the work done opened the way to further improvements and developments.

Another approach that we've tested exploits the production of secondary scintillation at the Micro-Hole and Strip Plate when operating in noble gases and CF_4. In the detector developed, the Photon Assisted Cascaded Electron Multiplier, the propagation of the electric signal through the detector is mediated by UV photons and the transference of electric charges is partially blocked. We've proven the PACEM concept and compared several gas mixtures in respect to the optical gain and to the ion back flow reduction achievable.

We've also developed and tested a new thick electron multiplier, the THCOBRA, which merges the properties of the Micro-Hole and Strip Plate with the ones of the thick electron multipliers. We've established its operation as a gaseous electron multiplier operating in several gases and incorporated it into the PACEM detector, replacing the MHSP in the production of the secondary scintillation.

SUMÁRIO

Neste trabalho desenvolveu-se um conjunto de técnicas com vista à redução do fluxo de iões em detectores gasosos compostos por cascatas de multiplicadores de electrões. Estas técnicas têm em comum o facto de utilizarem as propriedades da "Micro-Hole and Strip Plate", uma microestrutura que possui numa das suas faces dois tipos de eléctrodos independentes.

Numa primeira abordagem ao problema da redução do fluxo de iões em detectores gasosos a "Micro-Hole and Strip Plate" foi operada em modo reverso, com os seus eléctrodos polarizados de forma a capturar os iões positivos produzidos no detector. Os resultados obtidos demonstraram a eficácia deste método para capturar os iões positivos mas simultaneamente observou-se uma redução significativa do ganho em carga do detector.

Uma outra abordagem testada passou pelo desenvolvimento de um novo tipo de detector, que explora a cintilação secundária produzida na "Micro-Hole and Strip Plate" durante as avalanches de electrões que ocorrem na região entre os seus eléctrodos quando esta opera em gases nobres e CF_4. No detector desenvolvido, "Photon Assisted Cascaded Electron Multiplier", a propagação do sinal eléctrico pela cascata de multiplicadores gasosos é mediada pelos fotões UV e a transferência de carga eléctrica é bloqueada. Demonstrámos a exequibilidade do conceito de transferência de sinal por meio da cintilação secundária e comparámos várias misturas gasosas relativamente ao ganho óptico e ao número de iões positivos que retrocede no detector nestas misturas.

Foi também desenvolvido e testado um novo multiplicador gasoso do tipo "thick electron multiplier", a THCOBRA. Avaliámos as suas propriedades como multiplicador gasoso de electrões, tendo obtido ganhos relativamente elevados em várias misturas gasosas, e aplicámos esta nova estrutura ao conceito do "Photon Assisted Cascaded Electron Multiplier", tendo esta substituído a "Micro-Hole and Strip Plate" na produção de cintilação secundária.

CONTENTS

LIST OF FIGURES

LIST OF ACRONYMS

Ea: Electron affinity

Eg: Band Gap Energy

GEM: Gas Electron Multiplier

GPM: Gas Avalanche Photomultiplier

GSPC: Gas Proportional Scintillation Counter

IBF: Ion Back Flow Fraction

IISEE: Ion-induced secondary electron emission

MICROMEGAS: Micromesh Gaseous Detector

MCA: Multi-Channel Analyzer

MHSP: Micro hole and Strip Plate

MSGC: Micro Strip Gas Counter

MWPC: Multi-wire Proportional Chamber

PC: Photocathode

QE: Quantum Efficiency

RICH: Ring Imaging Cherenkov

THGEM: Thick Gas Electron Multiplier

TPC: Time Projection Chamber

VUV: Vacuum Ultra Violet

1 INTRODUCTION

1.1 Purpose of the work

Modern science is, as never before in its history, dependent on the development of scientific tools for progress. Experimental apparatus has grown, going far beyond the human size, and reaching a complexity level that requires dedicated facilities, some of them stretching outside the man made political borders. The current trend in the experiments taking place in accelerators over the world is to achieve higher rates and higher energies that require from the detector and electronics involved in the detection the ability to deal with the immense amount of events generated. The presence of the positive ions on the detectors is recognized as a major drawback to their efficient operation and intense research is being done to suppress or prevent them from reaching the sensitive areas of the detector.

The main objective of these investigations was to develop a set of techniques to efficiently block the ions that are produced during the charge multiplication avalanches in gaseous detectors and that return to the sensitive volume of the detector.

Since the primary charge deposited in a gaseous detector by an ionizing radiation is typically too low to be directly detected, these detectors rely on amplification mechanisms in the gas medium to produce a measurable output signal. The primary

electrons are collected and proportionally amplified by charge impact ionization mechanisms until their number is above the threshold for detection. In this process a large number of ion-electrons pairs are produced and, while the electrons are quickly collected at the anode of the detector and constitute the output signal, the positive ions are left behind and slowly flow in the opposite direction, until they reach the sensitive regions of the detector. The presence of the ions in these regions can affect the detector normal operation, depending on the amount of positive ions produced. In Time Projection Chambers, that require a uniform drift field to provide accurate timing and tracking information, the accumulation of the ions in the drift region can affect the electric field homogeneity, producing non-uniformities and causing track distortion. The development of detectors such as Gaseous Photo Multipliers equipped photocathodes sensitive to the visible region of the spectra, that are highly sensitive to the presence of the positive ions, is also a topic in urgent need of strong ion back-flow suppression techniques. The impact of positive ions on the sensitive photocathodes that equip these detectors results on their fast ageing and eventual damage, compromising the long term operation of the detector and limiting its performance.

Throughout this thesis we will present several strategies to achieve the reduction of the ion back flow in gaseous detectors to acceptable levels. All the techniques developed make use, one way or another, of the properties of the Micro-Hole and Strip Plate, a micro-patterned detector that was originally developed as an electron multiplier.

A first approach to the ion back flow reduction problem exploits the differences in the drift and diffusion movement of electrons and ions in order to decouple their paths and trap the positive ions at the electrodes of the Micro Hole and Strip Plate, using appropriate electric field configurations. This was done by innovating in the way the electrodes of the Micro-Hole and Strip Plate are used, introducing the reverse mode operation of the Micro-Hole and Strip Plate. The results obtained and further developments in this field are described in chapter 4.

Another approach that we've tested exploits a property of gaseous detectors that operate in highly scintillating gases, such as the noble gases and CF_4. It is a well known fact that these gases emit a copious amount of VUV photons whenever electrons are accelerated through them. It is also well known that VUV scintillation can be detected with a photo-sensor made of a thin film of CsI in direct contact with the detection gas.

The innovative feature implemented in this thesis was the use of the scintillation produced in the Micro-Hole and Strip Plate in combination with a CsI photocathode to transfer the signal between successive multiplier elements, instead of using electric fields, as it is usually implemented in cascaded gaseous multipliers. In this detector, the Photon Assisted Cascaded Electron Multiplier (PACEM), the transfer of charges (both electrons and positive ions) from the first element of the detector to the next one is completely blocked and the signal propagation between these two elements is mediated by the VUV photons emitted during the electron avalanches that take place on the first one. In chapter 5 we detail the work done concerning this technique, proving its efficiency in reducing the amount of ions that flow to the drift region of the detector without compromising the overall detection efficiency.

In chapter 6 a new patterned detector based on the thick electron multiplier technology, the THCOBRA, is tested for the first time. The THCOBRA is a thick-electron multiplier version of the Micro-Hole and Strip Plate and inherits some of its operational features while at the same time presents an increase in its robustness and easiness in production. Its operation as a charge electron multiplier is established and its application to the PACEM detector, operating in noble gases, is demonstrated in chapter 6.

The work presented in this thesis resulted so far in the publications listed below:

- "*The Thick-COBRA: a New Gaseous Electron Multiplier for Radiation Detectors*" F. D. Amaro, C. Santos, J. F. C. A. Veloso, A. Breskin, R. Chechik, J. M. F. dos Santos; accepted for publication, JINST.
- "*High pressure operation of the Photon-Assisted Cascaded Electron Multiplier"* F. D. Amaro, J. F. C. A. Veloso, J. M. F. dos Santos, A. Breskin, R. Chechik, A. Lyashenko; IEEE Transactions on Nuclear Science 56-3 (2009) 1097-1101.
- "*The Photon-Assisted Cascaded Electron Multiplier operation in CF_4 for ion backflow suppression"* F. D. Amaro, J. F. C. A. Veloso, J. M. F. dos Santos, A. Breskin, R. Chechik, A. Lyashenko; IEEE Transactions on Nuclear Science 55-3 (2008) 1652-1656.
- *"PACEM: a New Concept for High Avalanche-Ion Blocking"* J. F. C. A. Veloso, F. D. Amaro, C. D. R. Azevedo, J. M. F. dos Santos, A. Breskin, A. Lyashenko,

R. Chechik; Nuclear Instruments and Methods in Physics Research Section A 581 (2007) 261-264.

- *"The Photon-Assisted Cascaded Electron Multiplier: a concept for potential avalanche-ion blocking"* J. F. C. A. Veloso, F. D. Amaro, J. M. F. dos Santos, A. Breskin, A. Lyashenko, R. Chechik; Journal of Instrumentation 1 P08003 (2006).
- *"MHSP in reversed-biased operation mode for ion blocking in gas avalanche multipliers"* J. F. C. A. Veloso, F. D. Amaro, J.M. Maia, A.V. Lyashenko, A. Breskin, R. Chechik, J. M. F. dos Santos, O. Bouianov, M. Bouianov; Nuclear Instruments and Methods A 548 (2005) 264-261.

And was part of the manuscript:

- *"Secondary scintillation yield from gaseous micropattern electron multipliers in direct Dark Matter detection"* C.M.B. Monteiro, A.S. Conceição, F. D. Amaro, J.M. Maia, A.C.S.S.M. Bento, L.F.R. Ferreira, J. F. C. A. Veloso, J. M. F. dos Santos, A. Breskin, R. Chechik; Physics Letters B 677, Issue: 3-4 (2009) 133-138.

2 SCIENTIFIC BACKGROUND

2.1 Physical processes

The field of radiation detection is a complex one and requires from its intervenient a detailed knowledge of the process implicated. In this chapter we will provide a small introduction to the subject of radiation detection with the purpose of clarifying some of the aspects concerning the practical operation of the detectors developed in this work.

Some of the characteristics of gaseous detectors that make them so attractive are the relatively low cost and fact that these detectors can be constructed with large volumes. These detectors are typically operated as amplifying devices, detecting a small amount of charge deposited in the detecting medium and turning it into a signal passive of efficient detection. The physical processes involved in this achievement are the conversion of the energy of the incident radiation into the primary charge, the efficient collection and amplification of the primary charge and finally the detection of the resulting amplified charge. In the following sections we will give a brief introduction to these topics.

2.1.1 Absorption in the gas and interactions with matter

The interactions between the incident radiation and the atoms or molecules of the gas medium, taking place within the sensitive volume of the detector, are strongly dependent on the type and energy of the radiation to be detected. With respect to its

nature, ionizing radiation can either be charged (such as alpha particles or fast electrons) or devoid of charge (neutrons and photons) and this division has a strong influence on the type of interactions that take place inside the detector.

Heavy charged particles interact mostly through Coulomb force with atomic electrons and the products of the interaction are excited or ionized atoms and free electrons from the ionization processes [1]. When the charged particle enters the detection medium it interacts with the electrons of the medium and in each of these interactions the charged particle losses a very small fraction of its energy suffering almost no change in its direction. The charged particle goes through the detector in an almost straight line, continuously losing energy and slowing down, until the very end of its track, when most of the energy of the particle is lost. In each interaction there is the probability of exciting or ionizing the electrons of the gas medium and as a consequence a track of electrons-ions pairs and excited atoms is created, marking the path of the particle in the detector. If the detector is dimensionally scaled to match the energy of the incident particle there will be a high probability that all its energy will be transferred to the detection medium. In cases where the density of atoms/molecules of the detection medium is not enough to fully absorb all the particle energy, it may not loose all its energy inside the detector, leaving only a partial signature of its passage through it. In both cases, either full or partial absorption, the passage of a charge particle through the detector leaves behind a track of excitations and ionizations that signal the path of the particle in the detector.

A different type of interaction takes place between non charged radiation (photons and neutrons) and the atoms or molecules of the detection medium. In this case the ionizing radiation interacts with the detection medium in a so-called catastrophic interaction: either being fully absorbed, with its energy completely transferred, or suffering a large scattering and losing a considerable fraction of its energy in a single event. In both cases, the path of the radiation suffers a large disruption and the energy is transferred to the region surrounding the interaction point and not distributed in a linear track as it is the case with heavy charged particles.

Photons interact with the detection medium via three major mechanisms: photoelectric effect, Compton scattering and pair production. The probability of interaction for each of these mechanisms depends on the detection media and is presented in figure 2.1 for

X-rays in the energy range from 1 keV to 10 MeV interacting in xenon (a noble gas extensively used in this work).

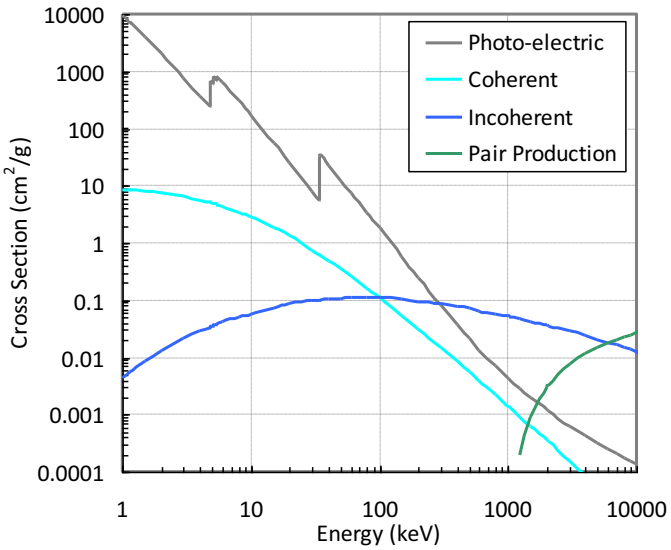

Figure 2.1 - Cross sections for photoelectric effect, coherent and incoherent (Compton) scattering and pair production for X-rays in xenon [2].

The pair production is an inexistent phenomena for photons in the energy range used in this thesis (up to some tenths of keV) occurring only for energies above the threshold of 1022 keV. For more information on this mechanism, the reader is referred to the text book [3].

Compton scattering occurs between the incident photon and an electron of the atom. In this process the photon suffers a deflection from its initial direction and transfers a fraction of its energy to the electron that is ejected from the atom and becomes what is known as a recoil electron. This recoil electron can be emitted with energy in a large energy range, from zero to a significant portion of the photon energy.

For low energy gamma rays and X-rays the major interaction mechanism is the photo-electric effect. In this interaction, the incident photon is completely absorbed by the atoms of the medium and an electron is emitted from the atom, carrying the excess energy corresponding to the difference between the energy of the incident photon and the binding energy, E_B, of the electron in the atom [3]:

$$E_{photoelectron} = h\nu - E_B \quad (2.1)$$

The atom is left in an excited state, with a vacancy in one of its bound shells, and quickly absorbs a free electron from the medium or undergoes a rearrangement process with the electrons from other shells of the atom occupying the inner vacancies. In these processes one or more Auger electrons may be emitted or else characteristic X-ray photons are emitted. While in most cases the radiation emitted is rapidly absorbed in the nearby atoms of the medium, in some cases the X-ray can escape the detector, carrying a fraction of the energy of the incident radiation. This fraction of the energy of the initial photon is not absorbed by the detector and gives rise to the escape peak, a characteristic feature of the absorption spectra obtained with low density detectors as are the gaseous ones.

As the result of the detection of a single photon, a cloud of electron/ion pairs is formed centred at the interaction point. Whenever photons are emitted as a beam the number of photons per unit area in the beam as it traverses the detector follows the typical absorption curve:

$$I = I_0 \times e^{-\mu \times d} \quad (2.2)$$

Being I the number of photons not absorbed in the medium after a distance d, and I_0 the initial number of photons penetrating the absorber. μ is the linear attenuation coefficient, a parameter that translates the probability per unit path length that a photon is removed from the beam. The mean free path, corresponding to $1/\mu$, represents the average distance traveled before an interaction takes place.

In all the processes described above the final result of the absorption of the radiation in the detector is the production of a cloud constituted by ion-electron pairs and atoms in excited states. This cloud is located around the interaction point but an additional process, not yet mentioned, contributes to its spreading. When a large amount of energy is transferred in a single ionization, the electron emitted may have energy high enough to promote new ionizations or excitations in the vicinity of the region were it was initially created. These electrons, the *δ-rays*, carry a significant portion of the energy of the primary particle away and can themselves promote new excitations and ionizations, in a process that only stops when the energy of all electrons produced becomes

equivalent to the thermal energy of the medium. These *δ-rays* have a short range and are easily absorbed in the detector but nevertheless they are responsible for the production of a considerable number of effects in the detector, particularly excitations, giving a strong contribution to the spreading of the initial cloud.

In the processes described above the minimum energy to be transferred from the incident radiation to the gas medium corresponds to the ionization potential of the atom or molecule. But not all the incident energy is converted in ionizations: some energy is spent in excitations that do not contribute, directly, to the production of ion-electron pairs. Therefore the energy required to produce in average one ion-electron pair, the *w value*, is always superior to the potential energy of the gases to be considered. For most of the gases with interest to radiation detection the *w value* is around 20-35 eV/ion pair [3].

Table 2.1: *w* value for some of the gases with relevance to gaseous detectors [3][4].

Element	w value (eV / Ion pair)
argon	26
xenon	22
neon	36.3
krypton	24
nitrogen	34.4
CH_4	27.3

For instance, in xenon, considering the 5.9 keV X-ray emitted by a Fe^{55} radioactive source, in average ≈ 268 ion pairs are produced for each photon fully absorbed in the detector. For each gas the number of ion-electron pairs produced by the incident radiation (the primary charge) is proportional to the energy of the radiation and too small to be directly detected. Therefore gaseous detectors rely on the collection of the primary electrons and on its multiplication to produce a measurable output signal that is proportional to the energy absorbed in the detector. The basic principle behind charge detection in gaseous detectors is the use of electric fields to separate and collect the electric charges produced by the passage of the ionizing radiation. These electric fields cause the charges to move in opposite direction, the electrons moving towards the anode

and the ions to the cathode and allows for an efficient separation of charges, preventing the loss of information that occurs with the recombination of these charges. During their movement along the field lines in the detector, electrons and ions will undergo a series of collisions with the atoms and molecules of the medium and the outcome of these collisions will ultimately depend on the energy they have at the time the collision takes place. This energy is supplied from the electric field and is therefore dependent on its intensity.

2.1.2 Drift movement

Once the primary cloud is created, the ion-electron pairs will be subject to the thermal diffusion movement characteristic of gases. During this diffusion motion the charges recently created are subject to collisions with either the neutral atoms of the gas or with the charge themselves that can result in information loss due to recombination between ions and electrons.

In order to conserve all the information on the energy of the incident radiation an electric field is applied in the region where the interaction takes place that separates the positive charges from the negative ones, preventing their recombination and superimposing a drift movement on the natural diffusion movement of the charges.

During the drift movement through the gas the electrons are continuously accelerated by the electric field and scatter with the gas atoms or molecules. If the electrons kinetic energy is low, the collision is simply elastic, without significant energy transfer from the electron to the gas atom, being the main effect of the interaction a change in the direction of the electron that keeps being accelerated by the electric field.

Once the electron energy reaches the threshold for inelastic collisions (corresponding to the amount of energy necessary to promote a change of state in the atom or molecule) a different kind of collision occurs, with transfer of the energy from the electron to the atom. After this collision the electron is once again accelerated by the electric field, increasing its energy, until a new collision takes place. This succession of microscopic inelastic collisions is the source of the macroscopic constant drift velocity with which the electron cloud drifts through the gas.

For electrons moving in a gas, the drift velocity is dependent on the electric field and can reach values as high as 10^5 m/s in methane [3]. For some gases the drift velocity

presents a broad maximum: a region where the drift velocity doesn't change much when the electric field is altered and that is usually picked as operation point to prevent instabilities due to voltage, temperature and pressure changes [5].

A precise knowledge of the drift velocity is one of the requisites for the operation of the drift chamber detector. This type of detectors makes use of the information on the time of the arrival of the particle, t_0, given by an external trigger (usually a fast scintillator) and on the time of the collection of the electrons at the anode, t_1, to provide information on the distance of the interaction point to the anode, x,:

$$x = \int_{t0}^{t1} v \, dt \tag{2.3}$$

Typical collection times in drift chambers are in the order of some μs, the so-called memory or dead time of the detector that can be reduced by choosing gases with high drift velocity.

2.1.3 Secondary scintillation mechanisms in noble gases

When operating a detector in pure noble gases a new phenomena, the emission of electroluminescence by the atoms of the gas, takes place above a certain threshold value of the electric field, E_{SCINT}. Above this threshold the electrons acquire a kinetic energy that is sufficient to create excited states in the atoms of the gas:

$$e + A \rightarrow e + A^*$$

Some of these excited states, A^*, have a short lifetime, in the order of some nanoseconds, and decay to the ground state with emission of a single resonance line:

$$A^* \rightarrow A + h\upsilon_R$$

This resonance radiation is quickly re-absorbed by the atoms of the gas medium, being trapped in re-absorptions and re-emissions in a process of radiation retention [1].

Some of the excited atomic states produced by electron impact are long-lived, metastable with a decay time of several tenths of μs [6]. During this time the excited atoms can interact with other atoms, in a process that is favored at higher pressures, and form an excimer or temporary molecule that decays through the emission of a continuum of radiation, $h\nu_C$, with energies below the resonant line and that therefore are not re-

absorbed in the gas. This mechanism is considered to be the main source of secondary scintillation[a] in noble gases, especially at high pressures [6] [7].

In the noble gases this radiation is emitted in two different wavelengths bands, referred to as the first and second continua, with the emission of the second continua being favoured relatively to the first with the increase in the pressure of the gas medium; at pressures near atmospheric pressure only the second continuum is present.

The emission of secondary scintillation by noble gases is exploited in the novel detectors developed in this thesis but has already been exploited in many other gaseous detectors [8][9][10][11]. This mechanism is dependent on the value of the electric field in the detector; taking place only above a certain threshold.

Table 2.2: Typical values of the threshold for scintillation in some noble gases along with the wavelength of the second continua (dominant at atmospheric pressure) [12][13]

Element	Second continua wavelength (nm)	E_{SCINT} threshold ($V \times cm^{-1} \times torr^{-1}$)
argon	128	0.86
xenon	172	1
krypton	148	0.71

In the movement of the electrons through the gas not all the energy supplied to the drifting electrons is converted into electroluminescence. Between each inelastic collision, that results in excitation of the atom, a large number of inelastic collisions (as much as 10^4 [14]) takes place. Despite the fact that the energy loss by the electron in each of these collisions is almost negligible, the large amount of this type of collisions that takes place contributes to the dissipation of some of the energy supplied by the electric field. Noble gases are particularly good scintillation emitters, converting with high efficiency the energy supplied by the electric field to the drifting electrons into scintillation. The conversion of this energy can reach values up to 80% in xenon and in argon [12] [15].

[a] the term secondary scintillation (sometimes employed as an alternative to electroluminescence) is used to distinguish it from the primary scintillation emitted during the interaction of the particle in the gas.

Xenon is one of the mostly used gases in gaseous detectors based in scintillation mechanisms and is extensively used in this thesis. At low pressure the secondary emission spectrum is composed by 2 lines at 120 and 147 nm, corresponding to the resonance line and the first continua [16] [17]. The formation of excited dimmers is favoured with the increase in pressure and above 10 mbar the emission is predominantly done by these excited molecules and composed by the two continua centred at 147 and 172 nm. For atmospheric pressures the second continua (centred at 172 nm) becomes dominant and most of the emission in xenon is done at this wavelength [18]. In other noble gases, Argon and Krypton, the second continua are located at 128 and 148 nm, respectively [19].

Another relevant value of electric field in gaseous detectors is the threshold for ionization, E_{IONIZ}: above this value the energy supplied by the electric field to the drifting electrons is high enough to promote the ionization of the gas atoms and a new mechanism is available for the electrons to dissipate their energy. The energy that is spent in the ionizations cannot be used in the production of electroluminescence and the values of conversion efficiency mentioned above for the noble gases drop.

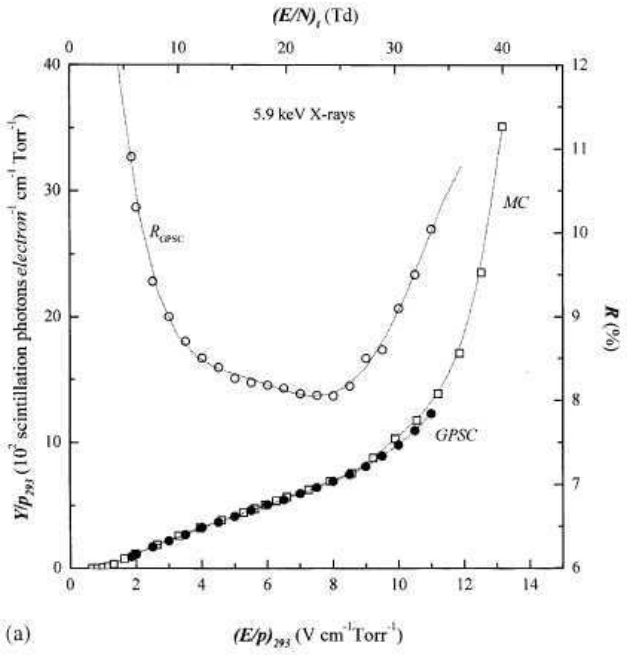

Figure 2.2 - Scintillation yield in xenon (solid circles, left axis) and energy resolution (open circles, right axis) of a GSPC. Squares indicate Monte Carlo simulations [20].

Nevertheless the total output of secondary scintillation emitted by the gas atoms increases since more electrons contribute to the electron cloud and are available to the production of electroluminescence. In figure 2.2 we present the scintillation yield, i.e. the number of photons emitted per primary electron, as a function of the electric field in a detector based in scintillation mechanism, the Gaseous Scintillation Proportional Counter (GSPC) [8] [9]. For a value of electric field intensity under E_{SCINT} no secondary scintillation is measured while for values above E_{IONIZ} the scintillation yield increases exponentially, reflecting the avalanche grown of the electron cloud.

The scintillation yield is a gas dependent parameter that follows a linear trend for values of electric field between the thresholds for scintillation and ionization (E_{SCINT} and E_{IONIZ}). In this region of electric field the number of photons emitted for each primary electron drifting in the gas is given by the formulas (for xenon and argon respectively):

$$\eta = 140 \times (E/p - 0.83) \times p \times \Delta x \quad [18] \tag{2.4}$$

$$\eta = 81 \times (E/p - 0.58) \times p \times \Delta x \quad [21] \tag{2.5}$$

In the formulas above, *E/p* is the reduced electric field and is given in units of $kV \times cm^{-1} \times bar^{-1}$, *p* is the pressure and Δx the distance travelled by the primary electrons (in units of bar and cm, respectively).

2.1.4 Quenching mechanisms

The scintillation mechanisms that take place in noble gases are the source of a large amount of photons emitted by the gas molecules and will be exploited in the some of the detectors described in thesis. These photons are emitted in the VUV range with energies of a few eV and can induce secondary effects when interacting with the metallic parts (the walls or electrodes) of the detector. Interactions of the type:

$$h\upsilon + \text{wall} \rightarrow e^{-}$$

with the emission of photon induced electrons are favored by the low work function of metals (aluminum and copper present work functions of 4.08 and 4.7 eV respectively [22]). The electrons emitted in these processes have a non-negligible probability of reaching the regions of the detector were the avalanches develop and trigger delayed pulses causing what is know as *photon feedback*.

This effect is suppressed in charge amplification detectors with the inclusion of an additive to the noble gas. This additive is usually a complex molecular gas (commonly CH_4) with several degrees of freedom and lower ionization energy that the noble gas and is included in the gas mixture in small percentages, acting as a *quenching gas*.

The quenching molecules have higher cross section for photo-absorption that for photo-emission and are therefore very efficient in the absorption of the photons emitted by the noble gases. The energy absorbed can be dissipated in a variety of mechanisms other that the emission of radiation and in some cases leads to ionization of the quenching molecule with production of additional charge [6]. The inclusion of even a small percentage of a quenching gas can fully suppress the secondary scintillation emitted by the noble gas and prevent the occurrence of the photon feedback.

2.1.5 Ionization and charge production mechanisms

When the electric field is above the ionization threshold of the gas, a new series of mechanisms becomes available for the accelerated electrons to dissipate the energy supplied by the electric field. In this region of operation, inelastic collisions that result in ionization of the gas atoms start taking place and an increase in the number of electrons in the electron cloud is observed.

The most significant mechanism for charge production in noble gases detectors is the ionization by electron impact:

$$e^- + A \rightarrow A^{*+} + e^- + e^-$$

The extracted electrons, resulting from the ionizations of the gas atoms, join the poll of electrons available to promote new excitations in the gas, leading to an exponential rise in the total amount of electrons in the electron cloud. The number of secondary electrons produced per unit path length by each electron that constitutes the electron cloud is the *Townsend coefficient*, α. This coefficient is dependent on the nature of the gas and on the electric field applied and dictates the avalanche growth when the electron cloud travels a path x in the detector:

$$n = n_0 \times e^{\alpha \times x} \tag{2.6}$$

The gas gain, M, is an important parameter in gaseous detectors and, for uniform electric fields where α is constant, is given by [23]:

$$M = n/n_0 = e^{\alpha \times x} \tag{2.7}$$

Although mathematically there is no limit to the value of M it is know that the maximum number of electrons in an avalanche is empirically limited to 10^7-10^8, a value known as the Raether limit [23] and that sets a physical limit to the maximum gas gain achievable in gaseous detectors.

2.2 Gaseous detectors

2.2.1 The proportional counter and the multiwire chamber

Proportional counters are the simplest gaseous detectors with charge multiplication and appeared initially in the shape of parallel plates with a small gap filled with a gas between them. Using an appropriate electric field between these two plates it is possible to collect and/or amplify the charge deposited in the gap between the plates by ionizing radiation. The parallel plate geometry, despite being still widely used actually presents the inconvenient that, since the electric field in the gap between the plates is uniform, the amplification that primary electrons are subjected is dependent on the distance of the point of interaction to the anode of the detector. This drawback was overcome with the introduction of the cylindrical proportional counter, composed by a metallic cylindrical container with a thin (some tens of μm) wire at its axis. The electric field inside this detector presents a radial dependence, and only in the small region at the vicinity of the central wire (that acts as anode, collecting the electrons) the electric field reaches values above the threshold for multiplication. The primary electrons produced in the detector simply drift through the low field regions until they reach the close vicinity of the anode were they suffer the multiplication processes described in the previous sections [3].

A remarkable advance took place in 1968 with the introduction of the Multi-Wire Proportional Chamber (MWPC) by Georges Charpak. The MWPC is an extended version of the proportional counter in the sense that is composed of several thin wires placed at a short distance apart. The MWPC can cover large areas and, by measuring the charge collected at each anode, allows the electronic readout of particle tracks inside the

detector. Soon the MWPC became the work horse of most high energy experiments, a position that more than justified the attribution of the Nobel Prize in Physics to its inventor.

Soon after the invention of the MWPC it became clear that this detector could be used to determinate the distance from the interaction point to the collecting anode. This is done with the accurate knowledge of the drift velocity and of the interaction time in the detector. The stacking of several MWPC, with the wires perpendicular to each other, gave the possibility to obtain 3D spatial localization of the particle track in the detector and made of the drift chambers very popular detectors.

2.2.2 Time projection chambers

Time Projection Chambers (TPC) are virtually at the heart of many high energy physics experiments currently taking place or being planed. These detectors are usually composed by a long (up to a few meters) cylindrical volume filled with gas and with a perfectly uniform electric field that is fitted around the accelerator beamline [24].

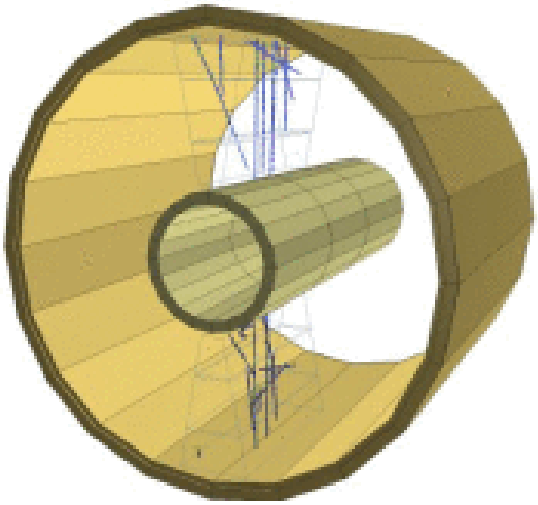

Figure 2.3 - One of the first cosmic ray events recorded and reconstructed in two sectors of the ALICE time projection chamber [26].

The collisions that take place in the accelerator produce a jet of particles that are detected in the gas volume of the TPC and whose tracks drift through the detector, under the influence of the uniform electric field, to the readout pads placed at the caps

of the TPC. The readout is usually done with MWPC, that amplify and collect the primary electrons, but the current trend is for the replacement of MWPC by micro-patterned detectors, either GEM, THGEM or Micromegas [25].

The ions produced at the readout elements slowly drift back to the detection volume and accumulate in the sensitive volume of the detector, distorting the uniform electric field and causing major dynamic track distortions [27]. The presence of the positive ions was soon realized to be a problem [28] and most TPC designs included a gated electrode to trap the ions.

2.2.3 Gas scintillation proportional counter

The operation of the Gas Scintillation Proportional Counter (GSPC) [8] [9] is based on a completely different mechanism that the one of the detectors described so far. These detectors are usually composed by a drift region, were the primary charge is produced and were the electric field intensity is below the excitation threshold of the gas. Under the influence of this low electric field the primary electrons cloud simply drifts until it reaches the scintillation region of the detector, separated from the drift region by a metallic mesh. The electric field in the scintillation region has a value between the thresholds for excitation and ionization of the gas. Once the electron cloud enters this region of the detector, all the energy that the primary electrons take from the electric field is spent in excitations and no changes occur in the number of drifting electrons. As it was described above, the efficiency with which the energy supplied from the electric field is converted in secondary scintillation is very high, reaching values above 80% in the noble gases. This energy is emitted in the form of a large amount of VUV secondary scintillation photons that are detected by an appropriate sensor, usually a photo-multiplier tube although other photo-sensors can be employed [11]. These detectors benefit from the low statistical fluctuations in the number of secondary scintillation photons produced by the electrons drifting in the scintillation region and present very good energy resolution.

2.2.4 Gas electron multiplier

The development of UV photo-lithography techniques and its application to the radiation detection science allowed the development of the family of micro-patterned gaseous detectors. One of these, the Gas Electron Multiplier (GEM), was developed by

Fabio Sauli at the CERN [29] and is made of a thin insulating copper claded polymer (Kapton®) foil. The lithography process used in the production of the GEM removes part of the copper leaving some regions of the polymer foil exposed. The foil is then submitted to a wet chemical etching process that removes the exposed polymer, leaving the regions protected with copper intact. Usually a mask with circular openings disposed in an hexagonal pattern is used in the lithography process and the result after the wet etching step are a series of bi-conical holes in the polymer foil as it is showed in figure 2.4.

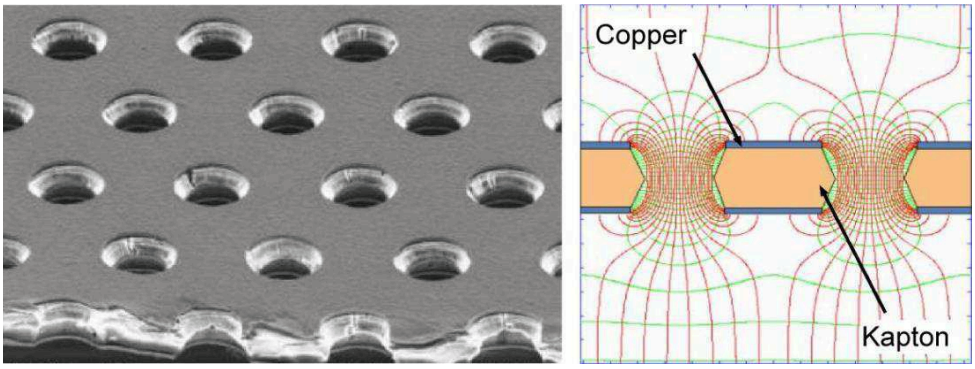

Figure 2.4 - Micro photography of a GEM foil and schematics of its operation (images from CERN GDD group [30]). GEM are usually manufactured from 50 μm thick polymer foils and the etching process produces holes with 80 μm and 60 μm diameter in the metal and in the polymer, respectively.

The application of a suitable voltage difference between the two electrodes of the GEM allows the establishment of a dipolar electric field inside the holes of the polymer foil. This electric field reaches values well above the threshold for charge multiplication in some gases and any charge that enters one of the holes of the GEM will be strongly amplified, in certain situations by factors above 100.

If an appropriate drift field is established in the region adjacent to the GEM, any charge produced by the interaction of ionizing radiation can be guided into its holes and amplified inside them. The establishment of another electric field, the extraction field, on the other side of the GEM foil assures the extraction of the resulting charge and facilitates its transport to a readout electrode or, and this is an unique property of this type of detectors, to another multiplicative element. One of the first applications of the GEM was the coupling to a sensitive Micro Strip Gas Chamber (MSGC), acting as a

pre-amplifying element (thus reducing the necessary voltages applied at the MSGC) in the HERA-B inner tracker System [31].

Another exciting feature of the GEM and other hole multipliers is the fact that the electron avalanches only occur in the region inside the holes, confining them to a small region of the detector. This is of particular interest when operating in pure noble gases. These gases emit, as we've seen, a copious amount of scintillation. Some of this photons have energy above the work function of the typical metallic constituents of the detector body (aluminum walls and copper electrodes mostly) and can promote the occurrence of photon feedback in the detector. This effect is one of the reasons that led to the inclusion of gases with quenching properties in noble gases mixtures: to suppress the scintillation emitted by the noble gas atoms. In the traditional wire detectors, such as the proportional counter, the avalanches take place in the open space near the vicinity of the detector leaving a lot of open space for UV photons to spread in all directions, causing positive feedback mechanisms in the detector. The introduction of the hole multipliers strongly reduced the occurrence of photon-feedback, since in this type of multipliers the avalanche is limited to the region inside the holes, hiding it from most of the detector. This allowed for higher gains to be achieved with GEM based detectors operating in noble gases [32] and triggered some interesting applications, particularly at cryogenic temperatures and in the development of gas avalanche photomultipliers (GPM) [33].

2.2.5 Cascaded gas electron multipliers

One of the most attractive features of the GEM (and that is also shared by other hole multipliers detectors) is the possibility of stacking several elements in a cascade of electron multipliers. The charge produced in each of the individual elements is transferred to the next one were it is further multiplied resulting in an overall higher gain across the detector. The individual elements can be operated at lower voltages that the ones used in single mode, resulting in increased stability and lower probability of breakdown in the detector.

In these detectors the electron cloud keeps growing while going from one multiplicative element of the detector to the next one and most of the charge is produced at the last element of the cascade. This effectively optically hides the last avalanches from the drift region of the detector, strongly reducing the photon feedback in these detectors and

allowing for the efficient operation of gas avalanche photomultipliers (GPM) coupled to photocathodes sensitive to the UV [33] [34].

The occurrence of secondary avalanches caused triggered by ions, the *ion feedback*, is also intrinsically reduced in cascaded gas electron multipliers: the ions that are produced in the last stage of the detector (where most of the avalanches that place) have to cross all the previous elements in order to reach the sensitive region of the detector and in this process a significant fraction of the ions ends up by being trapped at the several electrodes of the detector [35].

Despite these advantages the operation of double and triple GEM detectors is not without some constrains. Although the charge multiplication inside the holes of a GEM is controlled by the voltage across them (ΔV_{GEM}), the effective charge gain is dependent on the efficiencies with which the electrons are focused in the GEM holes and extracted from them. For a certain ΔV_{GEM}, an efficient focusing of the electrons in the GEM holes is favoured by low electric fields at the entrance of the holes while the extraction off the resulting charge from them is favoured by large fields at the exit of the holes. In a cascade of GEM the two conditions above are conflicting, since the electric field E_2 in the region below the GEM_i of the cascade (figure 2.5) will correspond to the electric field E_1 in the region above GEM_{i+1} on the cascade.

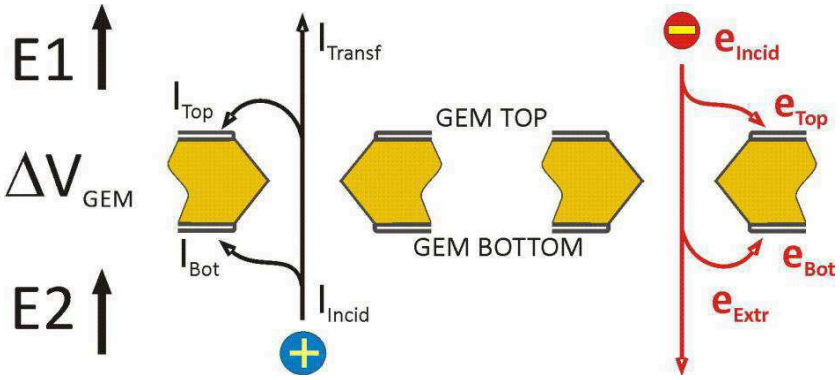

Figure 2.5 - Schematic representation of the ion and electron transfer and capture in a GEM and their dependence on the electric field on both sides of the GEM.

A compromise between the electric fields in the cascade of GEM is usually achieved that maximizes the extraction and focusing efficiencies of the entire cascade. This compromise results in a total charge gain in the detector composed by *n* elements, *G*,

that is not the product of the individual gains of each GEM, *M*, but also includes the transfer efficiency ε from one GEM to the following one [35]:

$$G = (M\varepsilon)^n \tag{2.8}$$

Figure 2.5 gives also a schematic representation of the possible paths that the electrons of the electron cloud and the positive ions can take when crossing through a GEM foil, depending on the value of the electric fields E_1 and E_2 and on the voltage across the GEM, ΔV_{GEM}.

The transference of the ions though a GEM follows a similar relation on the electric fields as the transference of electrons [36]. The probability that an ion coming from the multiplicative stages below the GEM enters its holes is favoured by a low electric field E_2 and increases with increasing $\Delta V_{GEM}/E_2$. On the other side of the GEM, the ions coming out of holes have a probability of being trapped at the top electrode that increases with $\Delta V_{GEM}/E_1$ and for low values of E_1 a large fraction of the ions are collected at the top electrode of the GEM. This effect is responsible for the almost linear decrease in the number of ions that cross through a GEM when the drift field is decreased in gaseous detectors [37].

2.2.6 The micro hole and strip plate

The lithography techniques employed in the production of the GEM and the promising results obtained with this device triggered a series of new developments that led to a considerable growth of the micro-patterned gaseous multipliers family. One of these devices, the Micro-Hole and Strip Plate (MHSP) [38] was developed by the Atomic and Nuclear Instrumentation Group in Portugal (GIAN) in a close collaboration with the Radiation Detection Lab, Israel [39] [40]. This device shares some similarities with the GEM, being also made of a copper clad polymer foil by the same chemical etching process that the GEM, but innovates with the inclusion of an extra multiplicative stage by patterning one of the plain copper electrodes of the GEM into a strip pattern with two independent electrodes.

One of the metallic surfaces of the MHSP (figure 2.6) is modified relatively to the GEM and presents a strip pattern were larger strips (designated by cathodes, with 100 μm width) alternate with thinner ones (that are designated by anodes, with only 30 μm).

These two types of strips correspond to two different electrodes that, in combination with the electrode on the opposite surface of the MHSP, create two different multiplication regions in the MHSP: one inside the holes and another one between the strips (hole and strip multiplication regions in figure 2.7).

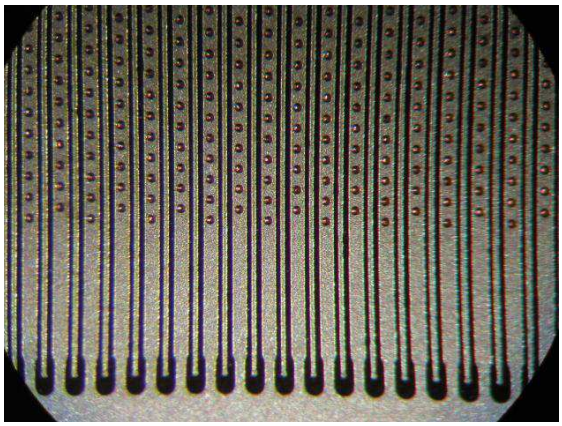

Figure 2.6 - Micro-photography of the patterned surface of the MHSP. The holes crossing the MHSP are centered in the cathode electrodes. These electrodes are 100 mm wide and are separated from the anode electrodes (the thinner strips, with 30 mm wide) by a gap of 35 mm. All the anodes and cathodes are interconnected. The other surface of the MHSP is similar to a GEM (figure 2.4) with the regular honey-comb hole pattern slightly modified in order to create space to accommodate the strips. The MHSP tested on this thesis had all an active area of 28×28 mm^2.

The inclusion of an extra electrode in the MHSP makes this a very versatile micro-patterned device capable of operation in different modes. In the so-called *normal operation mode* (the first one to be tested) the MHSP operates as an electron multiplier with increased gain due to its extra multiplication region. In this mode the plain electrode similar to the electrodes of the GEM (designated by *top*), is placed facing the drift region of the detector. On the opposite surface of the MHSP, the thicker electrode surrounding the exit holes (the *cathode*) is placed at higher potential that the *top*, creating an intense electric field inside the holes. For some values of the voltage between cathode and top ($V_{C\text{-}T} = V_{CATHODE} - V_{TOP}$) the dipolar electric field in the holes reaches values above the multiplication threshold of the gas and, as in GEMs, charge multiplication takes place in this region. But, unlike the GEM, the resulting charge is not transferred to another multiplicative element. Instead it is extracted from the holes

and transferred to the thinner strips, the *anodes*, in the MHSP. This is achieved by placing the anodes at an even higher potential that the cathodes, creating another voltage difference in the MHSP ($V_{A\text{-}C} = V_{ANODE} - V_{CATHODE}$). Once again, for high values of $V_{A\text{-}C}$, the electric field established in the bottom surface of the MHSP (in the region between its cathodes and anodes) reaches high values, above the multiplication threshold and multiplication takes place in this region. Finally the resulting charge is collected at the anodes of the MHSP.

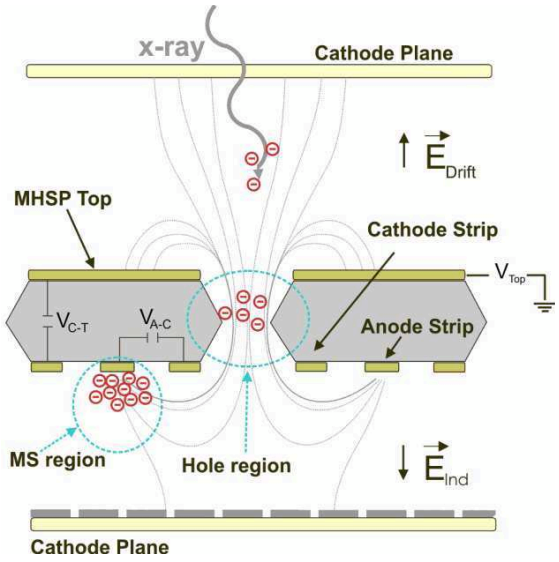

Figure 2.7 - Operation Principle of the MHSP.

The geometry of the MHSP, were the final avalanches are optically hidden from the drift region of the detector, makes of the MHSP a very closed-geometry electron multiplier, with low photon-feedback.

Comparatively to the GEM the ion feedback is also greatly reduced with the MHSP: the ions produced in the vicinity of the anodes are, depending on the electric field intensity in the region below the MHSP (E_{IND}), either collected at the cathode strips or shared between this electrode and the cathode plane below the MHSP. A fraction of the ions back-flowing into the MHSP holes and of the ones produced at the holes is also trapped at the top electrode, strongly reducing the number of ions that reach the drift region of the detector [41].

The MHSP has been developed as a micropatterned detector for X-ray and neutron detection, but its versatility revealed other applications. The presence of the strip pattern on the bottom face of the MHSP gives the MHSP an intrinsic 2D readout making it very suitable as an imaging detector [42]. The scintillation produced in the avalanches that take place in the region between strips is crucial for the PACEM detector [43], one of the techniques developed in this thesis for the ion back flow reduction. The same objective led to the application of the MHSP in a different mode of operation that the one described above, the *reverse mode of operation*, to be detailed in chapter 4 [44]. During all these developments the MHSP has proven to be a stable and reliable detector, operating at high charge gains in several gas mixtures, including high pressure pure noble gases and under high radiation flux with an overall good energy resolution [45][46].

2.2.7 Thick electron multipliers

Thick gaseous electron multipliers (THGEM) have been recently introduced [47] and immediately attracted attentions due to their robustness and easiness of production. These micro pattern structures can be readily produced, in large amounts and at low cost, using standard printed circuit board technology. THGEM are produced by precision mechanical drilling of holes with sub-millimeter dimension in printed circuit boards, covered with copper electrodes on both sides. The initial results have showed that the inclusion of an extra step to the manufacture process of the THGEM, the chemical etching of a small rim around each hole, increases the stability and allows for higher charge gains to be achieved. Currently all THGEM are manufactured with a small rim around each hole, produced by chemical etching methods.

THGEM are produced from printed circuit boards of several thicknesses (t) and the holes are drilled with different diameters (d) in a hexagonal pattern. Standard values for thickness are in the range 0.4 mm to 0.8 mm, although thicker THGEM have been manufactured. The holes are drilled with dimensions going from 0.3 mm to 0.8 mm and maximum gain are achieved for a ratio t/d of approximately 1 [48]. The dimensions of the rim are more standard and THGEM are usually fabricated with a 0.1 mm rim. Figure 2.8 shows the typical aspect of a THGEM, with the holes drilled in the printed circuit board and the rim etched around each hole. As in the standard GEM, the holes in the THGEM are also arranged in a honeycomb pattern.

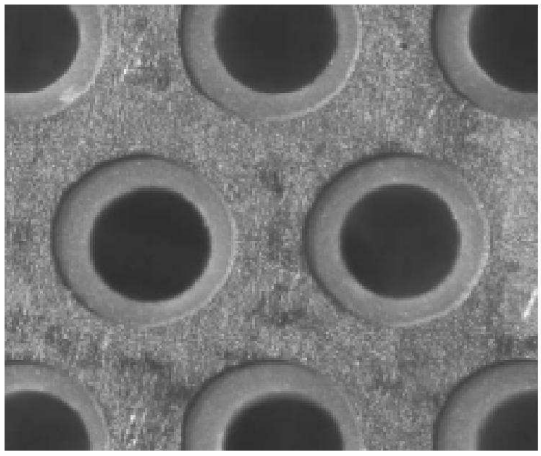

Figure 2.8 - Micro-photography of a THGEM element [48]. The rim with 0.1 mm is clearly seen around each hole.

Due to their internal stiffness, THGEM can be produced in large areas and without the need for additional mechanical support, making them very easy to implement in gaseous detectors. These are usually built with 30×30 mm^2 but larger area, 100×100 mm^2, elements have already been built and tested in argon and neon based mixtures [49].

Despite the larger dimensions of a typical THGEM relatively to a standard GEM, the electric field inside the THGEM holes reaches values above the charge multiplication threshold and gains in the range 10^3-10^4 are obtained with a single THGEM operating in several gases at atmospheric pressure (Ar, Xe and Ar-5% CH_4) [50][51]. The gains obtained with THGEM are dependent on the thickness of the THGEM, increasing with increasing thickness.

As it is the case with traditional hole electron multipliers, two or more THGEM can be cascaded with higher gains and increased stability obtained at the expense of applying higher voltages to the detector. Charge gains as high as 10^6 have been measured using double THGEM detectors in single photoelectron conditions [51].

2.3 Photoelectric effect

The emission of electrons from a metallic surface when placed in vacuum and exposed to radiation was first observed in 1887 by H. Hertz. This phenomenon was further investigated by Lenard, who showed that, although the number of electrons emitted was

proportional to the intensity of the radiation, the energy with which they were emitted was not. It was also noted that for radiation with energy below a certain energy value (the so-called work function of the metal, φ) no emission was recorded, despite the intensity of the radiation [52].

This was then in contradiction with the wave theory of light and was only explained latter in 1905 by Einstein that applied the recently developed quantum theory to this problem. In his explanation Einstein stated that each electron would receive its energy from one photon and would be emitted from the metallic surface with an energy corresponding to

$$E_{PHOTOELECTRON} = h\nu - \varphi \qquad (2.9)$$

Where $h\nu$ represents the energy of each quantum of radiation and φ, the work function of the metal, represents the minimum energy required for the electron emission.

The efficiency with which a solid emits a photoelectron[a] (the *quantum efficiency*, Q.E.) is defined as the average number of photoelectrons extracted for each incident photon that strikes the surface of the solid and varies considerably for different photoelectron emitting materials. This variability is explained by considering the photoelectric effect as a three step process [3][53] involving:

1) Optical absorption of the photon and emission of the photoelectron by the atom or molecule of the material
2) Motion of the photoelectron inside the volume of the material, towards the surface
3) Escape of the photoelectron from the solid, across the potential barrier of the surface

Each of these steps gives a contribution to the quantum efficiency that depends on the properties of the material. Due to high reflectivity of their surface, metals typically tend to be bad photon emitters. Another important effect that hinders the photo-emission in metals is the high amount of free electrons in metals. Once the photo-electron is

[a] From this point on we will refer to the electrons created by photoelectric effect as photoelectrons.

produced in the bulk metal with will suffer a series of interactions until it reaches the surface. The type and the amount of collisions that the photoelectrons endures during the transport in the bulk solid will dictate if it reaches the surface with an energy above the threshold for emission across the potential barrier present at the surface of the solid. In metals, due to the high abundance of free electrons, most of the interactions are electron-electron collisions. In each of these collisions the photoelectron loses a considerable amount of energy and only the photoelectrons produced in a small layer close to the surface (the *escape depth*) will reach the surface with an energy appropriate for the photon emission. In metals the escape depth represents the active area for photoemission and is typically of only of a few atomic layers [54].

The quantum efficiency in semiconductors materials is favoured both by the low surface reflectivity and by the nature of the transport mechanisms in these materials. In semi-conductors a photoelectron is extracted from the valence into the conduction band only if the energy of the incident radiation is above the *energy gap* (*E*g) of the material. In semiconductors, due to the lack of free electrons in the conduction band, most of the interactions in which the photoelectron takes place are scattering mechanisms with the surrounding lattice. Since the average energy loss in each of these interactions is low, the probability that the photoelectron reaches the surface with energy above the potential barrier at the surface (the so called *electron affinity* of the surface, *E*a) is high, even for photoelectrons converted deeper in the material and the escape depth in semiconductors can reach several tenths of nanometres.

2.3.1 CsI photocathodes

Cesium Iodide is one of the most used photocathodes for the detection of radiation in the UV region. This is due to its high Q.E., easiness of production, physical and chemical stability. The sensitivity region of CsI photocathodes covers the UV region of the spectra, reaching a cut-off threshold (at 210 nm) for energies lower that the energy gap of CsI (Eg ≈ 6 eV). The low electron affinity (Ea ≈ 0.1 – 0.2 eV) translates in high Q.E. and large escape depth, typically presented by these photocathodes [55] [56].

Thin CsI films are easily prepared by vacuum deposition in metallic surfaces and are relatively stable in air, sustaining periods of exposition of some minutes without significant decrease in the QE. For larger expositions to air, particularly in high humidity conditions, the CsI reacts with the water molecules and the Q.E. of the film

drops. This process can generally be recovered by an appropriate baking of the substrate [55] [54].The experimental conditions during the production and application of the CsI photocathode play an important role in its properties and have been a major source of discrepancies in the values for Q.E. obtained by independent researchers. Typical values of Q.E. for CsI photocathodes operating in vacuum are around 25 % to 30 % for wavelengths of 170 nm, increasing for shorter wavelengths [55].

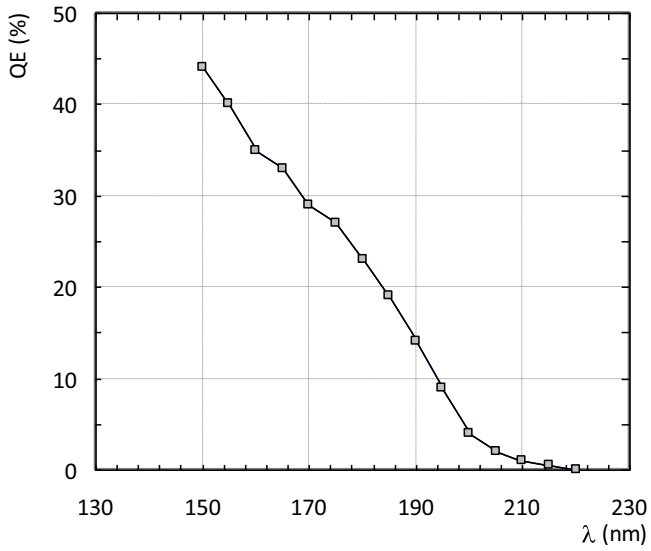

Figure 2.9 - CsI Quantum efficiency, adapted from [57].

Due to their operational properties and high Q.E. CsI photocathodes have found many applications in areas where UV detection is required. They have proven to be both cost and operationally efficient in replacing vacuum photomultipliers in Gaseous Scintillation Proportional Counters [11]. Applications in noble gas cryogenic detectors for dark matter search have been investigated with successful results [58]. The cut-off threshold of CsI photcathodes (at 210 nm) makes them solar blind, with applications going from the fundamental astrophysics to the more practical flame detection [59]. Several RICH detectors equipped with CsI photocathodes have been tested and implemented in large scale facilities for the detection of Cherenkov radiation [60][61].

2.3.2 Photoelectron backscattering

Since the early days of operation with solid photocathodes it was noted that the Q.E. is reduced in gas relative to the vacuum operation [62]. In fact, once the photoelectron leaves the surface of the photocathode, there is a non-negligible probability that it returns to the photocathode, due to collisions with the gas molecules, therefore reducing the measurable Q.E. of the photocathode. This decrease is dependent on the type of gas used and it was observed to be particularly large in monoatomic noble gases, being very small for some molecular gases, particularly CF_4 and CH_4 where the Q.E. in charge collection mode can reach almost the same values as in vacuum [63][64][65].

The drop in Q.E. can be compensated by increasing the extraction field at the surface of the photocathode. For quenched gases, where the scintillation produced is re-absorbed in the gas mixture and no photon feedback occurs, the photoelectron current extracted from a CsI photocathode as a function of the electric field follows the typical behaviour presented in figure 2.10.

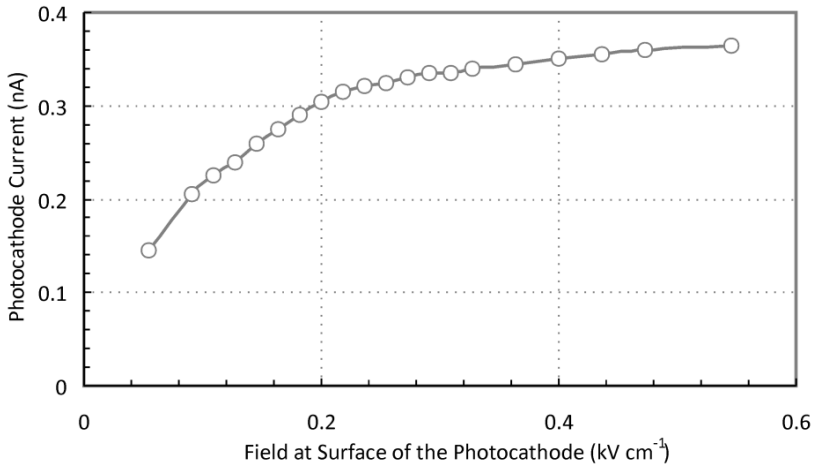

Figure 2.10 – Photoelectron extraction from a semi-transparent CsI photocathode into a gas medium, Ar + 10 % CH_4, as a function of the electric field at the surface of the photocathode.

The behaviour depicted in figure 2.10 is typical of these gases, with the Q.E. reaching a stable plateau prior to the multiplication threshold [62]. When operating photocathodes in gases with the behaviour depicted on igure 2.10 it should be a concern to ensure that the extraction field at the surface of the photocathode, E_{EXTR}, is kept in the plateau

region. This is of particular relevance when extracting primary photoelectron currents and ensures that, even for small fluctuations in the extraction field, the photocurrent extracted from the photocathode is not altered by a significant factor.

2.3.3 Photoelectron extraction in noble gases

In noble gases the photoelectron extraction efficiency is strongly affected by photoelectron backscattering effects and reaches values as low as 0.2 and 0.45 in xenon and argon (for extraction fields of 1 $V \times cm^{-1} \times torr^{-1}$) [66].

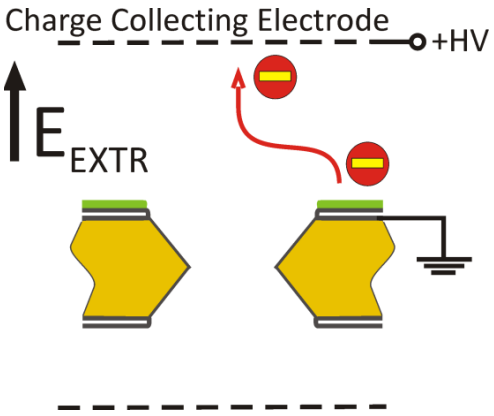

Figure 2.11 - Photoelectron extraction from a reflective photocathode and collection. The electric field E_{EXTR} is responsible for the extraction of the photo-electrons from the reflective photocathode irradiated by an UV beam (not depicted).

In these gases the occurrence of photon feedback mechanisms plays a decisive role in the extraction and collection of photoelectrons. For values of E_{EXTR} above the threshold for scintillation, the photoelectrons extracted from the reflective photocathode will promote (on their path to the charge collecting electrode) the emission of secondary scintillation. This scintillation is emitted isotropically and a fraction of it will reach the photocathode and promote the extraction of new photoelectrons. The setup in figure 2.11 was used in our experiments to measure the photoelectron current extracted from a CsI reflective photocathode deposited on the top electrode of a GEM, as function of the electric field at its surface, E_{EXTR}.

The behavior of the current measured at the charge collecting electrode (figure 2.11) is presented in the chart of figure 2.12, as a function of E_{EXTR}, for xenon. The effect of the

photon-feedback is clearly seen for $E_{EXTR} > 3.0\ V \times cm^{-1} \times torr^{-1}$ when the current increases exponentially with E_{EXTR}. For values of E_{EXTR} in the region between 1 and $2\ V \times cm^{-1} \times torr^{-1}$ the current extracted presents a moderate increase with E_{EXTR}.

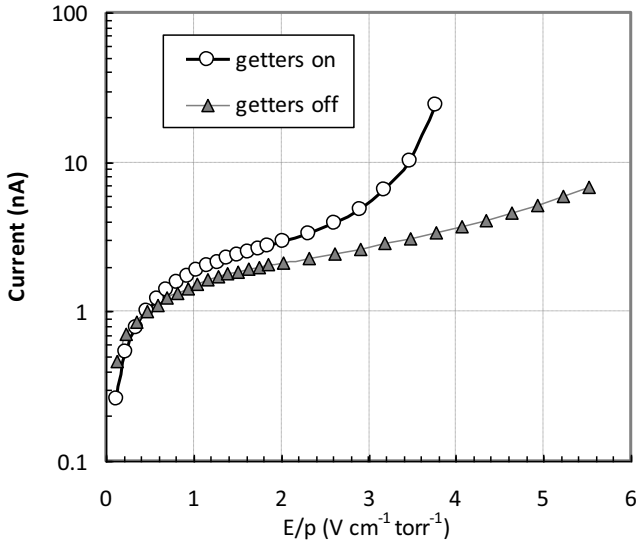

Figure 2.12 - Photo-electron current collected at the charge collecting electrode of figure 2.11, as a function of the E_{EXTR}. Open circles correspond to the normal operation, with the gas purifying getters at a temperature of 200 ºC. The triangles represent the same measurement with the getters off (0 ºC) for several hours. Results were obtained in xenon at 1 bar.

The behavior depicted in figure 2.12 is not in complete agreement with the results obtained by the authors of [66] that measured the photo-electron extraction in xenon and reported an exponential increase for values above $1.5\ V \times cm^{-1} \times torr^{-1}$. This apparent discrepancy could be attributed to differences in the level of impurities presented in the gas. The detector used in [66] had a reduced volume and the excellent purity levels achieved are not comparable to the ones of the detector used in this thesis, with a much larger volume. For an example of the effect of the contaminants in our experimental setup, the chart of figure 2.12 presents also the photo-electron extraction obtained with the getters circuit (to be described in section 3.4) used to purify the gas circulating in the detector closed.

2.3.4 Practical operation of photocathodes

During the work described in this thesis two types of CsI photocathodes, semi-transparent (or transmissive) and reflective (or opaque), were implemented.

Semi-transparent photocathodes are made of thin CsI films deposited in UV transparent windows (in this work we've used semi-transparent photocathodes with ≈ 250 Å thickness deposited in 0.5 cm thick Suprasil® windows). In this type of photocathodes the emission of the photoelectrons is done in the same direction as the direction of the incident UV beam: the UV beam hits one of the surfaces of the photocathode and the photoelectrons are extracted, by means of a suitable electric extraction field, from the opposite surface. The optimum thickness is a compromise between UV absorption in the bulk material and escape depth of the photoelectrons: if the CsI film is to thick and conversion of the UV quanta is done at a distance from the exit surface larger that the escape depth of the photocathode no emission is observed. On the other hand, the photocathode has to be thick enough to ensure that the UV radiation is absorbed in the bulk material and the photoelectrons are produced in the first place.

In reflective photocathodes the exit and entry surface are the same and the photoelectrons leave the material from the same surface were the UV radiation penetrates. Photocathodes operating in this mode are usually made of thicker films that the semi-transparent ones (≈ 2500-3000 Å) in order to increase the UV absorption. Reflective photocathodes are deposited in opaque surfaces, usually metallic and with some reflectivity to the VUV: a photon that is not absorbed when crossing the medium has a probability of being reflected and returning back to the medium for absorption giving an increase in the Q.E. of this kind of photocathodes.

2.4 Gaseous detectors and solid photocathodes

Solid photocathodes, either reflective or transmissive, can be coupled to gaseous detectors composed of several cascaded gas electron multipliers and directly placed in the detection volume without the need to use separation windows.

In the semi-transparent operation mode the CsI photocathode is deposited on a transparent window and placed at some distance of the first element of the gaseous multiplier cascade [67] [68]. The electric field in the drift region, E_{DRIFT}, promotes the extraction of photoelectrons from the CsI photocathode and plays a major role in their

focusing into the holes of the gas electron multiplier. As we've seen in 2.3, a high ratio of hole voltage to drift field is a requirement for efficient focusing of the photoelectron into the holes of the GEM. In the operation of semi-transparent photocathodes coupled to GEM a compromise is usually required since the drift field is (in this particular configuration) also responsible for the extraction of photo electrons from the CsI photocathode and must be kept at a sufficiently high value to assure a good extraction efficiency [69].

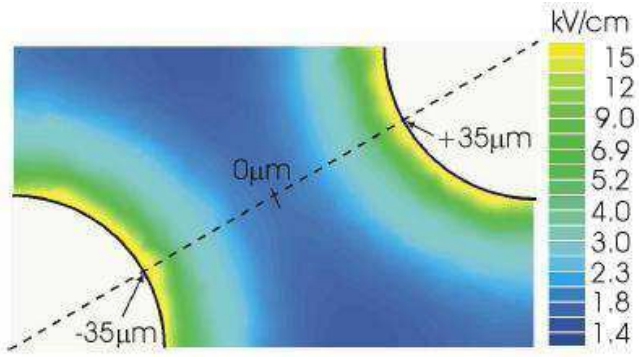

Figure 2.13 - Electric field intensity at the surface of a GEM [70], for $\Delta V_{GEM} = 300$ V. The electric field is higher at the periphery of the holes and drops towards the 0 point were it reaches values above 1 $kV \times cm^{-1}$.

The operation of GPD operating in the reflective mode is easier to implement and less subject to the constrains of semi-transparent GPD. The CsI photocathode is directly deposited on the surface of the first element of the cascade making it sensitive to radiation. In this mode the efficient extraction of the photoelectrons from the CsI surface is achieved with a combination of high electric field inside the holes of the electron multiplier and low (preferably zero) electric field in the region above the GEM, E_{DRIFT}.

In these photocathodes the extraction of photoelectrons from a reflective photocathode deposited on the top surface of a GEM and their focusing in the GEM holes is promoted by the dipolar electric field established in the holes of the GEM. This field, created by ΔV_{GEM}, extends itself to the top surface of the GEM, were it reaches values suitable for the photo-electron extraction (figure 2.13).

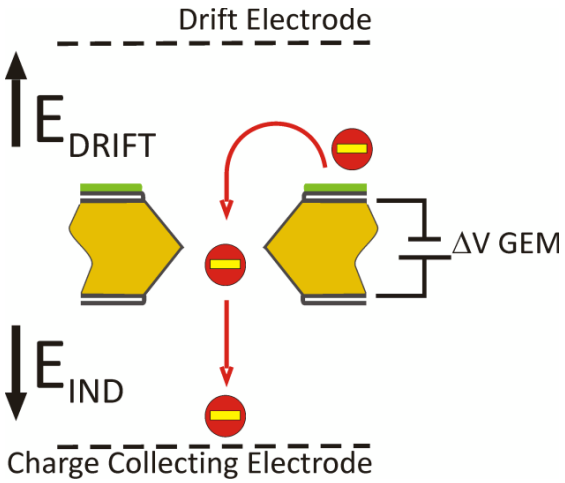

Figure 2.14 - The voltage difference between the top and bottom surface of the GEM creates a dipolar electric field that extends to the top surface and promotes the extraction of photo-electrons from the a reflective photocathode. The establishment of an electric field, E_{DRIFT}, in the region above the photocathode will affect the extraction and focusing of the photo-electrons.

For a fixed voltage across the GEM holes, ΔV_{GEM}, the extraction of the photoelectrons from the reflective photocathode and their focusing into the holes of the GEM are strongly influenced by the electric field in the region above the photocathode (E_{DRIFT} in figure 2.14). A positive value of E_{DRIFT} (relative to the orientation of figure 2.14) is not favourable to the extraction of photo-electrons from the reflective photocathode and will reduce the extraction efficiency, leading to a drop in the final charge collected at the charge collecting electrode. This effect is expressed on the chart of figure 2.15, were for positive values of E_{DRIFT} the photoelectron extraction efficiency in xenon drops with increasing E_{DRIFT}. This effect is dependent on the ΔV_{GEM} and can be compensated by increasing its value: for $\Delta V_{GEM} = 400$ V the effect of the drift field is compensated and the extraction efficiency approaches the one measured for null drift field.

On the other hand a negative value of E_{DRIFT} is favourable to the photoelectron extraction from the photocathode but not to the photoelectron focusing into the holes of the GEM. The increase in E_{DRIFT} promotes the collection of the photoelectrons at the drift electrode of figure 2.14, competing with the effect of the dipolar electric field established inside the holes and thus the photoelectron current reaching the charge collecting grid decreases when E_{DRIFT} is increased to more negative values.

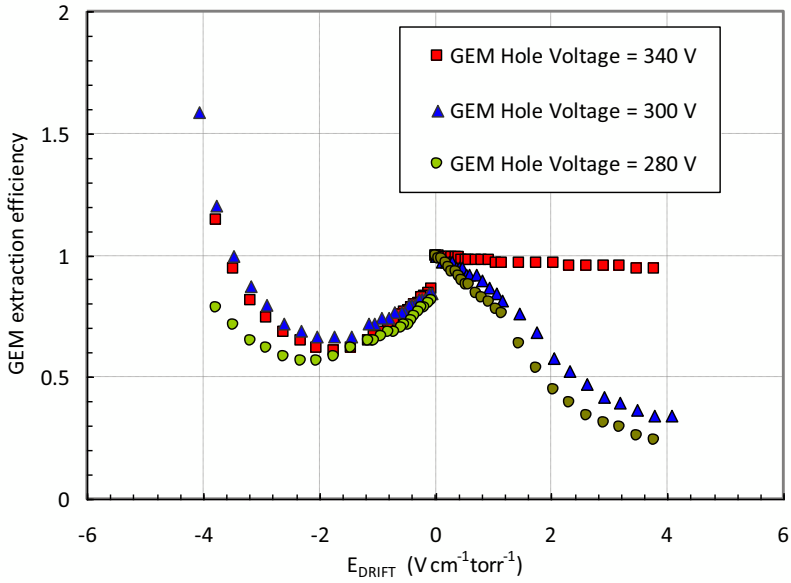

Figure 2.15 - Photoelectron extraction efficiency. The results were obtained with the setup presented in figure 2.14. An Ar(Hg) lamp was used as a source of UV photons. For constant ΔV_{GEM} and E_{IND} the current collected at the charge collecting mesh reflects the change in the photoelectron extraction efficiency. Results obtained in xenon at 1 bar.

Until now the behaviour of the photoelectron extraction efficiency in xenon is similar to the one in quenched mixtures (figure 2.16) where the inclusion of a small amount of a quenching gas absorbs the photons emitted by the noble gas and prevents the photon-feedback mechanisms to occur. In noble gases the photon-feedback is not suppressed and above the threshold for scintillation in xenon ($> 1\ V \times cm^{-1} \times torr^{-1}$) the electrons start to produce the electroluminescence, characteristic of noble gases.

The increase in the photo-electron extraction efficiency measured in xenon for values of E_{DRIFT} lower that $-2\ V \times cm^{-1} \times torr^{-1}$ (figure 2.15) is the result of the photon feedback caused by the scintillation emitted by the photo-electrons extracted from the reflective photocathode and that are collected at the drift electrode.

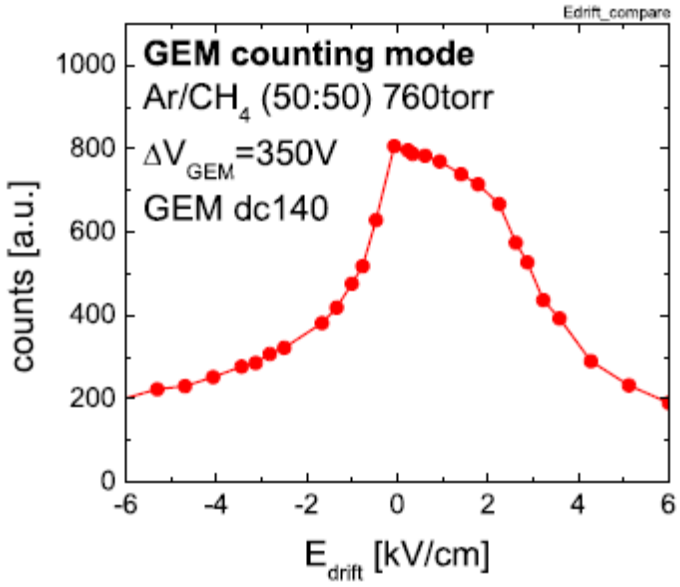

Figure 2.16 - Influence of the drift field on the photo-electron extraction efficiency in Ar/CH_4 [71].

2.5 Effects of ions in gaseous detectors

The performance of gaseous detectors is often limited by secondary effects induced by photon and ions produced during the avalanches in the detector. While the presence of photons can be suppressed with the use of an appropriate quenching gas, the production of ions is an unavoidable consequence of the charge multiplication mechanisms in gaseous detectors.

The positive ions drift in opposite direction of the electron cloud with a velocity that is typically a few orders of magnitude lower and accumulate in the detector, causing local distortions on the electric field that affect both the gain and tracking performance of the detector. Already in the early days of wire chambers it was recognized that the build up of the positive ions produced during the avalanches in these detectors when operating at high rates (this effect was already visible at rates of 10^4 $Hz \times sec^{-1}$) could distort the electric field to the point of annulling the gain of the detector [72]. In the development of TPC, that operate at low, uniform drift field, the build up of positive charge in the sensitive region of the detector was also soon recognized to be a problem [28] and a standard element of any TPC now developed is a ion blocking gate. This gate is an ingenious device that once triggered (after the electrons have passed through it and the

electron signal is being developed in the cascade) reverses the polarity on its wires and closes the passage of the positive ions, preventing them to reach the drift/conversion region of the detector. This technique is very efficient in suppressing the positive ions but has some important drawbacks. It requires an electronic trigger that is not always available in all experiments [73] and, since it is an electrode inside the detector for which the applied voltage changes rapidly, introduces further electronic noise. In addition, since the ion drift velocity is small, the dead-time of such electron multiplier is very large and, therefore, only useful for low count rates. The currently planed experiments in high energy physics will operate at particle fluxes well above the 10^5 Hz counting rate limit obtained with gating electrodes [70] and will required DC methods of ion blocking [74].

In their backflow movement, the positive ions are eventually collected at the cathode electrodes of the detector were they can induce the emission of secondary electrons. This is particularly true for sensitive photocathodes, as the ones used for visible light detection with a low ionization potential. The probability of secondary emission from these photocathodes is extremely high and their operation is hindered by the ion feedback levels present in current gaseous detectors. The impact of the positive ions in the visible sensitive photocathodes causes also its chemical aging, preventing the long term operation of gaseous detectors equipped with this type of photocathodes. These effects have represented until now a serious limitation to the implementation of GPM equipped with visible sensitive photocathodes and motivated a long series of R&D efforts [75] in order to reduce the ion back flow in gaseous detectors.

2.5.1 Ion back flow

The fraction of the ions produced in the detector and that reaches a particular area of interest in the detector is designated by *ion back-flow fraction*, IBF. This quantity is equivalent to the ratio between the number of ions measured and the total number of electrons collected at the anode of the detector:

$$\mathrm{IBF} = \frac{\mathrm{Ions}}{\mathrm{Primary\ electrons} \times \mathrm{Gain}} \tag{2.10}$$

In an open geometry detector, as it is the case with the MWPC or parallel plate chambers, all the ions produced will eventually reach the cathode and in these detectors the IBF reaches values close to 1 [75] .

In cascaded gas electron multipliers the IBF is naturally reduced due to the trapping of ions at the several electrodes of the detector elements. The electric field configuration plays a decisive role in the value of IBF in these detectors as well as the gas mixture and the shape of the electrodes [73]. Another significant parameter for the IBF in cascaded gas electron multipliers is the intensity of the electric field in the drift region. The IBF is particularly dependent on the drift field, increasing almost linearly with E_{DRIFT}. In detectors complying with the low drift field (0.1 $kV \times cm^{-1}$) requirements of TPC the best IBF values reached were ≈ 1 %, obtained at a gain of 10^4, and slightly higher, ≈ 3-5 %, at higher gains. GPM typically operate at higher drift fields (> 0.5 $kV \times cm^{-1}$) and in these conditions the best IBF values, 5%, were obtained at a total gain of 10^4 [76].

The IBF in cascaded gas electron multipliers can be further improved by incorporating an MHSP as the last element of the cascade. Due to the electric field configuration in the anode-cathode plane of the MHSP (see figure 2.7) a significant fraction of the ions produced in the last multiplicative stage on the MHSP is trapped in the cathodes and on the electrode placed below the MHSP. The incorporation of an MHSP as the last element of a cascade of 3-GEM coupled to a reflective photocathode allowed to achieve IBF values of 0.03 at total gains of 10^5 [41]. This value represents a strong reduction from the 0.1 value of IBF obtained, at similar gains, with a 4-GEM detector coupled to a reflective photocathode and demonstrates the potential for IBF reduction with the MHSP.

Despite the efforts in the reduction of the IBF summarized above, the current IBF values were, at the time we've started our research, still not satisfying and posed a limitation to the efficient operation of the long time awaited detectors such as the GPM equipped with visible photocathodes or of high rate TPC in development for the future generations of colliders.

The development of GPM sensitive to the visible spectral range is based on the operation of photocathodes with low electron-emission threshold. In these photocathodes the probability of emission of ion induced secondary electrons (IISEE) is relatively high, causing limitations to their efficient operation [77]. In this type of

detectors the IBF has to be suppressed to values of 2×10^{-4} at a total gain of 10^5 for a stable operation and sensitivity to single-photon [78].

The requirements for the operation of TPC are less obvious as the adequate IBF values on these detectors are dependent on the primary charge distribution, on the detector geometry and on the acceptable amount of track distortions [73]. As a rule of thumb it is considered that these detectors require that the fraction of ions reaching the sensitive regions of the detector to be suppressed to values of G^{-1}, being G the total gain [73] [79].

3 EXPERIMENTAL METHODS

3.1 Introduction

The experimental work described in these chapters was done in two different laboratories devoted, amongst other research interests, to the development of gaseous detectors: the Radiation Detection Lab in Israel (chapter 4) and the "Grupo de Instrumentação Atómica e Nuclear" (GIAN) in Portugal (chapter 5 and 6). These two labs have a long tradition in the field of radiation detection and have developed a series of techniques and methods that were employed in this work.

The detectors developed in this work are cascaded gaseous multipliers, composed by several elements (GEM and MHSP, photocathodes and metallic meshes) mounted in individual frames and stacked inside a test chamber. The type, number of elements and the distance between them can be easily changed, allowing the implementation and testing of several detector configurations without any mechanical modifications to the test chamber used.

3.2 Test chamber

The test chamber developed in the GIAN laboratory is made of a stainless steel metallic cylinder with 160 mm of diameter and 35 mm height. This chamber is vacuum sealed in both ends by 2 metallic flanges using Viton® O-rings. The electrical connections used

to polarize the detector electrodes were placed in a circle in the periphery of one these flanges and are electrically isolated using custom made MACOR feedthrough. These feedthrough were glued to the detector using non conductive, low outgassing epoxy glue, ref. TRA-BOND 2116 [80].

One of the flanges was equipped with 4 plastic pillars, placed in the vertices of a square, 42 mm apart and centred with the flange. The several elements of the detector were stacked in these pillars.

The entrance window of the detector was located in the opposite flange of the detector that was designed to accommodate two different types of windows: a 25 μm thick aluminized Mylar window for the operation of the detector with X-ray sources and a 5 mm thick fused silica (UV transparent) window for the operation of the detector with UV photons. These two windows were interchanged whenever it was required to change the operation mode of the detector.

During the measurements presented in this work the detector was always operated in sealed mode[a] and, in order to ensure high gas purity, the gas was continuously purified circulating by convection through non-evaporable getters (ref. SAES St707) placed in a circulating system attached to the detector main body and kept at an adequate temperature for the purification of the gas (usually 200 ºC for noble gases and 150º for CF_4).

3.2.1 MHSP and GEM assembly

The several MHSP and GEM micro-pattern structures used during this work were made of thin, flexible Kapton® foils without any internal stiffness. In order to properly delimitate the distances between the several elements of the detectors all the micro-pattern structures were attached to solid frames made either of G10 or MACOR. These frames had the advantage that, once the micro-pattern were attached to them, could be used as building blocks in the detector and easily exchanged or replaced.

[a] The detector is filled with the gas and sealed, operating without renovation of the gas. Gaseous detectors can also be operated in flush mode, with a constant renewal of the gas inside the detector.

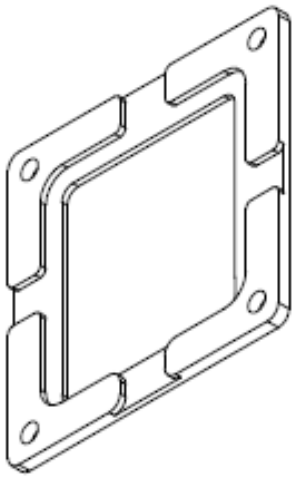

Figure 3.1 - Production drawing of the 2 mm thickness MACOR frame used for the MHSP. The MHSP were glued in the internal rim while the wires for the electrical connections were glued in the outer depressions. The frames used had an area of 50×50 mm^2 and the holes were placed in a square pattern, 42 mm apart.

The choice for a MACOR or G10 frame as holder for the micro-structures was done according to the application desired for the detector. G10 is an extremely porous material with high out-gassing. The use of G10 frames as holders for micro-structures was restricted to the work done in chapter 4, with detectors operating in flow mode. The operation of sealed detectors with constant purification that rely in scintillation mechanisms to amplify the primary charge (as the ones described in chapter 5 and 6) requires special care in the choice of materials and in these detectors the frames used were made of MACOR, a machinable ceramic with good vacuum properties.

Despite the differences in the material constituting the frame, the setup-up process shared many similarities. The MHSP or GEM element was cut out of the larger Kapton® foil were it was produced with a total area of 30×30 mm^2, leaving a small Kapton border around the 28×28 mm^2 micro-patterned active area. After cutting, the MHSP/GEM was tested for potential short-circuits between the electrodes with a voltmeter. Once this first quality test was passed the MHSP/GEM was glued to the frame. The G10 holders (1.6 mm thick) were produced with copper-pads (to were the connecting wires were previously soldered) and the electrical contact between them and the micro-structure electrodes was easily established with a conductive silver paint. A

layer of high voltage rated scotch tape was placed on top of the silver paint for additional stability and electrical insulation.

The MACOR frames used (with 1.0 and 2.0 mm thickness) were produced without the copper electrodes and the assembly of the GEM/MHSP in these frames required longer time and more care that on the G10 frames. Before the GEM/MHSP assembly a small layer of conductive epoxy glue, Tra-Duct 2916, was placed on the MACOR frame to establish the electrical contacts and, simultaneously, holding the electrical wires used for the polarization of the micro-patterned structures to the frame. After the completion of this first process (the epoxy-glue used has a typical curing period of 24 hours) the non active area of the GEM/MHSP was glued to the frame with the non-conductive epoxy-glue. The assembly process in the MACOR frames was completed with another gluing of the electrodes of the GEM/MHSP to the previously deposited contacts using the conductive epoxy glue.

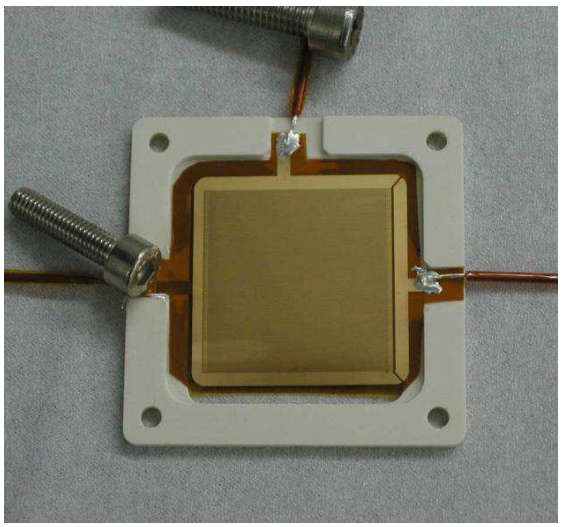

Figure 3.2 - Photography of an MHSP glued to a MACOR frame and ready to be placed in the detector.

During the assembly of the GEM/MHSP in their frames great care was taken to ensure that the micro-structure was perfectly stretched in the frame. After this process, the frame holding the micro-structures was easily stacked in any combination required, using for that the holes depicted in figure 3.2 and the 4 threaded plastic pillars attached to the base of the detector. Thin MACOR spacers with different thickness (from 0.5 to

several millimetres) were used to establish the separation regions between elements of the detector. Finally the stacked elements that composed the detector were kept in place using metallic nuts screwed around the tip of the threaded plastic pillars.

After the final assembly of the detector, and prior to the vacuum and gas filling, all the elements were voltage tested and in case any defect was found the element was easily replaced. All the procedures described above were done in a clean-room controlled environment.

3.2.2 Other detector elements

Besides the GEM and MHSP elements the detector was composed by other parts that were also mounted in frames with the detector dimensions. The metallic meshes used in the detector were made of 80 μm diameter stainless steel wires with 900 μm spacing. These meshes were stretched in 1 mm MACOR frames and glue to them with the non-conductive epoxy glue. The conductive wire used for the polarization of the mesh was glued with the conductive epoxy.

The current mode measurements require the production of a continuous flow of primary electrons in the detector. This current was extracted from a semi-transparent photocathode deposited on the surface of an UV transparent window with 5 mm thick and 5 cm of diameter. Previously to the CsI deposition the window was evaporated with a small layer of aluminium that ensures proper electrical contact and electric field uniformity throughout the photocathode surface. The UV transparent window is attached to a stainless steel frame with dimensions similar to the ones used for the GEM/MHSP.

3.3 Evaporation plant for the CsI photocathode production

The production of CsI photocathodes (either reflective or semi-transparent) by vacuum deposition is a relatively simple process but requires a dedicated system. This process was done several times during this work, either at the radiation detection lab in Israel and at GIAN laboratory in Portugal and follows similar procedures for both sites. Therefore only the GIAN system, were most of the vacuum depositions were done, will be described here.

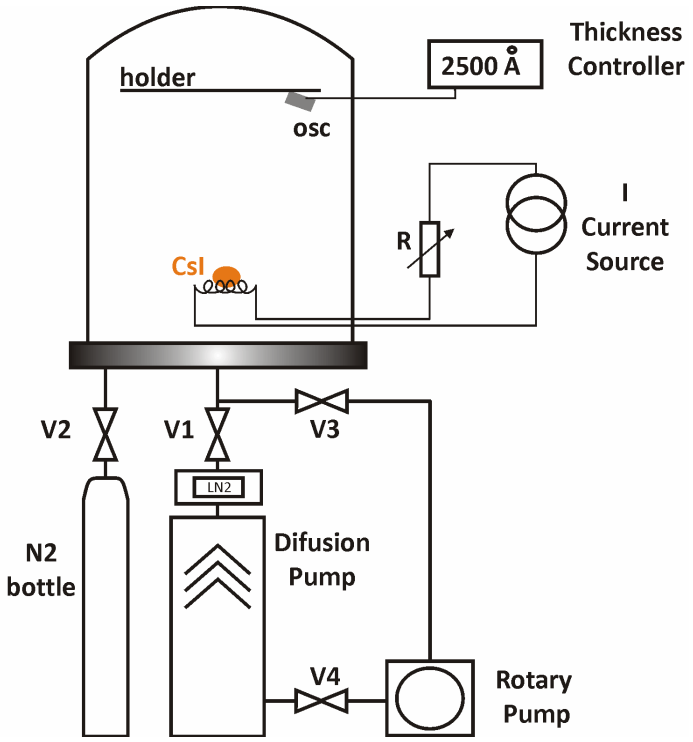

Figure 3.3 - Schematic representation of the evaporation plant used for the preparation of the CsI photocathodes.

The vacuum deposition system depicted in figure 3.3 comprises a diffusion pump, equipped with a liquid nitrogen cold trap, connected to the deposition chamber by a main vacuum valve, V1. A rotary pump is used to produce the rough vacuum in the evaporation chamber (through valve V3) and to assure the backing vacuum of the diffusion pump (through valve V4). With this setup the vacuum inside the deposition chamber can reach values as low as 1.0×10^{-7} mbar after a few hours of operation. Valve V2 allows the introduction of gas (either atmospheric air or nitrogen) for the opening of the chamber once the deposition is completed.

The CsI, in the shape of small crystals, is placed in a resistive tungsten holder and heated by passage of a current, I. The thickness of the CsI film to be deposited can be previously determined by the measuring the amount of CsI placed in the holder or, as it is was the case in this work, controlled by a thickness deposition monitor connected to a oscillator crystal (*osc*) placed in the vicinity of the substrate where the CsI is to be deposited.

The control of the start and the stopping of the deposition process is done with a shutter (not depicted) placed in front of the CsI holder and mechanically actuated from the outside of the deposition chamber.

Vacuum deposition is controlled by the current passing through the CsI holder and by the consequent eating of both the holder and the CsI (the boiling point of CsI is approximately 500 ºC [81]). Prior to the deposition, the vacuum levels in the chamber are kept in the order of 10^{-6} mbar for several hours to assure a minimum of impurities during the deposition process. This process takes a few minutes, and should be done at a deposition rate in the range 10-20 angstrom/sec [55].

CsI is an extremely hygroscopic material and loses its quantum efficiency when exposed to humidity conditions. The room were the vacuum deposition system is located is equipped with a de-humidifier system and the process of removing the photocathodes from the deposition chamber and placing them under vacuum inside the detector was optimized to take no more that 5-10 minutes.

3.4 Detector and gas system description

The system used to create the vacuum and filling of the detector is depicted in figure 3.4. The gases are supplied from individual containers through valves V2 and V3. The gases used in the measurements were all high purity grade, with minimum purity of 99.99%, directly transferred from the original bottle to the admission line at vacuum levels of 10^{-6} mbar (these levels were measured with P1 and were achieve after a few hours of pumping in the system).

The pressure during the filling of the detector, after sealing and during the operation is controlled by the manometer P2. The detector was always operated in closed mode, with the gas being constantly purified by convection through the non-evaporable getters that are kept at their operational temperature using a heating tape with regulated temperature control. The purification circuit could be easily isolated from the detector (for maintenance purposes) using valves v7 and v6. The main valve, v4, controlled the connection of the detector to the main vacuum system. This system is equipped with a turbomolecular pump and can reach vacuum levels of 10^{-6} mbar.

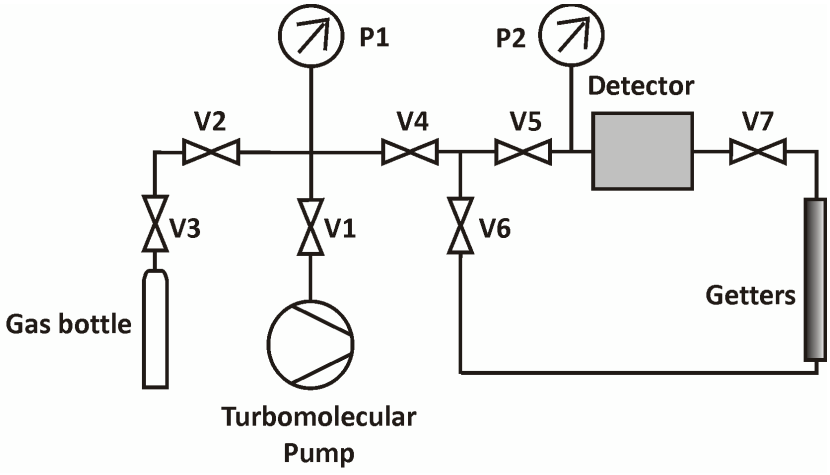

Figure 3.4 - Experimental system used to evacuate and fill the detector. The detector main valve, V4, isolates the detector and gas circulating system from the vacuum system. The detector can be isolated with valves V5 and V7, allowing the getters to be activated without contamination of the detector. P2 and P1 are pressure gauges. The turbomolecular pump is assisted by a rotary backing pump, not depicted.

Prior to the gas admission, the system was evacuated down to 4×10^{-6} mbar with valves v1, v2 and v4 to v7 open. Once the vacuum level above mentioned was reached, the turbo-molecular pump was isolated from the system by closing the main valve v1 and the gas was slowly admitted to the detector through valve v3 until the required pressure was achieved in the system.

3.5 Pulse mode measurements

In the pulse-counting mode operation the primary charge was deposited in the drift region of the detector by conversion of X-rays from radioactive sources, usually Cd^{109} (22.1 keV) or Fe^{55} (5.9 keV). The drift region of the detector is limited by the detector window and by the first element of the cascade of electrons multipliers that constitutes the detector to be tested. In this operation mode the entrance window of the detector is made of an aluminized Mylar foil (25 μm thick) glued with a low out-gassing conductive epoxy to a stainless steel frame that is screwed to the detector body using a Viton O-ring for the vacuum sealing.

Due to the electrical connection between the detector window and the body of the detector in this mode of operation the detector window must always be connected to

ground potential and, in order to transfer and amplify the primary charge, the detector has to be polarized with growing positive voltages between consecutive electrodes. The primary charge produced by each event is multiplied at the several stages of the detector until the final charge is collected at the anodes of the detector, using charge sensitive preamplifiers.

An individual power supply is used for the polarization of each electrode of the detector. Two different models were used during the measurements: the more sensitive electrodes of the MHSP, GEM and T-MHSP were polarized using CAEN N471 A power supplies. These power supplies have the feature of limiting the current supplied to values as low as 1 nA. This was extensively used during the present work and the output currents were limited to the 60-80 nA range, in order to protect the sensitive micro-patterned electrodes in case of discharges in the detector.

The final charge collected at the anode of the detector was feed to a charge sensitive preamplifier, Canberra 2006 (with two selectable values of sensitivity, 47 mV/MeV and 235 mV/MeV) and was feed to a linear amplifier, model Tennelec TC 243. The output of the amplifier was connected to a Nucleus PCA2 1024 multichannel analyzer and the electronic chain sensitivity was calibrated by injection of a known charge into the preamplifier input.

3.6 Current mode measurements

The operation of gaseous detectors in the current or DC mode is extremely convenient for the direct evaluation of the currents on the different electrodes of the detector. With the knowledge of the values of the currents in the several electrodes of the detector it is straightforward to calculate the charge gain and ion back flow fraction of the detector. The measurements in current mode are done with the production a continuous flow of primary electrons, usually extracted from a semi-transparent photocathode, conveniently placed inside the detector and in direct contact with the detection medium. This primary electron current is then multiplied in the detector and produces an output current at the anode of the detector.

The production of the primary electron current in the detection medium is done with an external UV beam that enters the detector and reaches the semi-transparent photocathode placed inside the detector that limits the drift region of the detector.

To operate in current mode the test chamber has to be slightly modified relatively to the pulse mode configuration and the Mylar window used in the pulse-counting mode (that is opaque to the UV radiation) is replaced by a 5 mm thickness suprasil window, transparent to the UV emitted from the lamp (a Hg(Ar) calibration lamp, model Oriel 6035, was used in our measurements).

The photocathode used for the production of the primary electron current is of the semi-transparent type, consisting on a 250 Å CsI film deposited in a 5 mm thickness suprasil plate (this plate is similar to the one used as entrance window for the test chamber). This circular plate, with 50 mm diameter was glued with the conductive epoxy to a metallic frame and was pre-evaporated with a thin, 150 Å, layer of aluminium, to ensure a proper electrical contact and field uniformity through the photocathode surface. This aluminium layer is sufficiently thin to allow the transparency of the UV beam but provides adequate electrical contact in order to obtain a uniform electric field at the surface of the photocathode. This photocathode was placed at a fixed distance from the first element of the cascade of multipliers, defining the drift region of the detector. The polarization of the photocathode (as all the electrodes of the detector) was established through high voltage rated connections, connected to the detector high voltage feed-through. The electric field in the drift region of the detector was established with the appropriate polarization of the photocathode (usually placed at ground potential) and the first element of the cascade of gaseous multipliers. This electric field was responsible for the extraction of the primary electron current, I_{PC0}, from the semi-transparent photocathode. Besides being strongly dependent on the value of the electric field at the surface of the photocathode, I_{PC0} is also strongly dependent on the UV photon flux that reaches the photocathode. This flux was regulated and stabilized by the power supply used to power up the UV lamp.

The I_{PC0} primary current was always recorded prior to each measurement and without charge multiplication in the detector in order to discard any ion back flow contributions. The UV flux was adjusted in order to obtain a value of I_{PC0} of a few nA at the beginning of the measurements. During the measurements the currents in the detector electrodes were always kept below 100 nA and if required the UV photon flux was reduced by placing absorbers in the UV beam path, outside the test chamber.

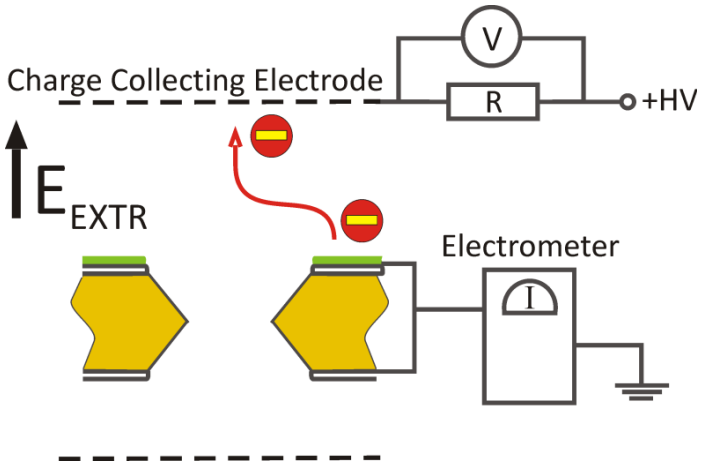

Figure 3.5 - Representation of the setup used to confirm the accuracy of the current measurement done by measuring the voltage drop at the resistor R. The photoelectron current emitted from the CsI photocathode is extracted to the gas and collected at the charge collecting grid. The measurements of the current at the electrometer and at the voltmeter are coincident. The photocathode, of the reflective type, was deposited on the top electrode of a GEM.

The currents recorded in the electrodes placed at ground potential were measured with high precision electrometers, model Keithley 610 C, placed between the electrodes and the ground reference. The same method could not be used to measure the currents in the electrodes connected to high voltage (such as the anode of the detector) and the value of the current in these electrodes was obtained from the measurement of the voltage drop across a resistor connected in series with a power supply. The agreement between these two measurements was compared with the setup depicted in figure 3.5: the photoelectron current emitted from a reflective photocathode (placed at ground potential) is measured by the calibrated electrometer. The photoelectron current emitted by the reflective photocathode is collected at the charge collecting electrode (a metallic mesh) and its value is calculated by measuring the voltage drop across the resistor R. If no charge is lost or produced (by parallel plate avalanche) during the transport in the gas medium the currents measured by both methods are similar (figure 3.6).

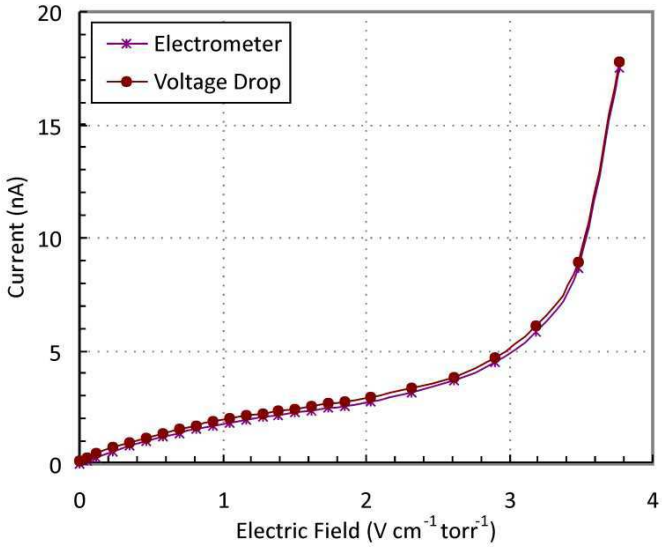

Figure 3.6 - Comparison of the methods used to measure the currents on the setup of figure 3.5, in xenon. The increase in the currents measured is caused by a increase in the extraction-efficiency for low values of electric field (up to 2-3 $V \times cm^{-1} \times torr^{-1}$) and by photon-feedback mechanisms for electric fields above these values.

4 ION BLOCKING WITH THE R-MHSP

4.1 R-MHSP concept

The micro-strip pattern present in the bottom face of the MHSP was developed with the purpose of providing the MHSP with an additional multiplication stage but it was soon suggested [82] that the presence of the anode strips in the bottom surface of the MHSP could be used for a very promising application: trapping of the positive ions back-flowing in the detector.

The application of the standard MHSP to the ion back-flow reduction in gaseous detectors is achieved by placing the thin strips (that in the normal operation mode previously described are designated by *anodes*) at a lower potential that the wider strips (the *cathodes* in the normal mode). In the reverse mode of operation (R-MHSP) the thin strips are at a lower potential that the wider ones but for simplicity we will keep the same notation as before and continue to use the word anodes to describe the thin strips of the MHSP (despite the fact that in the R-MHSP no electrons are collected in these strips). The voltage between these two electrodes, $V_{A\text{-}C}$ (corresponding to V_{ANODES}-$V_{CATHODES}$) now takes negative values since $V_C > V_A$.

The polarization of the thin strips with negative voltages intends to trap the positive ions while these are flowing from the lower stages of the detector (were most of the negative charge is produced) by taking advantage of the difference in the drift and diffusion movement between electrons and ions. The great difference in the mobility of ions and

electrons translates in longer transit time of positive ions through the detector with the positive ions being under the influence of the electric field for a longer period of time than the electrons. Despite the equivalent but opposite charge, electrons and ions have slightly different paths in the detector and the R-MHSP tries to take advantage of this difference and de-couple the paths of electrons and ions.

When the MHSP is operated in reverse mode (R-MHSP) it is incorporated in a cascade of electron multipliers as the first element of the cascade, with the top electrode facing the drift region and the strip pattern facing the remaining stages of the detector. In this setup, depicted in figure 4.1, the primary electrons produced in the drift region of the detector are focused and multiplied in the holes of the R-MHSP as in the normal mode of operation of the MHSP (see section 2.2.6).

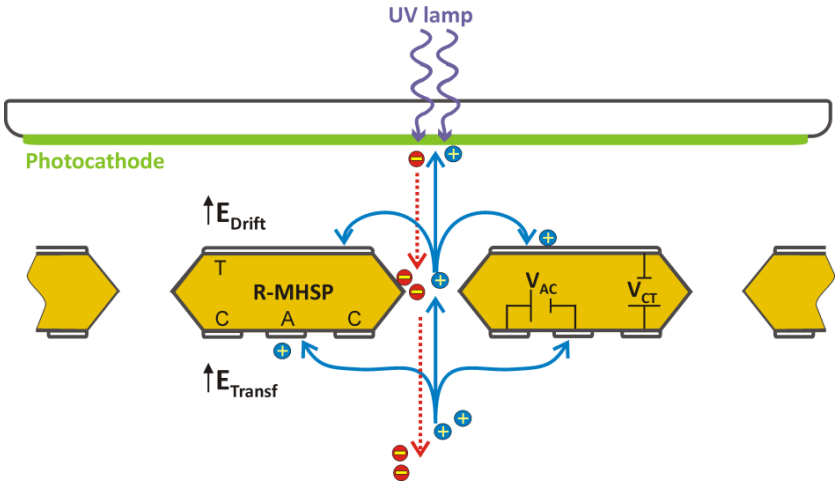

Figure 4.1 - MHSP operating in reversed mode (R-MHSP) coupled to a semi-transparent photocathode and operating in current mode.

The multiplication stage in the holes is controlled by the voltage across them, $V_{C\text{-}T}$, as in the normal operation mode of the MHSP. After the first multiplication stage the resulting electron cloud is extracted from the holes by action of the transfer field, E_{TRANSF}, and is further multiplied in the following elements of the detector (not depicted in figure 4.1). In this operational mode the final charge is no longer collected in the R-MHSP and therefore this micro-structure can be placed anywhere in a cascade, not being limited to the last element of the cascade, as it is the situation when the MHSP is

operating in normal mode [41]. Preferably, in order to trap as much ions as possible, the R-MHSP is placed as the first element of the cascade.

A fraction of the positive ions produced in the multiplicative stages of the cascade of electron multipliers flows back through each element of the detector and eventually reaches the R-MHSP. The role of the thin strips, now at a lower potential that the wider ones, is to attract these positive ions, trapping and preventing them of reaching the holes of the R-MHSP and from there the drift region of the detector.

The movement of the positive ions in the electric field configuration of the R-MHSP was first simulated using the GARFIELD software package [44], figure 4.2, and seems to validate the R-MHSP principle, indicating that a large fraction of the ions back-flowing will be trapped at the anodes of the R-MHSP.

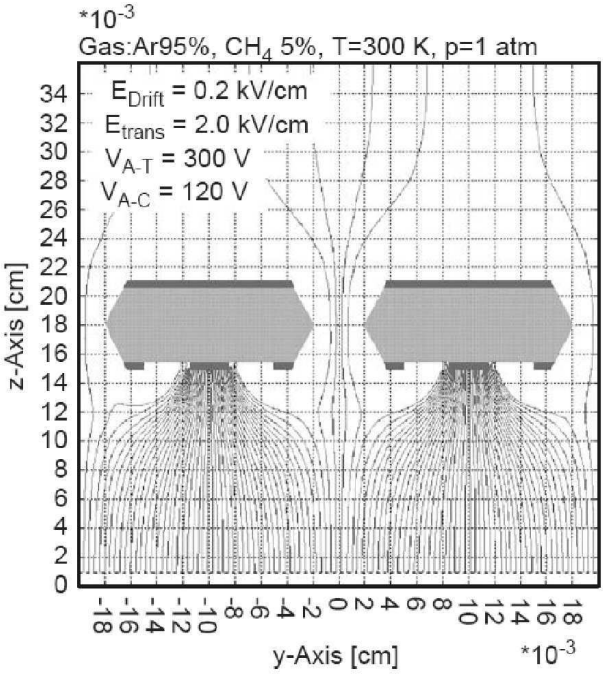

Figure 4.2 - Simulated paths of the ions produced in the stages below the R-MHSP. The simulations were done using GARFIELD software package [44].

4.2 Experimental setup

The measurements done with the R-MHSP have all taken place at the facilities of the Radiation Detection Lab at the Weizmann Institute of Sciences, in Israel. This group has

a long tradition in the field of radiation detection and provided all the necessary equipment and support required to test the operation of the R-MHSP.

The vacuum chamber used for the testing of the R-MHSP was already developed for other projects, described in [70]. The several elements of the detector were prepared as described in section 3.2.1 and were later stacked in one of the flanges used to seal the vacuum chamber. The sealing of the vacuum chamber was done using Viton O-rings and the detector was operated in continuous flow mode, with a mixture of argon and CH_4 in the relative percentages 95%-5%. The gas mixture was controlled by two mass flow controller (MFC) valves that regulated the admission of these two gases in the detector. The primary electron current was extracted from a CsI semi-transparent photocathode placed at an appropriate distance from the top element of the R-MHSP, defining the drift region of the detector.

The electrodes of the detector were either polarized independently using CAEN N471-A power supplies or, when the experimental requirements would allow it, using a voltage divider network powered by a single power supply.

The currents at the several electrodes of the detector were either recorded with electrometers in the electrodes connected to the ground reference or by measuring the voltage drop at the terminals of a resistor, for the electrodes placed at high voltage, as described in 3.6.

4.3 Results

4.3.1 Ion blocking with the R-MHSP

The first step taken to evaluate the feasibility of the R-MHSP concept was to establish its ion blocking properties. This was done using the setup depicted in figure 4.3 and composed by a semi-transparent photocathode, a Micro-Wire Proportional Chamber (MWPC) placed between two metallic meshes ($Mesh_1$ and $Mesh_2$), an R-MHSP and an ion collecting mesh ($Mesh_3$). The semi-transparent CsI photocathode was deposited on a UV transparent window (pre-evaporated with a thin layer of aluminium as described in chapter 3). $Mesh_3$ was placed 1.5 mm apart the top electrode of the R-MHSP and was used to collect the ions produced at the MWPC and that crossed the R-MHSP. An UV

lamp was used to promote the extraction of the primary photoelectron current from the semitransparent photocathode.

In this setup the MWPC acts solely as an ion source: the photoelectrons extracted from the CsI photocathode reach the MWPC and are multiplied in the vicinity of the anode wires. A fraction of the ions produced in the avalanches near the MWPC wires were transferred to the region between the MWPC and *Mesh*$_2$ and, by action of the electric fields E_3 and E_{TRANSF}, reached the R-MHSP.

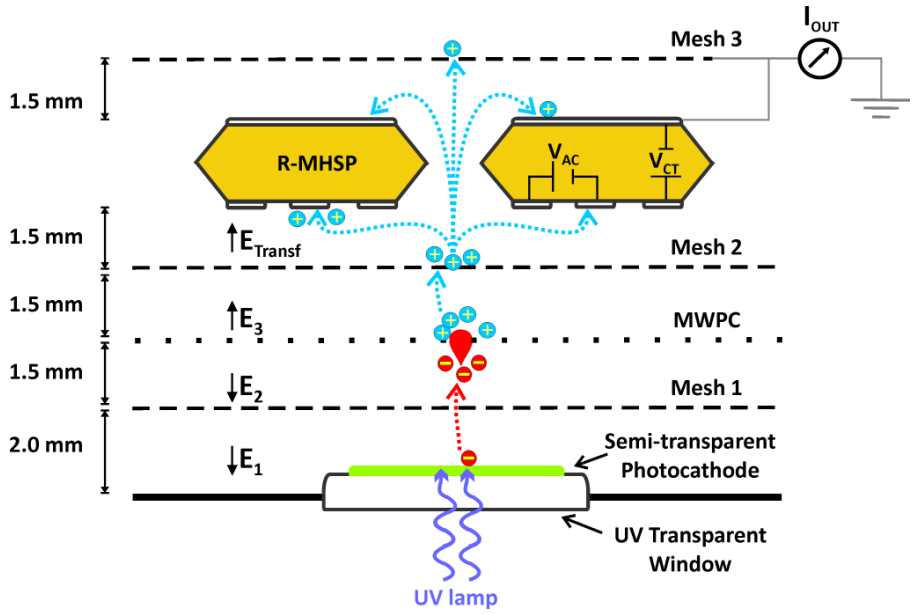

Figure 4.3 - Setup used for the measurement of the ion blocking properties of the R-MHSP.

Prior to each measurement, the amount of ions that reached the R-MHSP, I_{IN}, was determined by inter-connecting all the R-MHSP electrodes and measuring the current in these electrodes while maintaining the E_1, E_2, E_3 and E_{TRANSF} field configuration constant. The amount of ions crossing through the holes of the R-MHSP, I_{OUT}, was dependent on the reverse voltage across the strips of the R-MHSP and was continuously measured during our experiments. The *ion transparency* of the R-MHSP was defined as the fraction of ions that crossed the R-MHSP and calculated as the ratio between the ions coming out the holes of the R-MHSP, I_{OUT}, and the ions that reached the R-MHSP, I_{IN}:

$$\text{Ion Transparency} = \frac{I_{OUT}}{I_{IN}} \tag{4.1}$$

In order to ensure that I_{OUT} represented the current of ions coming out of the holes of the R-MHSP and to eliminate the influence of the electric field between the top electrode of the R-MHSP and $Mesh_3$, these two electrodes were inter-connected and I_{OUT} represented the current measured in these two electrodes.

The results obtained for the ion transparency are presented in the chart of figure 4.4 and demonstrate the ion blocking capabilities of the R-MHSP; reductions by more than 2 orders of magnitude in the *Ion Transparency* are obtained with the reverse polarization of the strips, relatively to the GEM mode operation of the R-MHSP (for $V_{A-C} = 0$ V the MHSP acts as GEM: the only multiplication region is the one inside the holes of the MHSP).

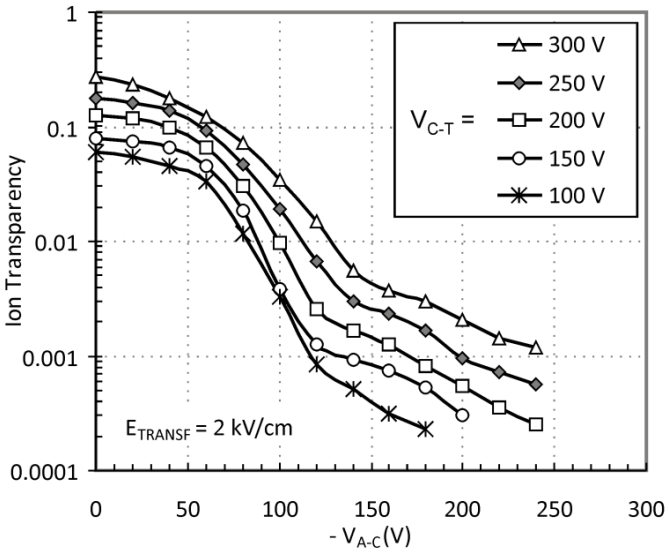

Figure 4.4 - Ion transparency of the R-MHSP as a function of the reversed voltage across the strips, for different voltages across the holes and for a transfer field of 2 $kV \times cm^{-1}$.

The same trend is valid for all values of voltage across the hole, but lower values of ion transparency are obtained for lower voltages across the R-MHSP holes, consistent with the charge transference properties across hole multiplier elements, described in chapter 2.

4.3.2 Single R-MHSP gain

Once established the ion-blocking properties of the R-MHSP the next step was to evaluate the charge gain obtained with the MHSP operating in the reverse mode. In order to measure the charge gain of the R-MHSP the setup inside the vacuum chamber used in the previous measurements was changed to one depicted in figure 4.5:

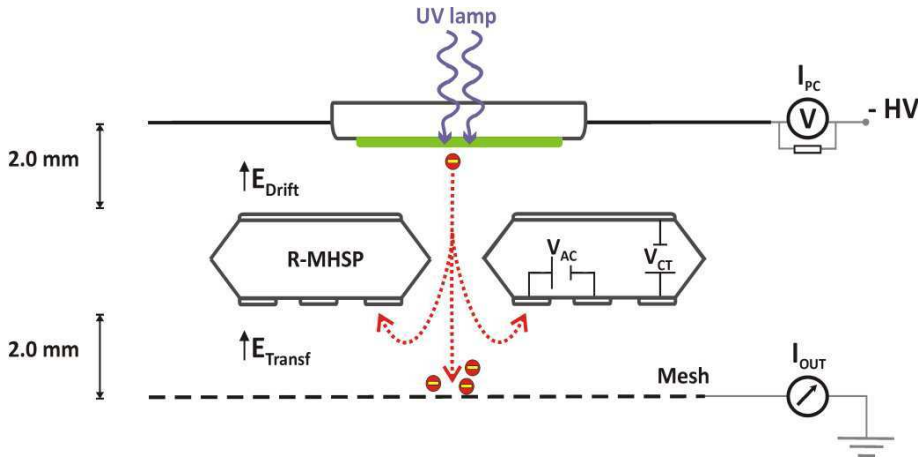

Figure 4.5 - Experimental Setup used for the measurement of the R-MHSP gain. A CsI semi-transparent photocathode deposited in a quartz window was used as a source for the primary electron current in charge mode.

The R-MHSP was placed between a semi-transparent CsI photocathode and a metallic mesh, 2.0 mm apart each of these elements. The CsI photocathode was irradiated with the UV radiation from an Hg(Ar) lamp, promoting the extraction of a current of photoelectrons, I_{PC0}. The electric field intensity in the region between the photocathode and the top electrode of the R-MHSP (0.5 $kV \times cm^{-1}$) assures that the current extracted from the photocathode corresponds to the plateau region of the curve in figure 2.10 ensuring a stable primary current during our measurements. The photoelectrons emitted from the CsI photocathode are focused and multiplied at the holes of the R-MHSP. The extraction field between the bottom of the R-MHSP and the *Mesh*, E_{TRANSF} = 2.0 $kV \times cm^{-1}$, ensures that the charge multiplied in the holes of the R-MHSP is extracted from them and collected at the metallic mesh.

E_{TRANSF} is dependent on the voltage difference between the *Mesh* (placed at ground potential) and the anode-cathode bottom plane of the R-MHSP. During our measurements the voltage at the anodes of the R-MHSP was changed while the one at

the cathodes was kept constant, affecting the potential at the anodes-cathodes plane. In order to account for this influence in the value of E_{TRANSF} we've calculated the *Equivalent Potential*, V_{EQUIV}, at the anodes-cathodes surface of the R-MHSP using the formula[a]:

$$V_{EQUIV} = \frac{V_{CAT} \times W_{CAT} + V_{ANOD} \times W_{ANOD} + (V_{ANOD} + V_{CAT}) \times GAP}{PITCH} \tag{4.2}$$

In the expression above GAP stands for the gap between anodes and cathodes on the R-MHSP and PITCH is the distance between two consecutive cathodes. W_{ANOD} and W_{CAT} are, respectively, the widths of the anodes and cathodes and V_{ANOD} and V_{CAT} the voltages applied to these electrodes. The value of V_{EQUIV} obtained with the formula above (for each value of V_{ANOD}) was then used in the calculation of E_{TRANSF}.

The effective (or visible) charge gain of the R-MHSP is the ratio between the final current collected at the mesh of the detector, I_M, and the primary photoelectron current emitted from the photocathode for null voltages differences across the R-MHSP, I_{PC0}. The measurement of I_{PC0} was always done prior to the polarization of the R-MHSP to assure that there was no contribution of the ion back flow current.

$$G_{R-MHSP} = \frac{I_M}{I_{PC_0}} \tag{4.3}$$

Figure 4.6 presents the R-MHSP effective gain as a function of the reverse voltage between the strips of the R-MHSP, measured for several hole voltages, $V_{C\text{-}T}$, and for a transfer field of 2 $kV \times cm^{-1}$. All the curves follow the same trend and translate a strong reduction of the charge gain of the R-MHSP when increasing the reverse voltage across the strips. The values obtained for $V_{A\text{-}C} = 0$ V (similar to the ones obtained with a GEM) drop by as much as 2-3 orders of magnitude for $V_{A\text{-}C} = -200$ V across the strips.

[a] The expression is an adaptation of the one used in the determination of the drift field in Micro Strip Gas Chambers (MSGC) [83].

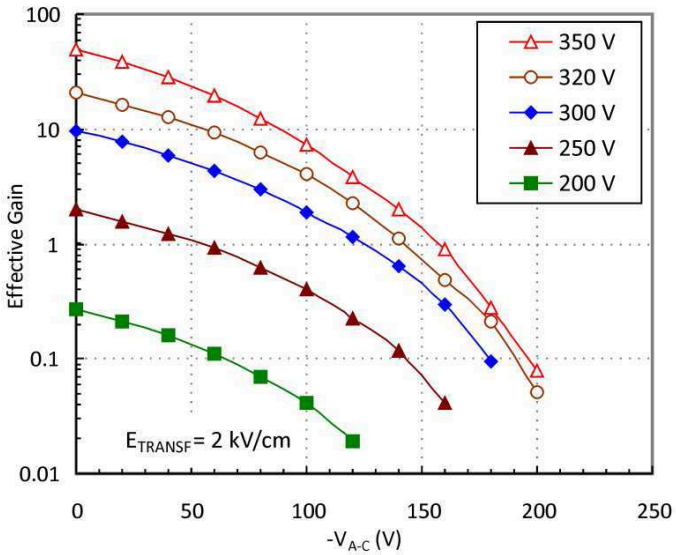

Figure 4.6 - Effective charge gain of the R-MHSP as a function of the reverse voltage, for different values of $V_{C\text{-}T}$.

The effective gain of the R-MHSP is a complex function of the voltage across the holes, $V_{C\text{-}T}$, and of the reverse voltage across the strips, $-V_{A\text{-}C}$. For null voltages across the strips, $V_{A\text{-}C} = 0$ V, the charge gain of the R-MHSP corresponds to the gain at its holes. The values of the effective charge gain of the R-MHSP, measured for $V_{A\text{-}C} = 0$ V and as a function of $V_{C\text{-}T}$, are presented in figure 4.7.

The fitting of an exponential curve to the experimental data points, figure 4.7, gives the expression that describes the charge gain of the R-MHSP for $V_{A\text{-}C} = 0$ V as a function of $V_{C\text{-}T}$:

$$G\,(V_{A\text{-}C} = 0\ \text{V}) = A_0 \times e^{B_0 \times V_{C-T}} \tag{4.4}$$

In the expression above A_0 and B_0 are empiric parameters, obtained from the fitting of an exponential curve to the experimental data points on figure 4.7.

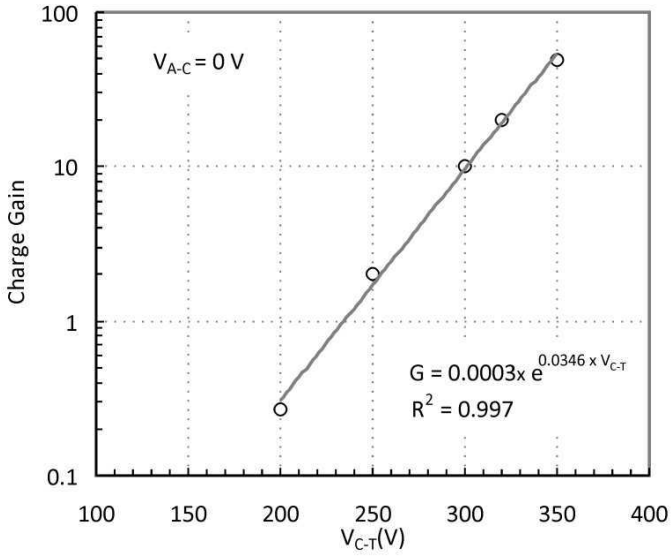

Figure 4.7 - Charge gain of the R-MHSP for V_{AC} = 0 V (GEM mode) and exponential curve fitting to the data points.

The results presented in figure 4.6 show a strong reduction in the effective or visible charge gain of the R-MHSP, i.e. a reduction on the charge collected at the metallic mesh of the setup depicted in figure 4.5, as a consequence of the polarization of the anode strips. The visible gain of the R-MHSP is dependent on the charge multiplication at the holes of the R-MHSP and on the extraction of the electrons from them.

In figure 4.8 we present the individual currents, measured at the electrodes of the R-MHSP, at the electron collecting mesh and at the semi-transparent photocathode of figure 4.5, as a function of V_{A-C}. The sum of the currents at the cathodes and at the electron collecting mesh, represented by the solid circles in the chart of figure 4.8, is almost constant, indicating that the charge multiplication at the holes of the R-MHSP is not affected by the increase in V_{A-C}. The major effect of the polarization of the anode strips at a lower potential that the cathodes is the increase in the collection of the electrons multiplied in the holes of the R-MHSP at the nearby cathodes (open triangles on figure 4.8), causing the drop in the current measured at the electron collecting mesh (open squares in figure 4.8).

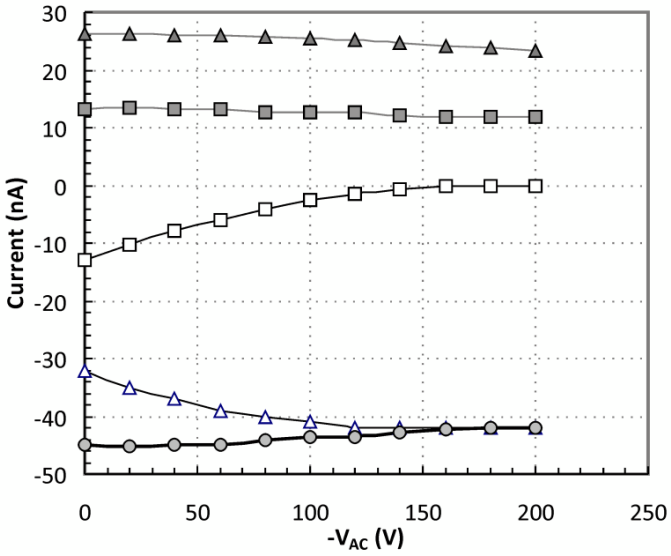

Figure 4.8 – Currents recorded at the several electrodes of the setup used for the measurement of the charge gain of the R-MHSP as a function of $V_{A\text{-}C}$. The solid triangles and squares represent the currents at the top electrode and at the semi-transparent photocathode, respectively. The open squares and triangles represent the currents measured at the electron collecting mesh and at the cathodes, respectively. The solid circles represent the sum of these last two currents. The results were obtained for $V_{C\text{-}T}$ = 250 V, E_{DRIFT} = 0.5 kV × cm^{-1} and E_{TRANSF} = 2 kV × cm^{-1}.

Although the multiplication inside the holes of the R-MHSP is not affected by the polarization of the anode strips, the visible gain, measured at the electron collecting mesh, is affected by the increase in $V_{A\text{-}C}$ according to the expression:

$$G(V_{C-T}, V_{A-C}) = A_0 \times e^{B_0 \times V_{C-T}} \times e^{-\gamma \times V_{A-C}^2} \qquad (4.5)$$

were A_0 and B_0 are the same as in (4.4) and γ (=15×10^{-5}) was adjusted to provide the best fit of equation (4.5) to the data points of figure 4.6 (presented again on the chart of figure 4.9). The expression above allows the calculation of the visible gain of the R-MHSP as a function of V_{CT} and V_{AC} (for a transfer field of 2 kV × cm^{-1}, as the one used in our measurements).

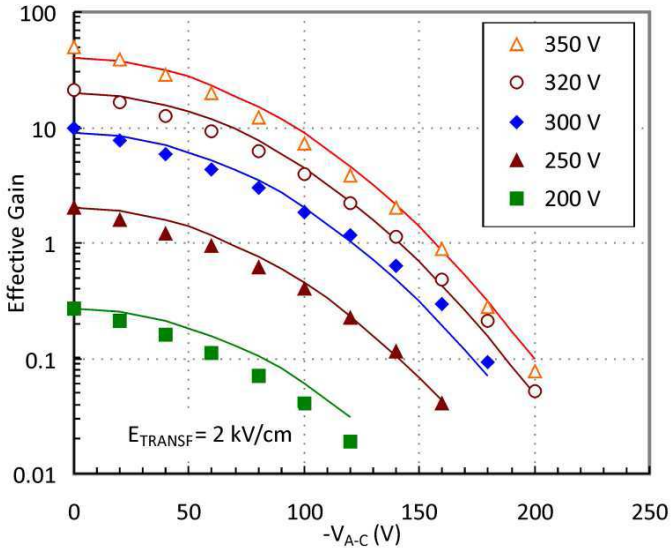

Figure 4.9 - Curve fitting of equation 4.5 (solid lines) to the experimental data points measured for the charge gain of the R-MHSP, for different values of V_{C-T}.

The charge gain and ion transparency of the R-MHSP are affected in a similar manner, decreasing when the reverse voltage across the strips is increased. The operation of the R-MHSP will therefore represent a compromise between these two quantities. In order to achieve the best compromise between visible gain (figure 4.6) and ion suppression (figure 4.4) obtained with the R-MHSP we've calculated the ratio between these two quantities, for the common operational voltages and for $E_{TRANSF} = 2\ kV \times cm^{-1}$. This ratio, figure 4.10, presents a maximum for values of $-V_{A-C}$ between 100 and 150 V indicating that is the region where one would expect to obtain better values of ion back-flow suppression, corresponding to the conditions of low ion transparency combined with less reduction of the transference of the electrons through the R-MHSP.

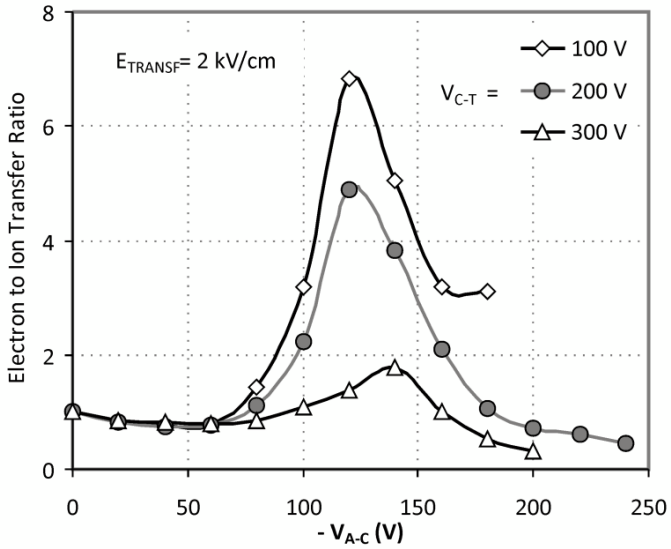

Figure 4.10 - Electron to Ion Transfer ratio.

4.3.3 Charge gain of the first element of the cascade

Since the R-MHSP is to be employed as the first element of a cascade of gaseous multipliers its charge gain is determinant in the overall detection efficiency of the detector. One could assume that a charge gain above the unity is sufficient to assure that all the events are properly detected. This is not always true, since the visible charge gain is an average gain, resulting from averaging the several individual avalanches suffered by each electron of the primary electron cloud. The charge gain of the R-MHSP is of particular relevance in the detection of single electron or low ionizing radiation. In these situations it is necessary to assure that the charge gain at the R-MHSP is enough so that, at least, one electron is always transferred from the R-MHSP to the next stage of the cascade of multipliers or else the information about the event will be lost.

For single electrons conditions the probability of obtaining a certain number (q) of electrons in an avalanche, is given by a Polya distribution [3] [84]:

$$P(q) = \frac{1}{Q} e^{\frac{-q}{Q}} \tag{4.6}$$

where Q is the average gain and q is the gain of each individual avalanche (in the case of single electron conditions, q represents the number of electrons in the avalanche following the multiplicative process).

Due to the exponential nature of the Polya distribution most of the single-electrons will suffer low gain multiplication processes and the probability that the avalanche is constituted by more than 1 electron is strongly dependent on the average gain. The probability of obtaining at least 1 electron in the avalanche for an average gain of 10 is of ≈ 92%. For an average gain of 20 this probability is of 96%, reaching values of 99% for average gains of 100.

4.3.4 Incorporation of the R-MHSP in a cascade of electron multipliers

Once the charge gain and ion blocking properties of the R-MHSP were determined we've incorporated it as the first element of cascade of 2 gas electron multipliers (2-GEM). The setup, depicted in figure 4.11, was assembled in the vacuum chamber and operated in Ar-5% CH_4 at atmospheric pressure in flow mode.

The photoelectrons extracted from the semi-transparent photocathode are focused and multiplied in the holes of the R-MHSP, from where they are extracted and transferred to the next element (GEM 1). Both GEM are polarized with the same voltage, ΔV_{GEM}. The electron current is amplified in each stage of the detector and finally collected at the mesh placed after GEM 2. The current in this mesh, placed at ground voltage, was recorded with an electrometer (Keithley 610 C). In order to fully evaluate the electron current coming out of the holes of GEM 2, the current in the bottom electrode of GEM 2 was also recorded, by measuring the voltage drop across a resistor connected in series to the power supply.

The currents collected at the electron collecting mesh and at the bottom electrode of GEM 2 were used to evaluate the total gain of the detector according to the expression:

$$G_{Detector} = \frac{I_{Mesh} + I_{Bot}}{I_{PC_0}} \tag{4.7}$$

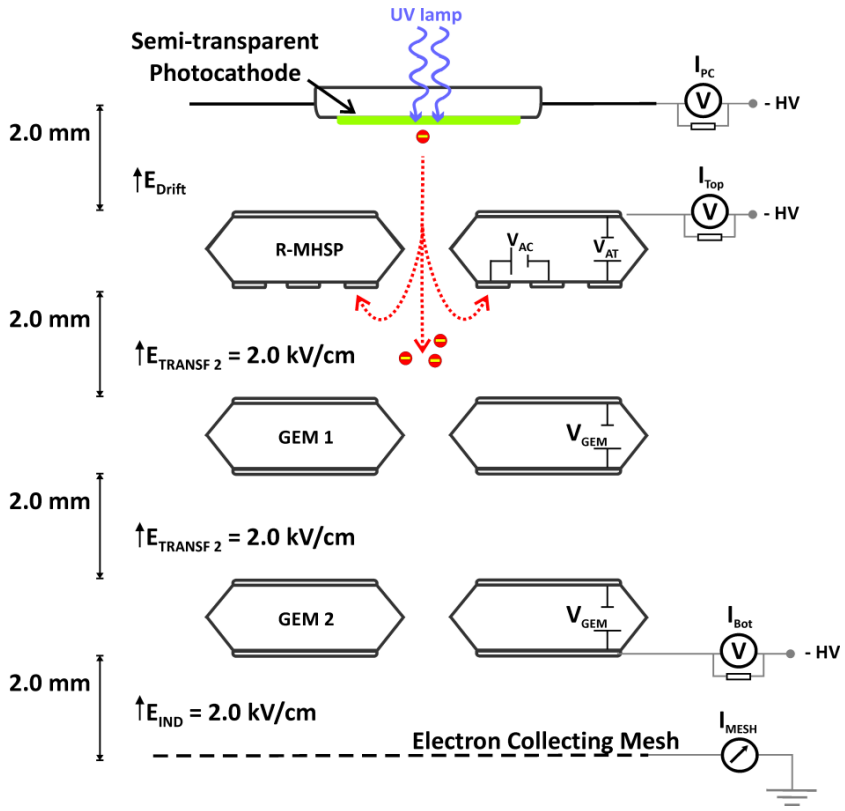

Figure 4.11 - Schematic representation of the detector used for measurement of the IBF reduction properties of the R-MHSP in a cascade of gaseous multipliers. The cascade was composed of an R-MHSP, followed by 2 GEM. The spacing between elements of the cascade was 2.0 mm. A semi-transparent photocathode was used for the production of primary charge.

The semi-transparent photocathode is irradiated with a constant flux of UV photons from an Hg(Ar) lamp, producing a primary photoelectron current, I_{PC0}, extracted by the electric field in the drift region of the detector, E_{DRIFT}. This current, which is only dependent on the UV lamp intensity and on the electric field intensity at the surface of the photocathode is kept constant during the measurements. The changes observed in the total current at the photocathode (I_{PC}) during the measurements are solely due to the current of ions coming out of the R-MHSP holes and reaching the semi-transparent photocathode, moving in the opposite direction to the photoelectron current. From the knowledge of I_{PC} (constantly monitored during the measurements) and I_{PCO} (recorded prior to each series of measurements, for no charge multiplication conditions) the current of ions that reaches the semi-transparent photocathode is determined:

$$I_{ION} = I_{PC} - I_{PC_0} \tag{4.8}$$

The knowledge of I_{ION} and of the final electron current at the anode of the detector I_{OUT} allowed the calculation of the IBF fraction that reaches the photocathode of the detector:

$$IBF = \frac{I_{ION}}{I_{OUT}} = \frac{I_{PC} - I_{PC_0}}{I_{mesh} + I_{Bot}} \tag{4.9}$$

In order to discard the contributions of the induction field E_{IND} on the charge collected at the electron collecting mesh we've also measured the charge collected at the bottom electrode of GEM 2 and included this contribution in I_{OUT}.

The results for the fraction of ions backflowing (IBF) that reaches the drift region of the detector and is collected at the semi-transparent photocathode are presented in figures 4.12 and 4.13 as a function of the voltage across the strips and of the total gain of the detector. The results were obtained for a drift field of 0.5 $kV \times cm^{-1}$.

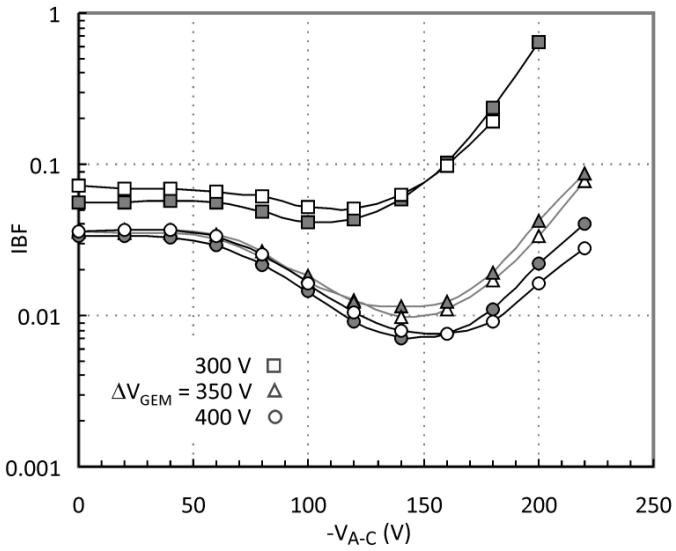

Figure 4.12 - IBF measured with the R-MHSP + 2-GEM detector depicted in figure 4.11, as a function of the reverse voltage across the R-MHSP strips. The ion current was measured at the semi-transparent photocathode electrode. The open symbols were measured for V_{C-T} = 300 V while the solid ones correspond to V_{C-T} = 250 V.

For V_{A-C} = 0 V the R-MHSP acts as a GEM and the IBF measured is equivalent to the one obtained with 3-GEM. [70]. The increase into the reverse voltage across the strips translates into an initial decrease in the IBF, as more ions are trapped at the R-MHSP anodes, until the minimum value of IBF is reached. For high voltages across both GEM, ΔV_{GEM} > 300 V, the minimum IBF is obtained for $V_{A-C} \approx$ -150 V, a value that matches the maximum in the electron to ion transfer ratio curve of the R-MHSP (see figure 4.10).

Once the minimum value of IBF is reached, the effect of the electron blocking becomes predominant in equation 4.9 and the values of IBF (that translate the number of ions reaching the drift region for each electron collected at the anode of the detector) start to increase, due to the reduction in the electrons transferred to the GEM, despite the continuous decrease in the absolute number of ions crossing the R-MHSP.

A similar behavior to the one reported here was measured by the author of [85] in an effort to minimize the ion back flow in a R-MHSP + 2-GEM operating in a 4 T magnetic field. The results obtained in [85], for an E_{DRIFT} of 2.0 kV×cm^{-1}, present a similar behavior as the ones of figure 4.12 with the minimum value of ion *backdrift* measured for V_{A-C} = - 160 V. The authors of this work reported little or no influence of the magnetic field on the ion back flow.

The graphic in figure 4.13 presents the IBF of the R-MHSP + 2-GEM detector as a function of the total gain of the detector, calculated according to equation 4.7. The curves on figure 4.13 were obtained by changing the voltage across the strips, while V_{C-T} and ΔV_{GEM} were kept constant for each of the curves. The first points to be acquired were measured at low values of V_{A-C} and correspond to the points with high charge gain on the chart above. Increasing $-V_{A-C}$ reduces the IBF due to the trapping of the positive ions while simultaneously reduces the charge gain of the detector. The minimum IBF value reached for each curve is dependent on ΔV_{GEM} but seems to stabilize for values higher that 300 V and is almost independent on the voltage at the holes of the MHSP, V_{C-T}. After the minimum IBF value is reached, the IBF increases strongly, due to the reduction in the electron transparency of the R-MHSP.

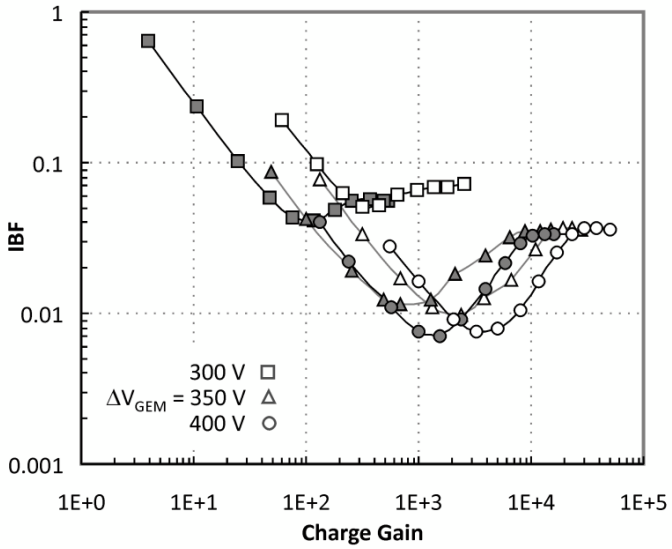

Figure 4.13 - IBF of the R-MHSP + 2-GEM detector, as a function of the total charge gain of the detector, changed by varying the reverse voltage across the R-MHSP. Lower values of V_{A-C} correspond to higher charge gain values. Open symbols were measured for V_{C-T} = 300 V while the solid ones at V_{C-T} = 250 V.

The lowest value of IBF measured was of 0.007, measured for V_{A-C} = -140 V and ΔV_{GEM} = 400 V across each of the 2 GEM of the detector. This IBF value represents a decrease by a factor of ≈ 4 relatively to the value obtained for V_{A-C} = 0 V.

Despite the good values of IBF measured with the R-MHSP coupled to a 2-GEM detector, the results were obtained at V_{A-C} = -140 V and V_{C-T} = 250 V. The charge gain of the R-MHSP for these voltages is below 1 and is therefore insufficient for the proper operation of the R-MHSP as the first element of the detector, particularly in single electron detection.

4.3.5 Double R-MHSP

The poor charge gain obtained with the R-MHSP led us to try a different approach: the inclusion of a second R-MHSP in the detector to trap the positive ions using 2 R-MHSP instead of only one, easing the reverse voltage across each R-MHSP and therefore increasing the charge gain on the first element of the detector to acceptable levels.

The detector presented in figure 4.11 was slightly modified in order to incorporate another R-MHSP element, resulting in the setup depicted in figure 4.14 and composed by 2 R-MHSP followed by a 2-GEM.

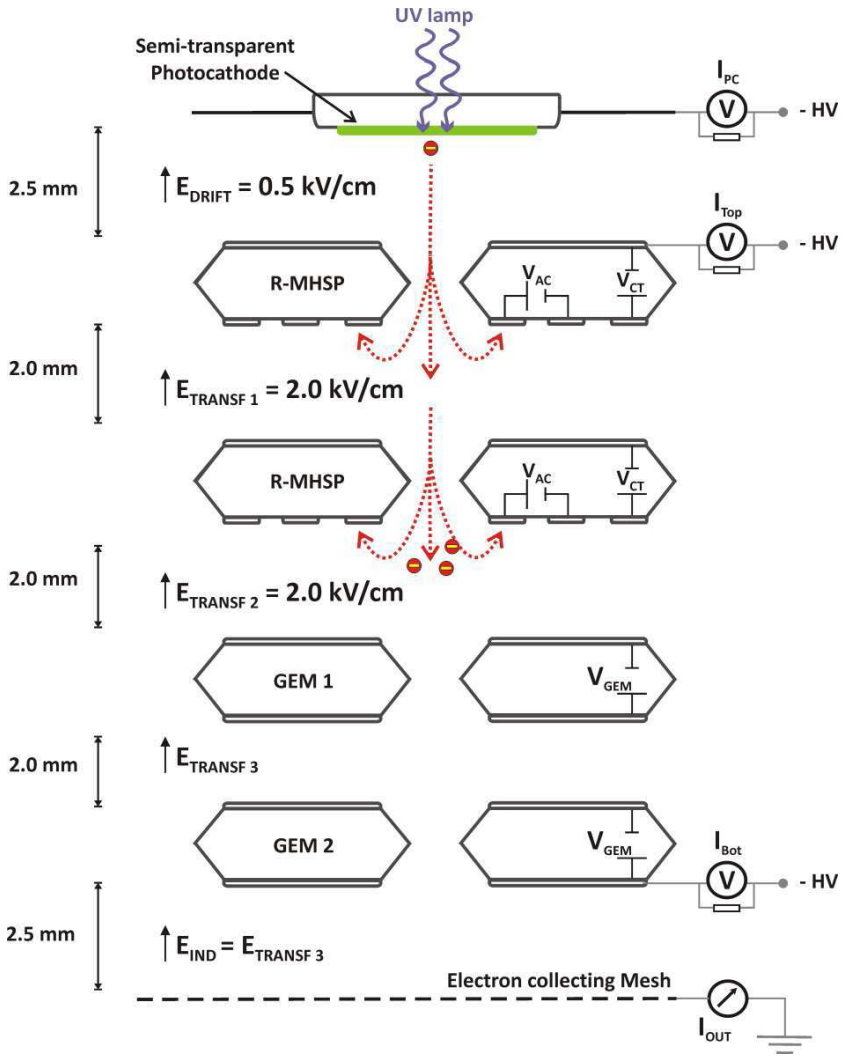

Figure 4.14 - Schematic representation of the 2-R-MHSP + 2-GEM detector.

The inclusion of a second R-MHSP in the test chamber required some minor adjustments relative to the spacing between each element and to the polarization scheme that was slightly altered by using a resistive network to polarize the 2 GEM and to establish the transfer field between them. Therefore the transfer field between GEM 1 and GEM 2, $E_{TRANSF3}$, was not kept constant during the measurements but was

proportional to ΔV_{GEM} (both GEM were polarized with the same potential). For ΔVGEM = 400 V the intensity of $E_{TRANSF3}$ was 2.0 kV × cm^{-1}. The electron collecting mesh and the bottom electrode of GEM 2 were not part of the resistive network and the currents on these two electrodes were obtained by measuring the voltage drop across a resistor in series with the power supply. The induction field between GEM 2 and the electron collecting mesh had always the same value as $E_{TRANSF3}$ and the drift field on the detector was set to 0.5 kV × cm^{-1}.

The expressions used for the calculation of the effective gain and IBF of the detector were the same as in equations 4.7 and 4.9, used for the R-MHSP + 2-GEM detector.

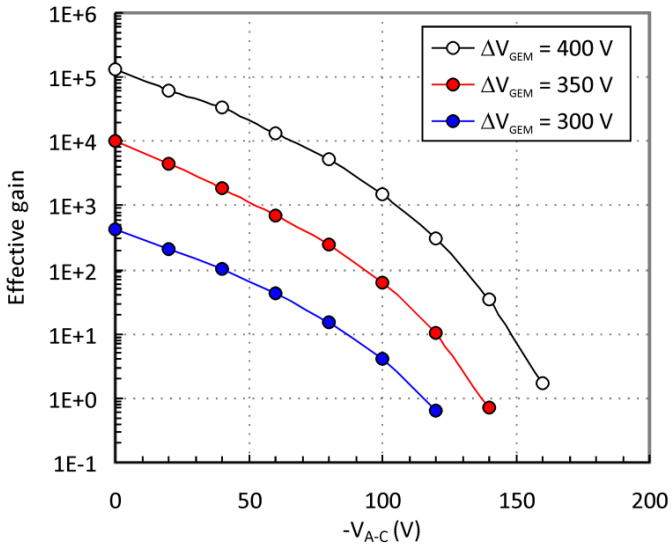

Figure 4.15 - Effective Charge gain of the 2-R-MHSP + 2-GEM detector as a function of the reverse voltage across the strips of the MHPSs for V_{C-T} = 250 V on the two R-MHSP and for different voltages across the GEM (both GEM were polarized with the same potential).

Figure 4.15 presents the total charge gain of the 2-R-MHSP + 2-GEM detector as a function of the reverse voltage at the strips of the two R-MHSP (these two elements were polarized with the same potentials). As expected, the charge gain of the detector is strongly dependent on the ΔV_{GEM} and reduces with the increase of the reverse voltage difference between anodes and cathodes of the R-MHSPs.

The IBF measured with the 2-R-MHSP + 2-GEM detector (figure 4.16) is, as expected, dependent on the reverse voltage across the strips of the R-MHSPs and on the voltage

difference used to polarize the GEM. The lowest values of IBF, 0.0006, were obtained for ΔV_{GEM} = 400 V.

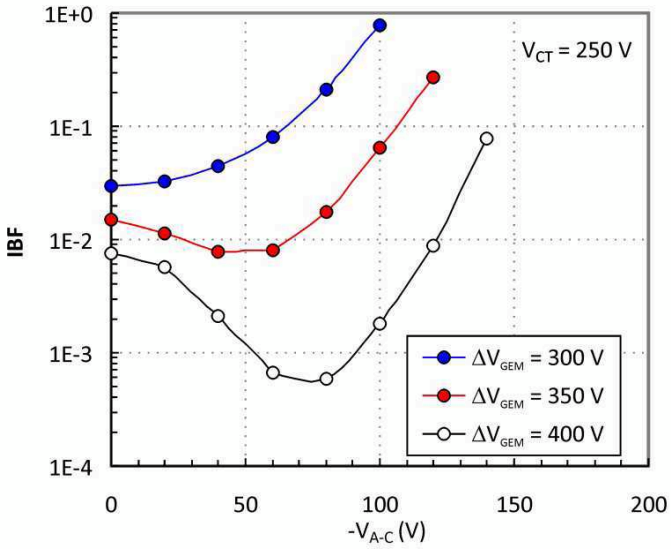

Figure 4.16 - IBF of the 2 R-MHSP + 2-GEM detector as a function of the reverse voltage across the strips for different ΔV_{GEM} voltages. Curves were obtained for V_{C-T}=250 V across the holes of the two R-MHSP.

The results for the IBF, presented in figure 4.16 for different $\Delta V_{GEM,}$ show that, for each curve, the minimum IBF value obtained is dependent on the voltage used to polarize the GEM, that is, on the charge gain on the 2-GEM. This is explained if we take into account the origin of the positive ions that contribute to the IBF. A fraction of these ions is produced at the holes of the R-MHSPs and is not trapped by the polarization of the strips. This fraction is dependent on the V_{C-T} voltage difference, which for the measurements above was of 250 V. The remaining ions contributing to the IBF are produced at the holes of the GEM and are therefore subject to the action of the R-MHSPs. The IBF reflects these two contributions as well as the total gain of the detector. For higher values of ΔV_{GEM} a larger fraction of the ions contributing to the IBF is subject to the effect of the R-MHSP, as more ions are produced at the holes of the 2-GEM. The action of the polarization of the strips is more evident for these voltages as it is indicated in the curves on figure 4.16: for ΔV_{GEM} = 300 V there is almost no

reduction in the IBF with the increase in $-V_{A-C}$, while for $\Delta V_{GEM} = 400$ V the suppression is of one order of magnitude.

An exciting feature observed with the 2-R-MHSP + 2-GEM detector was that the minimum values of IBF in the curves of figure 4.16 were obtained at lower values of $-V_{A-C}$ that in the single R-MHSP + 2-GEM detector. This fact, which we attribute to an improved ion trapping with the 2-R-MHSP instead that just with one, allows operating the R-MHSP at lower values of $-V_{A-C}$, corresponding to higher charge gains. The charge gains (figure 4.6) measured for $V_{A-C} = -80$ V are almost one order of magnitude higher that the ones obtained for $V_{A-C} = -140$ V (value for which the IBF reached its minimum in the single R-MHSP + 2-GEM detector).

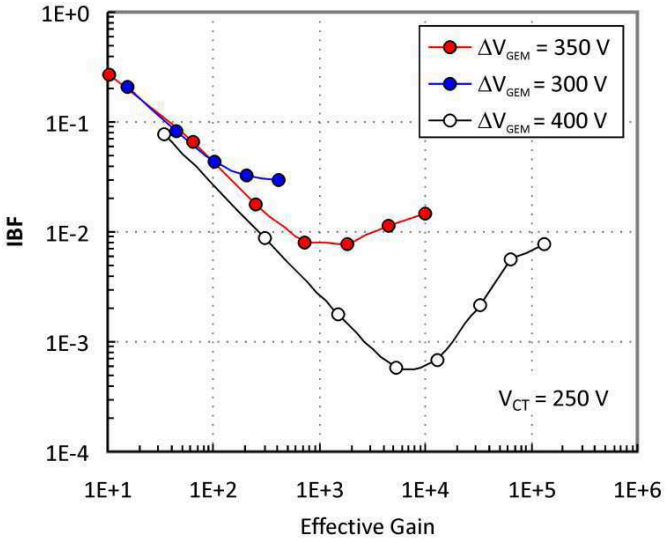

Figure 4.17 - IBF of the 2-R-MHSP+2-GEM detector as a function of the total gain of the detector, for different values of ΔV_{GEM}.

The results for the IBF obtained with the 2-R-MHSP + 2-GEM detector are presented in figure 4.17 as a function of the total gain of the detector and show that the minimum value of IBF for each curve is dependent on the total charge gain of the detector.

The minimum value of IBF measured, 0.0006 (that represents 6 ions reaching the drift region for each 10^4 electrons collected at the anode of the detector) was, at the time it was obtained, a record-breaking value for IBF reduction in gaseous detectors operating

in DC mode. This value was obtained for a reverse voltage of 80 V across the strips of each MHSP and for V_{C-T} = 250 V, corresponding to a charge gain on the first element of the detector of approximately 0.6.

This value of charge gain is insufficient for the efficient detection of single electrons deposited in the drift region and may degrade the energy resolution for highly ionization particles detected but can be increased, without compromising the IBF value, by operating the R-MHSPs at higher V_{C-T}. At the time of the measurements presented here this was not possible due to the lack of good quality MHSP to proceed with the studies. From the chart of figure 4.13, were we present the IBF as a function of V_{A-C} for the single R-MHSP/2-GEM detector, one can conclude that the minimum value of IBF achieved whit the R-MHSP is not strongly influenced by V_{C-T} (at least not in the single R-MHSP configuration). It is therefore reasonable to assume that IBF values similar to the ones obtained for V_{C-T} = 250 V will be achieved at higher values of V_{C-T} and at higher gains on the R-MHSP (for V_{C-T} = 350 V and V_{A-C} = -80 V the charge gain in the R-MHSP is above 10, a value that assures a 90% detection efficiency for single electron, as discussed above).

Despite these limitations, the results obtained constitute a step forward on the IBF reduction in the operation of gaseous detectors and are passive of implementation, whenever the reduction of the IBF for highly ionizing radiation is required.

4.4 Further Progress with the R-MHSP

Despite the low charge gains experimentally achieved with the R-MHSP, the results presented here represented a new approach to the IBF reduction in gaseous detectors and motivated further improvements. The work presented in this chapter was later continued in [76] [86] [87], taking advantage of the production of a new batch of MHSP elements. In [76] the R-MHSP was operated at atmospheric pressure in Ar-5% CH_4, at V_{C-T} = 410 V and V_{AC} = - 70 V, corresponding to a charge gain of 20. In this reference the work on the suppression of the IBF went even further by combining the ion trapping at the strips of the R-MHSP with the natural ion suppression of the R-MHSP acting as the last element of the cascade [41]. In this work, with a single-R-MHSP + 2-GEM + MHSP detector, IBF values of 0.0015 were obtained for a drift field of 0.5 $kV \times cm^{-1}$ and

a total gain of 10^5. An IBF of .0002 was obtained with the same detector for a drift field of 0.1 $kV \times cm^{-1}$.

The work on the on IBF reduction with the Micro Hole and Strip Plate was continued by using this device in another configuration: the flipped-reversed MHSP (F-R-MHSP). In this configuration the F-R-MHSP was operated in the reverse mode but with its strips facing the drift region of the detector. With this setup not only the ions produced in the stages following the MHSP were trapped at the anode strips but also the ions produced at the holes of the F-R-MHSP itself [86]. Another major improvement of this configuration was the fact that the polarization of the anode strips had much less influence on the visible gain of the F-R-MHSP that in the R-MHSP. This series of R&D efforts were successful in the reduction of the IBF to 0.0002 at a gain of 10^5 in a detector composed by a F-R-MHSP + GEM + MHSP. These values later allowed the first time operation of a GPM coupled to a visible spectral range sensitive photocathode, operating in continuous mode and with single photon sensitivity [88].

5 PACEM DETECTOR FOR ION BLOCKING

5.1 Motivation

The limitations on the charge gain of the R-MHSP have triggered a new direction in our efforts to suppress the IBF in gaseous detectors. Cascaded gaseous multipliers rely on electric fields between the different elements of the detector to transfer the charge between each stage until the final collection at the anode of the detector. In this type of detectors the same electric fields that transport and multiply the negative electrons from the sensitive region of the detector to the collecting anode are also responsible for the movement of the positive ions in the opposite direction. In order to efficiently block the ions from reaching the sensitive regions of the detector a discontinuity in the electric field must be introduced in the detector, preventing the passage of the positive ions while at the same time providing a pathway for the electric signal to be transmitted. The introduction of a pulsed gate was one of the first advances in the suppression of ions [36] and was successful in blocking the IBF, up to 10^5 Hz. There is, however, great interest in achieving the reduction of the IBF at higher counting rates and even in DC mode. This was indeed implemented with the Photon Assisted Cascaded Electron Multiplier (PACEM), a detector developed to block the ion back flow in gaseous detectors operating in highly scintillating gases.

The innovative feature of the PACEM is the mechanism used to transfer the signal between the first and the second element of the multiplier cascade. As described in

section 2.2.6, a large amount of scintillation photons is emitted during the electron avalanches that take place at the holes of the Micro Hole and Strip Plate and in the region between the holes and the anode strips. Due to the strong charge multiplication that occurs in the vicinity of the anode strips the emission of photons by the gas molecules in this region is particularly intense.

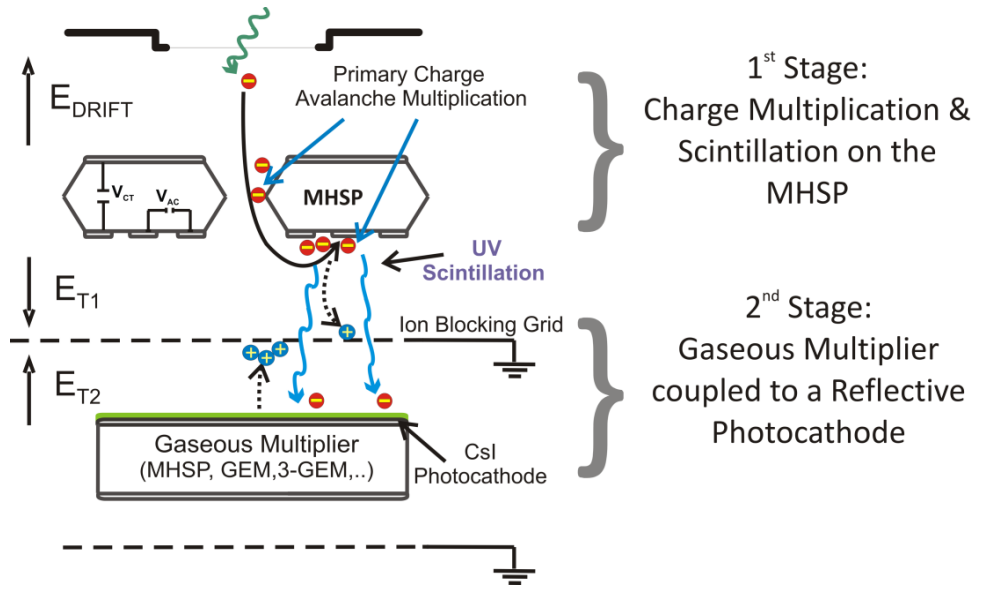

Figure 5.1 - Schematics of the operation of the PACEM detector. The scintillation produced on the 1st stage of the detector (MHSP) induces the extraction of the photo-electrons from the CsI photocathode deposited on the top of the 2nd element of the PACEM detector, being the photoelectrons directed to the holes of this second element and multiplied in it as well as in any subsequent elements by electron avalanche. The ion blocking grid will block all the ions that drift from the electrons avalanche produced in the elements below it.

The PACEM is a two step detector with a MHSP as the first stage. A metallic grid, with high optical transparency, is placed between the first and second stages of the detector, electrically isolating one from the other. The signal is transmitted from the first stage of the detector to the next one using the VUV scintillation produced during the electron avalanches that take place on the MHSP. A CsI reflective photocathode is placed on the top of the first element of the second stage of the PACEM. The VUV scintillation produced on the first stage of the detector, composed by an MHSP, promotes the extraction of photoelectrons from the CsI photocathode. These electrons are further multiplied on the second stage of the detector by charge avalanche mechanisms. Figure

5.1 presents a schematic representation of the operation of the PACEM, indicating the two stages that constitute this detector. The second stage, were the CsI photocathode is deposited can be constituted by any kind of gaseous electron multiplier (GEM, MHSP, 3-GEM, etc).

The ion blocking mesh in figure 5.1 is made of 80 μm stainless steel wires with 900 μm spacing and has an optical transparency of 84%. It assures that all the ions produced in the stages below the mesh are blocked while the photons emitted by the MHSP are transmitted. This represents a major advance relative to the work described in the previous chapter were, besides the contribution of the ions produced at the holes of the R-MHSP, the IBF also received the contribution of a fraction of the ions produced in the following stages of the detector. In the PACEM this last contribution is completely blocked and only the ions produced at the avalanches on the MHSP contribute to the IBF. As described in [41] from the total amount of ions produced on the MHSP only ≈ 20-40% flow through the holes while the remaining fraction is naturally trapped at the ion blocking grid and at the cathode strips of the MHSP.

One of the major considerations in the development of the PACEM detector is the efficiency with witch the signal is transferred from the first stage of the detector to the second stage, that we've defined as the optical gain, i.e., the number of photoelectrons extracted from the CsI photocathode per each primary electron deposited in the drift/absorption region of the detector.

$$\text{Optical Gain} = \frac{\text{Photoelectrons extracted}}{\text{Primary electrons}} \tag{5.1}$$

The optical gain is dependent on geometrical factors such as the solid angle covered by the CsI photocathode and on the optical transmission of the ion blocking grid but is mostly dependent on the total number of photons produced at the MHSP and on the efficiency with which the photoelectrons are extracted from the reflective photocathode.

5.2 Pulse mode operation in xenon

In order to demonstrate the feasibility of the PACEM concept, the detector depicted in figure 5.2 was assembled in the test chamber of the vacuum system described in 3.4 and operated in pulse counting mode. The PACEM detector of figure 5.2 is composed has

an MHSP ($MHSP_1$) as the first stage of the detector and another MHSP ($MHSP_2$) acting as the second stage. The detector was operated in xenon, at atmospheric pressure and irradiated with a Fe^{55} X-ray source. The entrance window of the test chamber was made of an aluminized Mylar foil, 25 μm thick and prior to the measurements the detector was evacuated to 10^{-6} mbar and then filled at the indicated pressure. The detector gain was calibrated by the injection of a known charge into the electronic chain using a calibrated pre-amplifier.

The voltages on the electrodes of $MHSP_2$ were not changed during the measurements and were set to: $V_{TOP} = 0$ V, $V_{CATHODE} = 370$ V and $V_{ANODE} = 570$ V, corresponding to $V_{C\text{-}T2} = 370$ V and $V_{A\text{-}C2} = 200$ V. The electric field in the drift region of the detector was 1.2 $kV \times cm^{-1} \times bar^{-1}$ while the transfer field E_{T1} was set at 3.0 $kV \times cm^{-1} \times bar^{-1}$ and E_{T2} was kept close to zero to assure good extraction efficiency and focusing of the photoelectrons into the holes of $MHSP_2$.

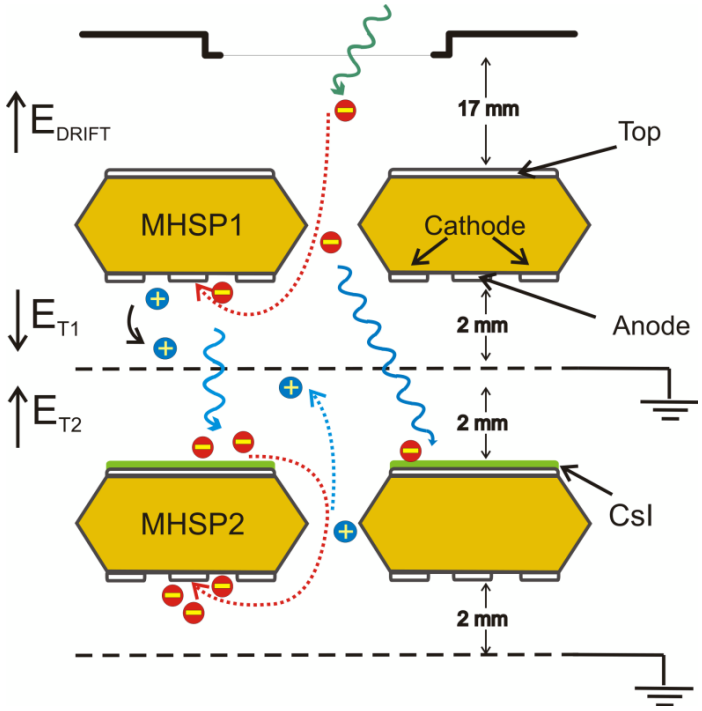

Figure 5.2 - Schematic representation of the detector used to demonstrate the PACEM concept. The detector is composed by 2 MHSP, separated by the ion blocking grid. The CsI photocathode is deposited on the top electrode of the second MHSP.

The operation of the PACEM was done by changing the voltages on $MHSP_1$ and measuring the pulse signals at the anodes of $MHSP_1$ and $MHSP_2$. The results obtained for the charge and optical gain of the PACEM detector are presented in figure 5.3, as a function of V_{A-C1} and for V_{C-T1} = 400 V, figure 5.3 a), and as a function of V_{C-T1} and for V_{A-C1} = 220 V, figure 5.3 b).

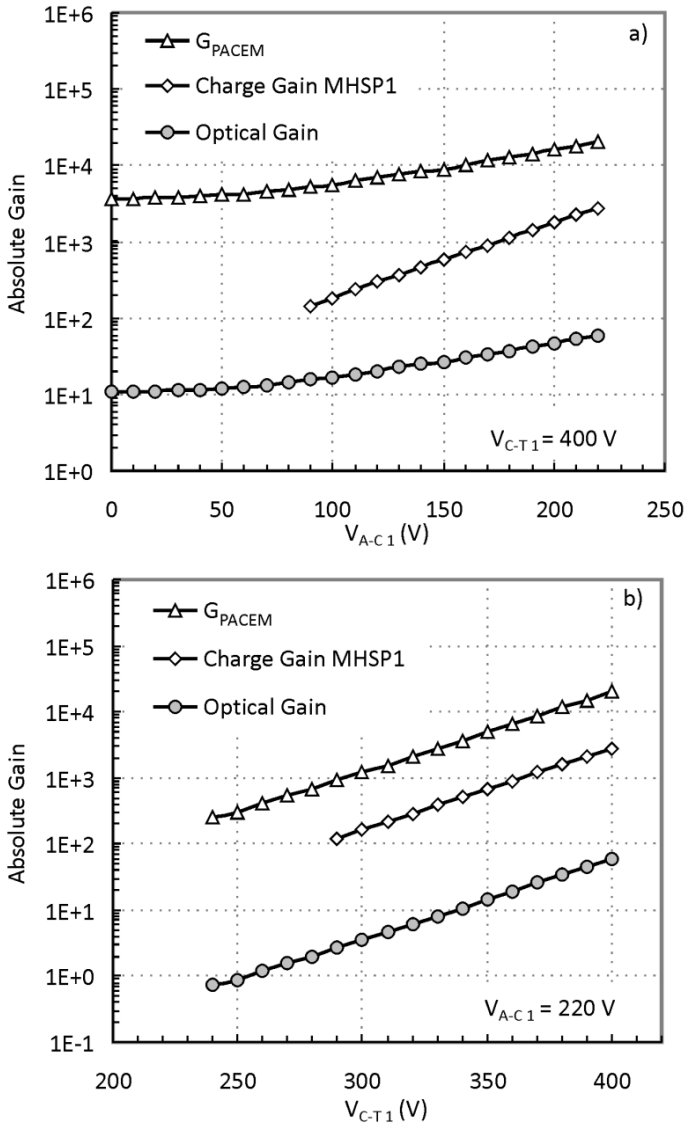

Figure 5.3 - Absolute gains obtained with 5.9 keV X-rays pulses recorded at the anodes of $MHSP_1$ (G_1) and $MHSP_2$ (G_{TOTAL}), as a function of V_{A-C1} and V_{C-T1}. V_{C-T2} = 370 V; V_{A-C2} = 200 V.

The total charge gain of the PACEM, G_{PACEM}, is obtained from the signal measured at the anodes of $MHSP_2$, were the final charge of the detector is collected, and is related to the gain that occurs in the optical stage of the PACEM detector through:

$$G_{PACEM} = \text{Optical Gain} \times G_{MHSP2} \tag{5.2}$$

The maximum values measured, above 10^4, are about one order of magnitude higher that the charge gains measured on the first MHSP (which are typical of the normal mode operation of this micro-patterned device in xenon [89] [90]).

The charge gain of $MHSP_2$, G_{MHSP2}, used in equation 5.2 to calculate the optical gain, was recorded in a previous measurement. In this measurement the ion collecting mesh and all the electrodes of $MHSP_1$ were grounded, transforming into a dead region the volume between the electron collecting mesh and the detector window. Some of the X-ray pulses from the Fe^{55} source that are not absorbed in this dead region are converted in the gap between the ion collecting mesh and the top electrode of $MHSP_2$. By action of an appropriate electric field ($0.1\ kV \times cm^{-1}$) the primary charge converted in this region is focused into the holes of $MHSP_2$ and multiplied in this micro-structure. The charge gain of $MHSP_2$ was measured for the same voltages as the ones used to obtain the results presented in figure 5.3, i.e. $V_{C\text{-}T2} = 370$ V and $V_{A\text{-}C2} = 200$ V. For these voltages the charge gain measured was of $G_{MHSP2} \approx 350$ and this was the value used to calculate the optical gain of the PACEM detector as presented on the charts of figure 5.3.

The differences in the behavior on the optical gain curves of figure 5.3 a) and b) are explained by the differences in the origin of the scintillation emitted by $MHSP_1$. In a) the voltage across the strips of $MHSP_1$ is changed while the voltage at the holes is kept constant ($V_{C\text{-}T1} = 400$ V). For these values of $V_{C\text{-}T1}$ there is already charge multiplication at the holes of $MHSP_1$ with the consequent production of secondary scintillation. This scintillation, emitted from the holes of $MHSP_1$, promotes the extraction of photoelectrons from the photocathode deposited on the top of $MHSP_2$, that contribute to the optical gain of ≈ 10 obtained for $V_{C\text{-}T1} = 400$ V and $V_{A\text{-}C1} = 0$ V on the chart of figure 5.3 (a). Once $V_{A\text{-}C1}$ starts to increase the electrons multiplied at the holes of $MHSP_1$ start being collected at the anodes and on their path produce additional electroluminescence that contributes to the increase in the optical gain. It is only for high values of $V_{A\text{-}C1}$ that the electrons extracted from the holes of $MHSP_1$ suffer

additional charge multiplication mechanisms and that the electron cloud starts growing exponentially with the consequent increase in the optical gain that, for higher values of $V_{A\text{-}C1}$, tends to an exponential dependence on $V_{A\text{-}C1}$.

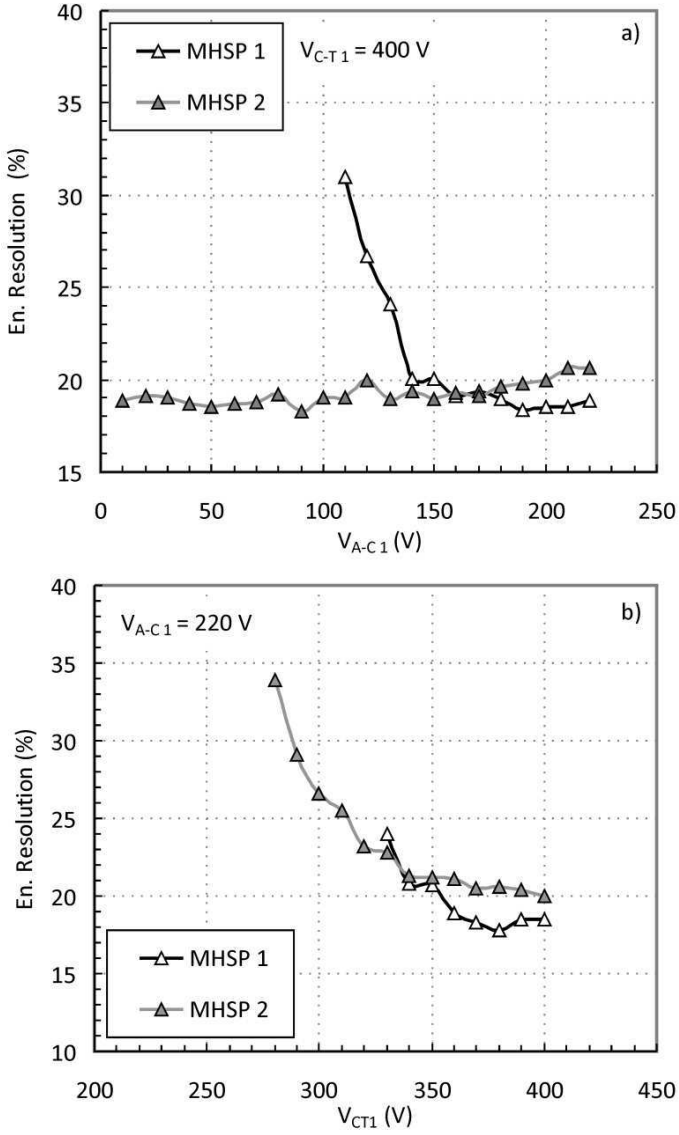

Figure 5.4 - Energy resolution measured at the anodes of $MHSP_1$ and $MHSP_2$, as a function of $V_{A\text{-}C1}$ and $V_{C\text{-}T1}$. The results were obtained by fitting the pulse height distributions to a Gaussian curve super-imposed on a linear background.

The results on figure 5.3 (b) were obtained with a different polarization scheme, and were recorded for a high value of V_{A-C1} (220 V) while changing V_{C-T1}. For this value of V_{A-C1}, the electrons multiplied in the $MHSP_1$ holes are extracted and further multiplied in the vicinity of the anodes, contributing to the exponential growth of the electron cloud and optical gain as the voltage difference across the holes, V_{C-T1}, increases.

The energy resolution, calculated from the pulse height distributions of the signals collected at the anodes of the two MHSP, are presented in figures 5.4, a) and b), as a function of V_{A-C1} and V_{C-T1}, respectively, for the same operational voltages as the results presented on the charts of figure 5.3.

The energy resolution of the PACEM detector, measured at the anodes of $MHSP_2$, does not degrades significantly from the one measured at the anodes of $MHSP_1$. For low values of V_{A-C1}, that correspond to low charge gains on $MHSP_1$, the energy resolution of the detector is significantly better that the one measured at $MHSP_1$. With the increase in V_{A-C1}, a small increase in the energy resolution of the PACEM detector is observed, going from 18% to 20%. This increase is most likely due to the increase in the statistical uncertainties caused by the additional charge multiplication mechanisms that occur when V_{A-C1} increases.

The pulse height distributions presented in figure 5.5 were recorded at the anodes of $MHSP_1$ (a) and $MHSP_2$ (b) for $V_{C-T1} = 400$ V, $V_{A-C1} = 160$ V, $V_{C-T2} = 370$ V and $V_{A-C2} = 200$ V, corresponding to a total gain on the detector of 10^4, a charge gain of 750 on $MHSP_1$ and an optical gain of 30. The noise on the pulse height distribution collected on $MHSP_2$ presented generally lower levels of electronic noise but this is most probably due to a feature of the particular MHSP used in this detector and not a physical property of the PACEM.

One very interesting feature of the PACEM, which could be an important advantage in some applications, and not yet explicitly mentioned, are the overall lower voltages required to polarize this detector and obtain high charge gains. In traditional cascaded gaseous multipliers the voltages are constantly growing from one element of the detector to the next, as a requirement to the transport of the charge through the detector. With the PACEM detector the presence of the ion blocking grid connected at ground potential and the fact that the signal transfer between stages of the detector is not mediated by the electric field, makes that the voltages used to polarize the second stage

of the detector are identical at the ones used to polarize the first stage. In a 2-stage detector as the one represented in figure 5.2, a total gain of 2×10^4 was achieved with a maximum voltage of 660 V applied on the detector (corresponding to V_{ANODE2}). If higher gains are required, a 3-element detector can be assembled, using the same voltages. This is a unique feature of the PACEM detector and, as far as we know, not shared by any other gaseous multipliers.

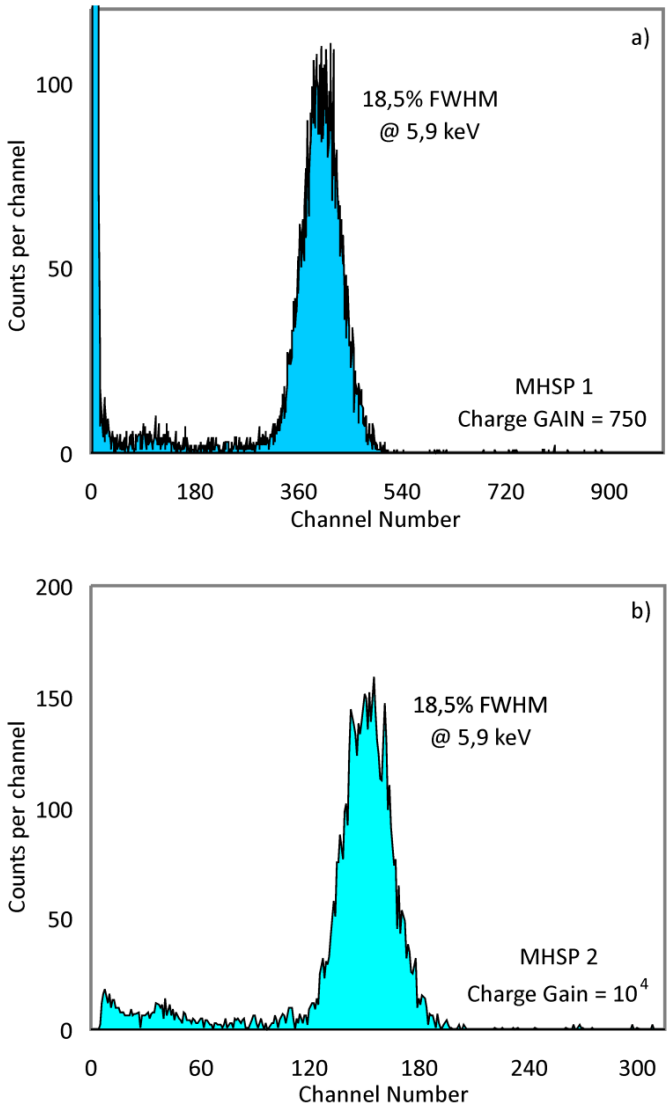

Figure 5.5 - Pulse-Height distributions from the 5.9 keV X-ray interactions in the drift region of the PACEM detector. The signals were collected at the anodes of $MHSP_1$ (a) and $MHSP_2$ (b).

5.3 Current mode measurements

The IBF reduction obtained with the PACEM detector can be easily evaluated operating the detector in current mode and measuring the currents on the several electrodes of the detector. In this mode of operation the primary charge is extracted from a CsI photocathode that is irradiated by UV photons emitted from a lamp placed externally to the detector. For this the setup used in the previous measurements was slightly modified in order to be operated in current mode. The major changes were the replacement of the Mylar entrance window of the test chamber by a 5 mm thick Suprasil® window, transparent to the UV photons emitted by the external lamp. The semi-transparent photocathode used for the production of the primary charge was deposited on the surface of another 5 mm thick window, placed 10 mm apart from the top electrode of $MHSP_1$.

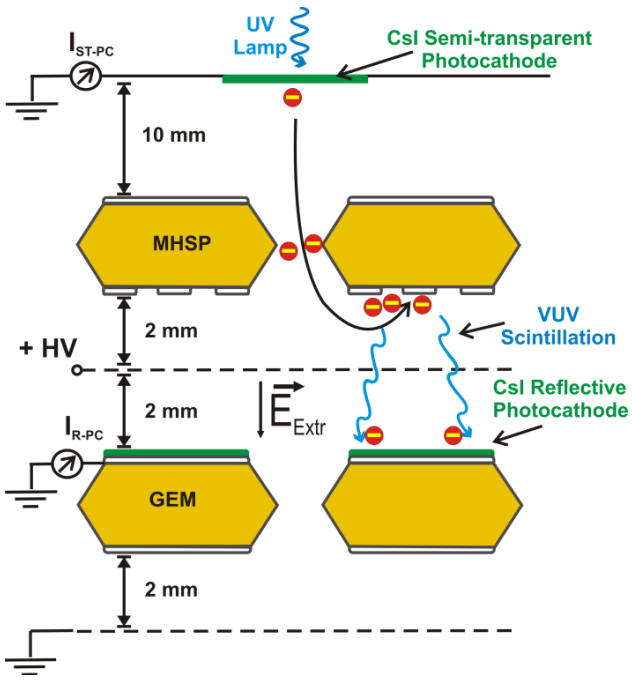

Figure 5.6 - PACEM detector used for the IBF measurements in current mode.

In addition to this change, the MHSP2 of figure 5.2 was replaced by a GEM and a new reflective photocathode[a] was evaporated on its top electrode, resulting in the setup depicted in figure 5.6.

For null voltage differences across the MHSP ($V_{A-C} = V_{C-T} = 0$ V) and for a constant electric field in the drift region, the current measured at the semi-transparent photocathode corresponds to the primary electron current emitted by the semi-transparent photocathode, I_{PE}. During the measurements, in which the voltages across $MHSP_1$ are changed, the primary electron current is kept constant (no changes on the drift field or lamp intensity were done during the measurements) but the total current measured at the semi-transparent photocathode, I_{ST-PC}, reflects the contribution of the ion current that reaches the semi-transparent photocathode. Therefore, during the operation of the detector, the current of ions that reaches the reflective photocathode, $I_{ION,}$ can be calculated accordingly to:

$$I_{IONS} = I_{ST-PC} - I_{PE} \tag{5.3}$$

The ion back flow, i.e. the fraction of ions produced in the detector that flows back to the drift region, is calculated from the knowledge of I_{ION} and the current at the anode of the detector, I_A. This current is the product of the primary electron current, I_{PE} and the total gain of the detector, G_{PACEM}:

$$IBF = \frac{I_{ION}}{I_A} = \frac{I_{ION}}{I_{PE} \times G_{PACEM}} \tag{5.4}$$

In order to measure the optical gain of the PACEM detector the current on CsI reflective photocathode, $I_{R-PC,}$ was measured by connecting the top electrode of the GEM (were the CsI reflective photocathode was deposited) to an electrometer. The current on this electrode I_{R-PC}, is the current of photoelectrons emitted from the CsI photocathode, and is used to evaluate the optical gain of the PACEM detector according to:

[a] The replacement of the Mylar window by the quartz window necessary for the operation of the detector in current mode requires the detector to be exposed to atmospheric conditions for a considerable period of time, degrading the Q.E of the reflective photocathode, reason why a new photocathode was used.

$$\text{Optical Gain} = \frac{I_{R-PC}}{I_{PE}} \tag{5.5}$$

A small nuisance was caused by the use of an external UV beam to produce the primary charge in the semi-transparent photocathode. Some of the photons emitted by the UV lamp passed through the detector window and were not absorbed on the CsI layer that constitutes the semi-transparent photocathode. Some of these photons would even cross through the MHSP holes (the MHSP has an optical transparency of ≈ 7%) and through the ion blocking grid, hitting the reflective photocathode placed in the top electrode of the second stage of the PACEM detector. This resulted in the appearance of a current in the reflective photocathode, $I_{R\text{-}PC0}$, even when no voltage difference was applied across the first element of the PACEM. This situation was partially compensated by slightly tilting the UV beam (making 30º from the vertical) and avoiding a direct hit of the residual UV beam into the reflective photocathode. Nevertheless, a remaining current, proportional to the UV beam intensity, was still measured for null voltages applied across the MHSP. The value of this current, $I_{R\text{-}PC0}$ (dependent on the UV lamp intensity and on the extraction field at the surface of the reflective photocathode) was measured simultaneously with the primary electrons current, I_{PE}, always for null voltages across the MHSP, and was later included in equation 5.5 (subtracted to $I_{R\text{-}PC}$) in order to calculate the optical gain of the detector.

5.3.1 Optical gain

The optical gain was calculated from the knowledge of I_{PE} and $I_{R\text{-}PC}$ measured in current mode, as described above. The primary photoelectron current extracted from the semi-transparent photocathode, I_{PE}, was recorded prior to each measurement for a electric field in the region between the top electrode of the MHSP and the semi-transparent photocathode, E_{DRIFT}, of 0.3 $kV \times cm^{-1}$. The UV beam intensity was adjusted in order to obtain values of $I_{PE} \approx 2$ nA. For these values the current on the reflective photocathode caused by the direct hit of the photons emitted by the UV lamp, $I_{R\text{-}PC0}$, was ≈ 0.1 nA, approximately 20 times less that I_{PE}.

In order to assure full photo-electron extraction from the reflective photocathode, the top electrode of the GEM was connected to ground via an electrometer while the ion blocking grid was polarized at 150 V, resulting in an extraction field of 0.75 $kV \times cm^{-1}$.

In this situation, with the sole purpose of measuring the number of photo-electrons extracted from the reflective photocathode and evaluating the optical gain of the PACEM, the collection of photo-electrons would take place at the ion blocking grid. The photoelectron current was measured at the top electrode of the GEM, were the reflective photocathode was deposited, and reflects the emitted photo-electron current. The bottom electrode of the GEM was grounded.

The MHSP was polarized in the normal mode, by increasing the voltage at the holes, $V_{C\text{-}T}$, until the maximum value was reached and then by increasing $V_{A\text{-}C}$. The optical gains of the PACEM detector, measured in current mode, are summarized in the chart of figure 5.7, as a function of the voltages across the MHSP. The left side of the chart corresponds to the optical gain measured while $V_{C\text{-}T}$ was increased, from 270 V to 450 V and for $V_{A\text{-}C}$ values of 0 V (corresponding to the GEM mode operation of the MHSP). The values on the right side of the chart were obtained for the $V_{C\text{-}T}$ voltages indicated while increasing the $V_{A\text{-}C}$ voltage accordingly to the values indicated in the abscissa.

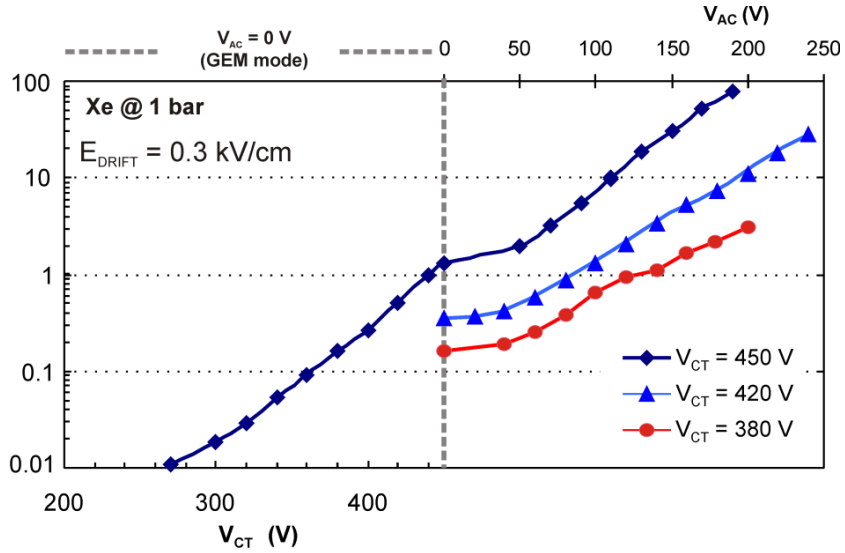

Figure 5.7 - Optical gain of the PACEM detector operated in xenon. $E_{EXTR} = 0.75\ kV \times cm^{-1}$.

The operation of the MHSP for $V_{A\text{-}C} = 0$ V, GEM mode, translates into a maximum optical gain slightly above 1, measured for $V_{C\text{-}T} = 450$ V. The polarization of the region between the strips of the MHSP, by increasing $V_{A\text{-}C}$, corresponded to an increase in the

optical gain by almost 2 orders of magnitude, from 1 to the maximum value of 80, obtained for V_{C-T} = 450 V and V_{A-C} = 190 V.

The maximum optical gains measured in current mode are similar to the ones obtained operating the detector in pulse counting mode, figure 5.3 a) and b), reaching maximum values close to 100.

5.3.2 IBF

The setup described in the previous section was used to evaluate the amount of ions reaching the drift region of the detector. The IBF in cascaded gaseous electron multipliers is strongly dependent on the value of the drift field, following an almost linear increase with the intensity of the drift field. For the IBF measurements with the PACEM we've operated the detector at 2 different values of E_{DRIFT}, 0.1 $kV \times cm^{-1}$ and 0.5 $kV \times cm^{-1}$, corresponding to the typical operation conditions of TPC and GPM detectors, respectively.

The number of ions reaching the semi-transparent photocathode per primary electron extracted is presented in the charts of figure 5.8 as a function of the optical gain of the PACEM detector. The optical gain in the charts was changed by increasing the voltage across the strips of the MHSP, V_{A-C}, from 0 to its maximum value (corresponding to the onset prior to discharges). For low values of the optical gain, corresponding to low values of V_{A-C}, the number of ions per primary electron is, as expected, dependent on the voltage across the holes of the MHSP since most of the ions of the ions that reach the semi-transparent photocathode are produced in this region. With the increase in V_{A-C} additional ions are produced and the dependence of the total number of ions flowing to the drift region on the hole voltage becomes less relevant, as more ions are produced in the anode-cathode strip region, due to the increase in V_{A-C}. For high values of V_{A-C} the curves in figure 5.8 tend to the same value, almost independent of the V_{C-T}.

The comparison on the IBF values obtained for E_{DRFIT} = 0.1 $kV \times cm^{-1}$ and 0.5 $kV \times cm^{-1}$ reveals the dependence on the IBF on the drift field, increasing almost linearly with the drift field: higher values of the field in the drift region favor the extraction of the ions from the holes of the MHSP into the drift region, reducing the amount of ions trapped in the MHSP top electrode.

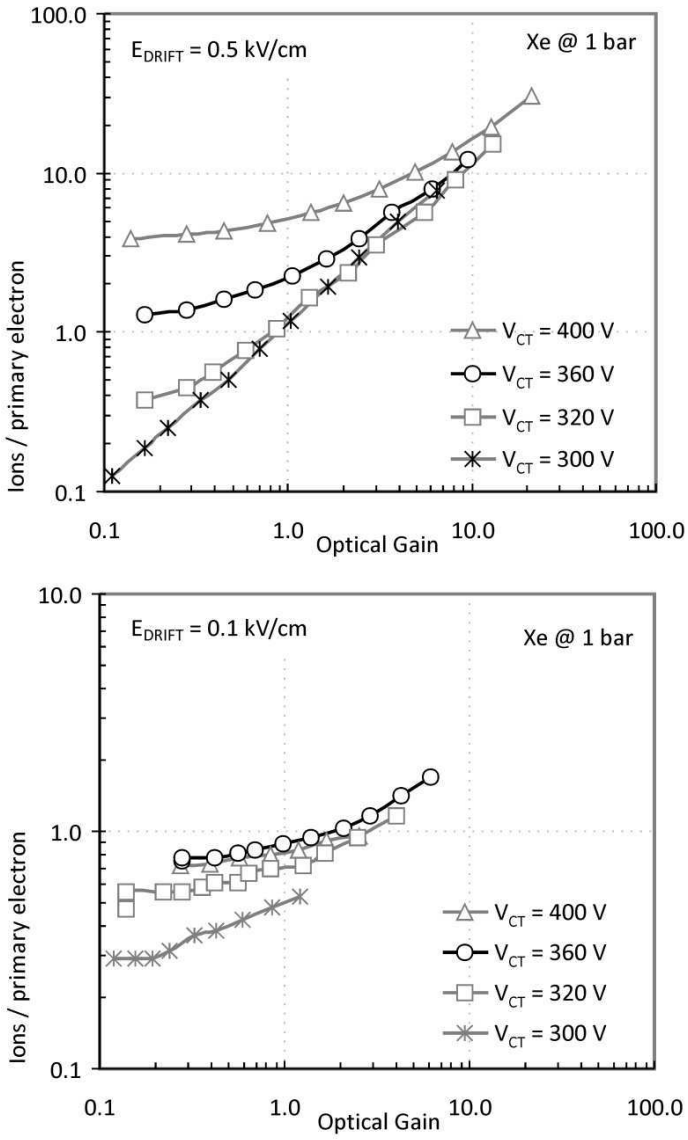

Figure 5.8 - Fraction of ions reaching the drift region of the detector as a function of the optical gain.

The slight reduction in the maximum optical gain obtained in the measurements presented at 0.1 $kV \times cm^{-1}$ versus the ones obtained at 0.5 $kV \times cm^{-1}$ does not translates any physical dependence of the optical gain on E_{DRIFT} being only the consequence of some limitations in the maximum voltages applied to the MHSP during the measurements at 0.1 $kV \times cm^{-1}$.

At $E_{DRIFT} = 0.1\ kV \times cm^{-1}$ we've measured a maximum of 1.5 ions per primary electron reaching the drift region, at an optical gain of 6.5. For $E_{DRIFT} = 0.5\ kV \times cm^{-1}$, 10 ions per primary electron were measured reaching the drift region at an optical gain of 10. These values can be used in equation 5.4 to calculate the IBF achievable in the current conditions,

$$IBF = \frac{I_{ION}}{I_A} = \frac{I_{ION}}{I_{PE} \times Gain} = \frac{I_{ION}}{I_{PE}} \times \frac{1}{Gain} \qquad (5.6)$$

The numbers above indicate that it is possible to achieve IBF close to 10^{-4} for $E_{DRIFT} = 0.1\ kV \times cm^{-1}$ and 10^{-5} at $E_{DRIFT} = 0.5\ kV \times cm^{-1}$, operating the PACEM at total gains of 10^4 and 10^6, respectively.

5.3.3 Total gain and IBF

With the purpose of demonstrating that the ions produced in the second stage of the PACEM do not contribute to the IBF of the detector we've polarized the bottom electrode of the GEM (figure 5.9) and measured the current on the semi-transparent photocathode of the detector, $I_{ST\text{-}PC}$, as a function of the voltage across the GEM holes.

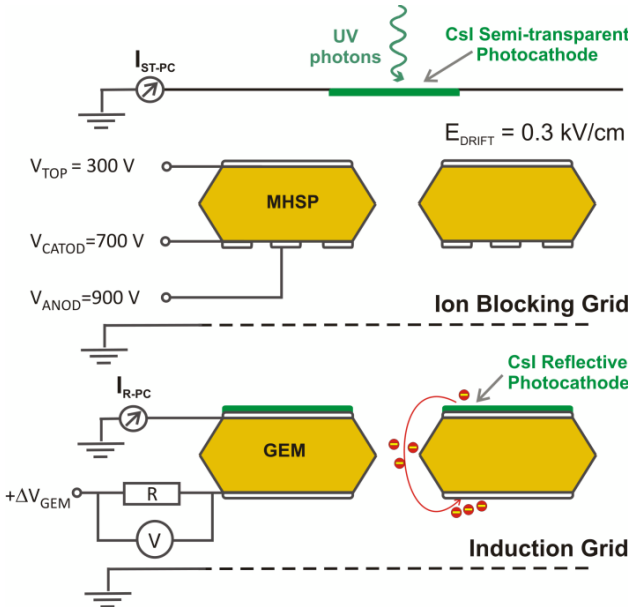

Figure 5.9 - Schematics of the detector used to evaluate the total gain of the PACEM detector and the ion current reaching the drift region.

The total gain of the detector, presented in figure 5.10, is the ratio between the current collected on the bottom electrode of the GEM and the primary photoelectron current extracted from the semi-transparent photocathode (measured for null voltages across the detector). The current on the bottom electrode of the GEM was measured by recording the voltage drop across a resistor connected in series with the power supply.

The current on the semi-transparent photocathode, $I_{ST\text{-}PC}$, was recorded with an electrometer and is also presented on the chart of figure 5.10, as a function of the voltage difference across the GEM, ΔV_{GEM}. This current, equation 5.3, is the sum of the primary photoelectron current (that is kept constant during this measurement) and of the ions back flowing to semitransparent photocathode. In our measurements the voltages at the MHSP were kept constant at the values indicated in figure 5.9 and only the voltage across the GEM holes was changed.

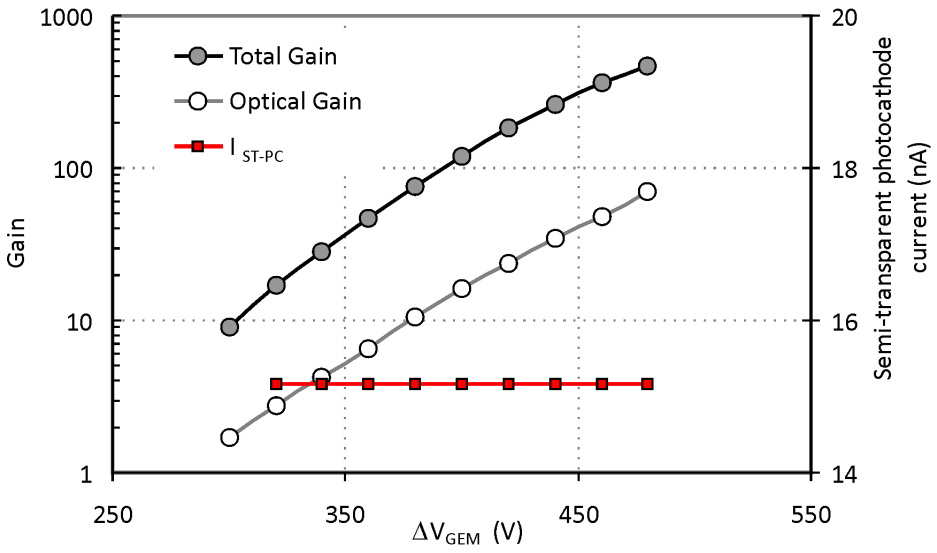

Figure 5.10 - Total gain (solid circles) and optical gain (open circles) of the detector depicted in figure 5.9. The current reaching the semi-transparent photocathode (solid squares, right axis of the chart) is constant during the measurements.

The current on the reflective photocathode deposited on the top electrode of the GEM was also recorded and allowed the calculation of the number of photoelectrons extracted from this photocathode by action of the dipolar electric field established between the top and bottom electrodes of the GEM. The optical gain was then calculated according to

equation 5.5 and is also presented in the chart of figure 5.10 as a function of the potential across the GEM holes.

As it is shown in figure 5.10, the quantity of ions reaching the semi-transparent photocathode (obtained from the current on this photocathode, $I_{ST\text{-}PC}$, right axis) doesn't increase with the increase of the voltage across the GEM holes, being constant and independent on the total gain of the detector.

The experiment and the results presented above clearly indicate that the total gain and the IBF of the PACEM detector are independent quantities; the total gain of the PACEM can be increased with the inclusion of additional multiplicative elements after the ion blocking grid, without any increase in the number of ions reaching the drift region of the detector. The IBF remains constant and only receives the contribution from the ions produced in the first stage of the detector.

5.4 Operation in CF_4

Despite being a molecular gas, that are typically used as quenching gas, absorbing the VUV photons emitted by noble gases, CF_4 is know to be a good photon emitter, being transparent to its own scintillation [91] and with a emission spectra covering the region from the UV to the visible. CF_4 is known to emit primary scintillation, measured during bombardment by ionizing radiation [92] [93] and is also an efficient secondary scintillation emitter under electron impact [94].

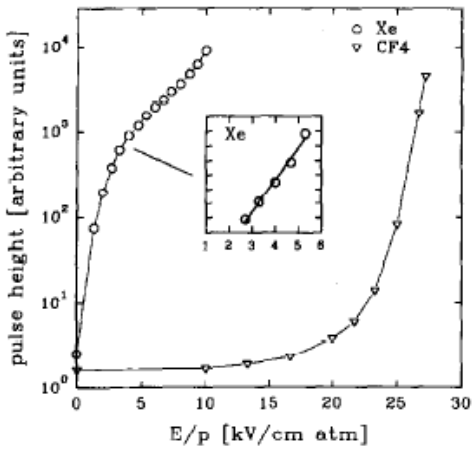

Figure 5.11 - Secondary scintillation in xenon and CF_4 has a function of the applied electric field [92].

The secondary scintillation output during the electron avalanches in CF_4 is lower than in xenon [94] [95] and, according to the authors of [92], the emission takes place only for higher values of electric field, when the mechanisms of charge multiplication start to manifest (figure 5.11). In CF_4 the scintillation is emitted by the positive ions, CF_4^+ and CF_3^+, produced by ionization mechanisms and therefore no scintillation is emitted for values of electric field under the threshold for ionization, [92] [96]. Nevertheless, the emission of CF_4 can, for high values of electric field, reach values as high as the ones obtained in xenon, as it is reported in [92], presenting a significant component in the VUV region with the first and second continua centred at 160 nm and 300 nm, respectively [92][97][98].

On the other hand, the collection efficiency of photoelectrons emitted by solid photocathodes is a few times higher in CF_4 than in xenon [65][66]. This effect is mainly due to the existence of vibrational excitation states in CF_4 that, at low electron impact energies, can compete efficiently with elastic scattering mechanisms. As a result of the presence of this additional mechanism in CF_4 the photoelectron energy may be reduced, after just a few collisions, to values that decrease the probability of returning to the photocathode [64]. This effect could compensate the lower scintillation output and result in a good performance of the PACEM detector operating in CF_4.

5.4.1 Experimental setup

The same setup used in section 5.3 for the measurements of the PACEM optical gain in current mode and depicted in figure 5.6 was used during the measurements in CF_4. The detector was filled at 1 bar and operated in sealed mode using the same circuit for purification as used the one used in the previous measurements, with a small reduction in the operation temperature of the getters, from the typical value of 200º to 150ºC.

The measurements were all done in current mode using an Hg(Ar) VUV lamp as a source of UV photons to promote the extraction of the primary photo-electron current, I_{PE}, from the semi-transparent photocathode.

The photoelectron current emitted from the reflective photocathode, $I_{R\text{-}PC}$ (figure 5.6), was measured for an extraction field of 1.0 $kV \times cm^{-1}$ in the region between the wire mesh and the reflective photocathode, a value that was found to ensure good extraction

efficiency from the CsI photocathodes and, as we'll see in the next section, a stable condition of operation.

5.4.2 Extraction from the CsI photocathode

As described in the previous section, a residual photon flux directly emitted by the UV lamp hits the reflective photocathode deposited on the second element of the PACEM detector and induces a current in this photocathode, $I_{R\text{-}PC0}$, even in the absence of polarization and scintillation in the MHSP. This current was used to measure the extraction curve of the reflective CsI photocathode in CF_4 to values of extraction field up to 1.5 $V \times cm^{-1} \times torr^{-1}$. The results, presented in figure 5.12, indicate that the photoelectron current extracted from the reflective photocathode stabilizes above 1 $V \times cm^{-1} \times torr^{-1}$, in agreement with the results of [65] that report no occurrence of secondary scintillation in CF_4 up to electric fields as high as of 15 $kV \times cm^{-1} \times atm^{-1}$.

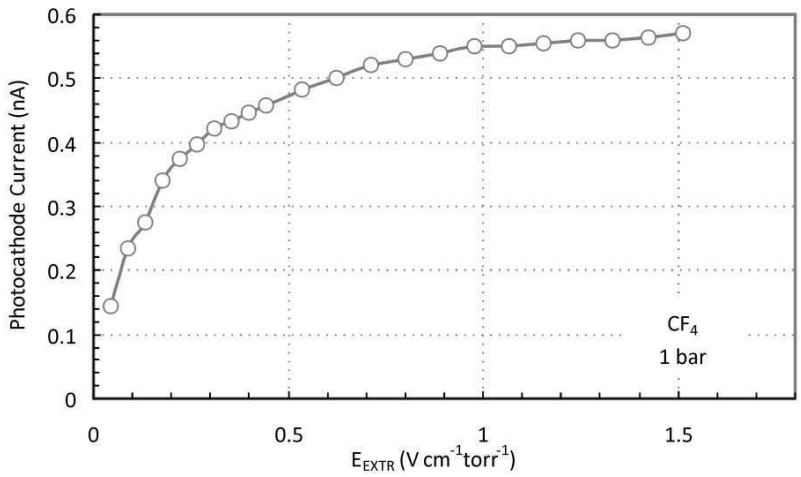

Figure 5.12 - Photo-electron current extracted from the reflective photocathode in CF_4 as a function of the extraction field.

5.4.3 Optical gain

The photoelectron current extracted from the CsI reflective photocathode, $I_{R\text{-}PC}$, was recorded as a function of the voltages at the electrodes of the MHSP for different drift fields in the detector. The optical gain of the PACEM detector operating in CF_4 was calculated, accordingly to equation 5.5, as the ratio between $I_{R\text{-}PC}$ (subtracted from its

value for null voltages across the MHSP to discard the photocurrent induced by the Hg(Ar) lamp) and the primary electron current, I_{PE}, extracted from the semi-transparent photocathode into the drift region of the detector and also measured for null voltages across the MHSP.

The results obtained are presented on the charts of figures 5.13 and 5.14, showing an increase by as much 3 orders of magnitude in the optical gain when increasing V_{A-C} from 100 to 500 V. The results were obtained for different values of V_{C-T}, from 400 to 500 V and for different values of electric field in the drift region of the detector (from 0.1 to 0.5 kV×cm^{-1}). The operational voltages in CF_4 are higher that the ones in xenon, a fact that was already expected from previous works with gaseous multipliers operating in CF_4 [99] [100].

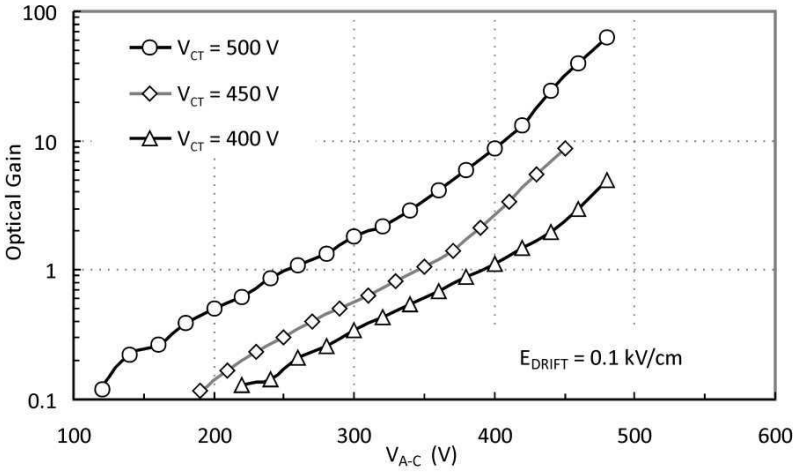

Figure 5.13 - Optical gain of the PACEM detector operating in CF_4 at 1 bar, as a function of V_{A-C}.

The optical gains measured in CF_4 were, for the same operating voltages, approximately one order of magnitude lower that the ones obtained in xenon (figure 5.7) but the higher voltages achieved in CF_4 compensated for this decrease and allowed achieving similar values of maximum optical gains as the ones obtained in xenon. For low values of V_{A-C}, the optical gains obtained were below 1, indicating that, similarly to the situation in xenon, only the extra scintillation mechanisms that take place in the region between the

strips of the MHSP can provide the necessary scintillation output for the efficient operation of the PACEM detector.

For high values of V_{A-C} the behavior of the optical gain curves (figure 5.13) seems to deviate from the exponential increase with V_{A-C}. The same behavior was not recorded in xenon, were the optical gain follows an exponential trend for all values of V_{A-C} measured, until the limit voltage imposed by the onset of discharges. The voltages applied to the MHSP in CF_4, particularly in the region between the strips, are larger by a factor of 2 that the ones applied in xenon, with a proportional increase in the electric field. A plausible explanation to this deviation is the operation of the PACEM detector in CF_4 in a region of electric field where the scintillation output increases faster than exponential, due to the emission of additional scintillation by the molecular ions (figure 5.11) in the electron path from the holes to the anode strips.

Another possible explanation is the occurrence of photon feedback mechanisms, caused by the photoelectrons extracted from the reflective CsI photocathode. This however is not probable: despite the higher extraction efficiency in CF_4 that in xenon, the secondary scintillation in CF_4 only occurs at values of electric field much higher that the ones used in the extraction region in these measurements ($\approx$1 k V $\times$ cm^{-1} $\times$ bar^{-1}).

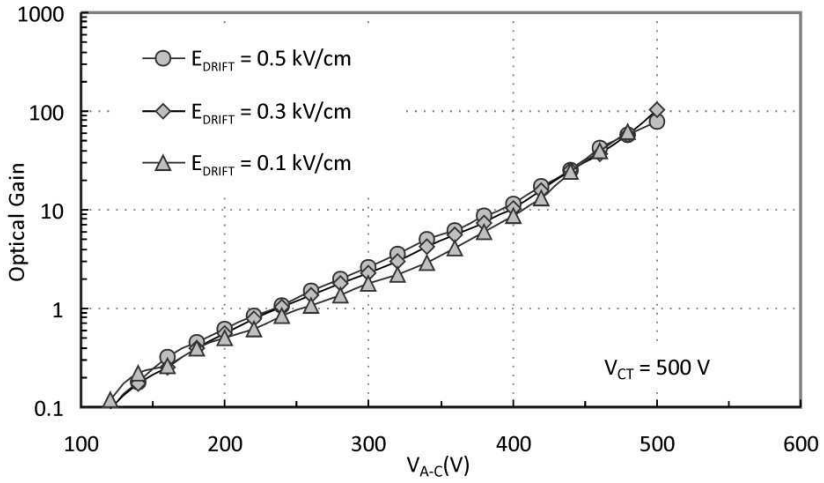

Figure 5.14 - Optical gain of the PACEM detector in CF_4, for different electric fields in the drift region and V_{C-T} = 500 V.

As expected, there is no influence of the electric field in the drift region on the optical gain of the PACEM (figure 5.14). The drift field is however, as previously mentioned, an important factor affecting the ion back flow reaching the drift region. The IBF is considered to increases almost linearly with the drift field, a dependence that is expressed for CF_4 in the chart of figure 5.15 were the number of ions per primary electron as a function of the optical gain, for several values of E_{DRIFT}, is presented.

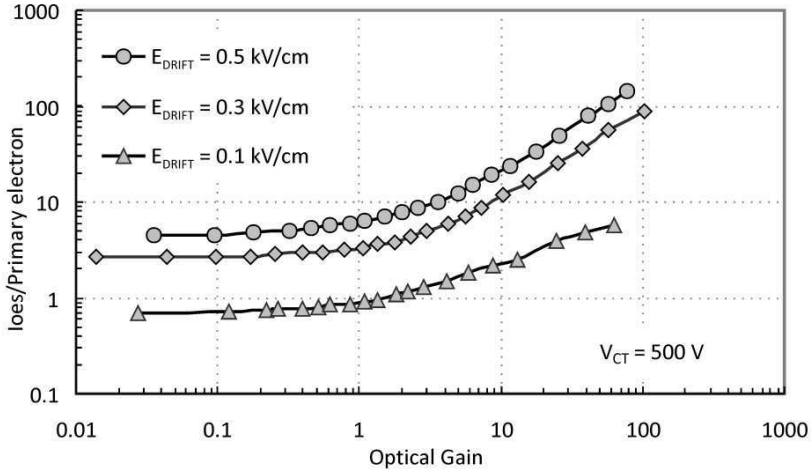

Figure 5.15 - Number of ions per primary electron reaching the drift region of the detector as a function of the optical gain in CF_4. The optical gain was changed by increasing V_{A-C} for a constant V_{C-T} of 500 V.

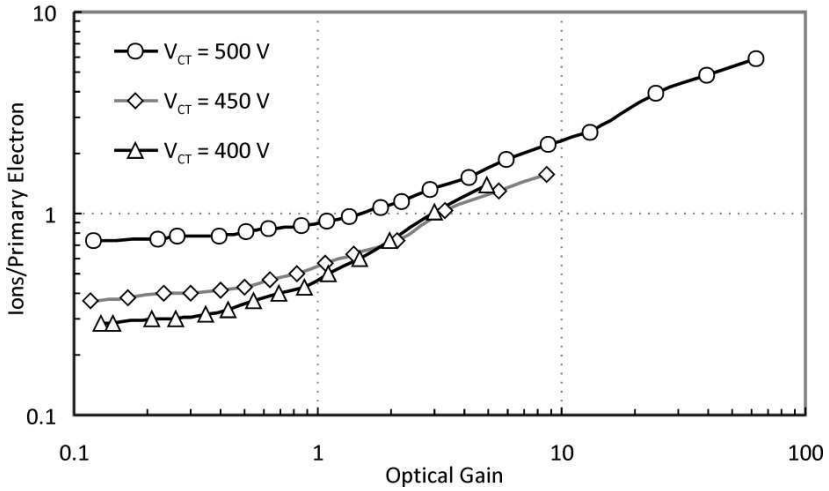

Figure 5.16 - IBF to the drift region as a function of the optical gain in the PACEM detector. The optical gain was varied by increasing V_{A-C}. E_{DRIFT} = 0.1 kV×cm^{-1}.

The number of ions per primary electron reaching the drift region of the detector is presented in figure 5.16, as a function of the optical gain and for different values of V_{C-T}. For low values of V_{A-C}, that correspond to low values of optical gain, the number of ions per primary electron is strongly dependent on the voltage at the holes of the MHSP, V_{C-T}, but at high values of the optical gain this dependence seems to smear as the curves converge in a similar trend. This effect is, as it was in xenon, a consequence of the additional charge multiplication mechanisms that take place in the region between the strips of the MHSP at higher values of V_{A-C}. For low values of V_{A-C}, corresponding to the low optical gain region on the chart of figure 5.16, most of the ions that reach the drift region are produced at the holes of the MHSP and the hole voltage, V_{C-T}, has a major impact on the IBF. For higher values of V_{A-C} the contribution of the ions produced in the region between the strips supersedes the one of the ions produced at the holes and the IBF becomes almost independent on V_{C-T}.

5.4.4 Expected total IBF and conclusions

The results obtained relative to the number of ions per primary electron and optical gain of the PACEM detector operating in CF_4 can be used in equation 5.6, allowing us to do some considerations regarding the expected values of IBF, dependent on the charge gain of the second stage of the PACEM. The number of ions per primary electron was investigated as a function of the optical gain for electric fields in the drift region of 0.5 and 0.1 $kV \times cm^{-1}$, corresponding to typical operations of GPM and TPC, respectively.

For GPM operating conditions ($E_{DRIFT} = 0.5$ $kV \times cm^{-1}$) a total of 24 ions per primary electron was measured reaching the photocathode placed in the limit of the drift region for an optical gain of 12. The operation of the PACEM with a triple - GEM coupled to a reflective photocathode [65] [101] as the second stage of the cascade multiplier may achieve a total gain of 10^6 corresponding to an IBF value of 2.4×10^{-5}.

Similar considerations can be extended for TPC operating conditions ($E_{DRIFT} = 0.1$ $kV \times cm^{-1}$). For this value of drift field we've measured 2.5 ions per primary electron reaching the semi-transparent photocathode at an optical gain of 13. This value results in an IBF of 2.5×10^{-4} for total gains on the detector of 10^4.

Both these figures are very close to the goal established for the operation conditions of these devices. Comparing to the PACEM operation in xenon, the operation in CF_4 leads

to the similar levels of ion blocking capability. The optical gain of the PACEM detector in CF_4 reaches values as high as the ones measured in xenon, indicating that the higher extraction efficiency from the reflective photocathode compensates for the lower scintillation output achieved in CF_4.

5.5 High pressure operation

The operation of gaseous detectors at pressures above the atmospheric has the benefit of increasing the detection efficiency and stopping power of the detector due to the increase in the number of atoms per unit volume. This comes at the cost of (besides the technical difficulties inherent in dealing with high pressure condition) an overall lower charge gain on the detector. The reduction in the maximum gain obtainable with increasing pressure is typical of gaseous detectors [46] [102] [103] being caused by the diminution in the *reduced electric field*, E/p, with increasing pressure. This effect occurs inevitably in these detectors as it is not possible to increase the voltage at the electrodes of the detector linearly with pressure, mostly due to the appearance of leak currents and discharges in the detector.

The increase in the pressure inside the detector causes an increase in the frequency of the collisions that take place between the drifting electrons and the atoms of the gas medium. If the electric field is not properly increased in order to maintain the E/p constant, the kinetic energy acquired by the electrons between each collision will be lower, leaving the accelerated electrons with less energy available to dissipate in the excitation and ionization mechanisms that are responsible for the production of the secondary scintillation.

Another factor that plays a major role in the optical gain of the PACEM is the reduction on the quantum efficiency of solid photocathodes with increasing pressure, due to the backscattering mechanisms with the gas molecules.

On the other hand, the reduction in the charge gain of the detector also affects the charge multiplication and the production of the ions and this effect is expected to bring a positive contribution to the IBF of the detector, leading to a reduction on the number of ions per primary electron that flow back into the drift region of the detector.

The operation of the PACEM at pressure above the atmospheric was investigated with pure xenon at pressures up to 3.3 bar operating the same setup already presented in

figure 5.6. The operation mode of the detector and the equations used in the calculation of the IBF and the optical gain are the same as described in the previous sections.

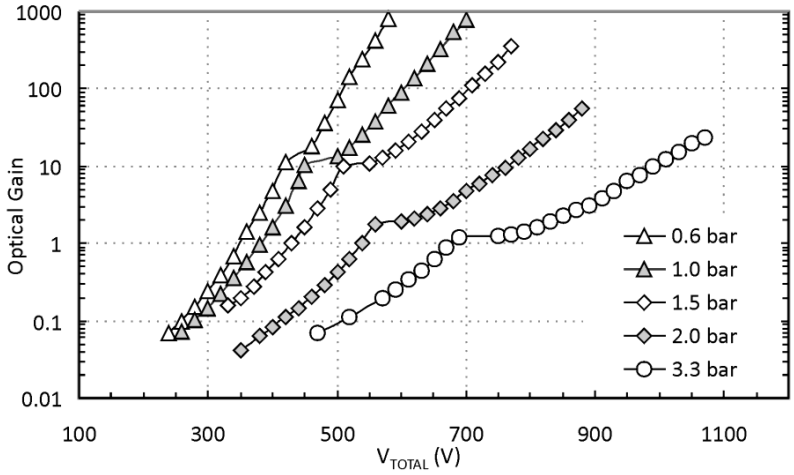

Figure 5.17 - Optical gain of the PACEM detector as function of the V_{TOTAL}, for different pressures. E_{EXTR} = 1.0 kV×cm^{-1}×bar^{-1}.

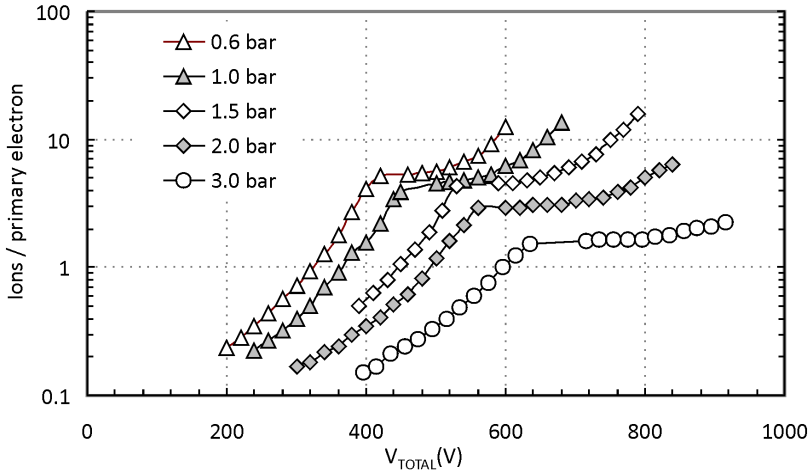

Figure 5.18 - Number of ions per primary electron as a function of the total voltage at the MHSP, for different pressures. E_{DRIFT} = 0.1 kV×cm^{-1}×bar^{-1}.

Figures 5.17 and 5.18 present the optical gain, calculated according to equation 5.5, and the number of ions per primary electron reaching the semi-transparent photocathode, as

a function of the total voltage, V_{TOTAL}, at the electrodes of the MHSP [a]. The results were recorded by first increasing the voltage at the anodes and cathodes of the MHSP while keeping the voltage at the top electrode constant. This resulted in an increase in the total voltage at the MHSP, V_{TOTAL}, due to the increase in V_{C-T} while V_{A-C} was kept at 0 V. Once V_{C-T} reached its maximum value (corresponding to the inflection points on the curves of figures 5.17 and 5.18) the voltage at the cathodes was fixed and the one at the anodes was raised, resulting in an increase in V_{A-C} and consequently on V_{TOTAL}.

For both the optical gain and the number of ions per primary electron, N_{ION}/P_E, the inflection points in the curves of figures 5.17 and 5.18 represent the point where V_{C-T} reaches its maximum value and from where V_{A-C} starts to be increased. After this point the optical gain and N_{ION}/P_E behave differently; while the optical gain increases steadily with increasing V_{TOTAL}, N_{ION}/P_E shows a slower increase with increasing V_{TOTAL}. This different behaviour is more evident at higher pressures and reflects the lower threshold for electroluminescence production relatively to the one for ionization in xenon, which favours the secondary scintillation mechanisms relatively to the charge production.

For low values of V_{A-C} (corresponding to the data points after the inversion in the charts of figures 5.17 and 5.18) the E/p in the region between anode and cathode is not high enough to cause the ionization of the xenon atoms and the curves for N_{ION}/P_E are relatively flat. As the pressure in the detector increases this effect becomes more evident, due to the reduction on the E/p, which is not maintained due to the physical limits to the maximum voltages applied. The number of ions produced and reaching the drift region only approaches an exponential increase for higher values of V_{A-C}, when charge multiplication takes place between anode and cathode. At higher pressures, the threshold of E/p for ionization is reached only for higher values of V_{A-C} and the N_{ION}/P_E curves are relatively flat.

The threshold for the scintillation production is reached for lower values of V_{A-C} and the curves for the optical gain follow an almost exponential increase with V_{TOTAL}, even at higher pressures.

[a] V_{TOTAL} is the sum of V_{A-C} and V_{C-T}.

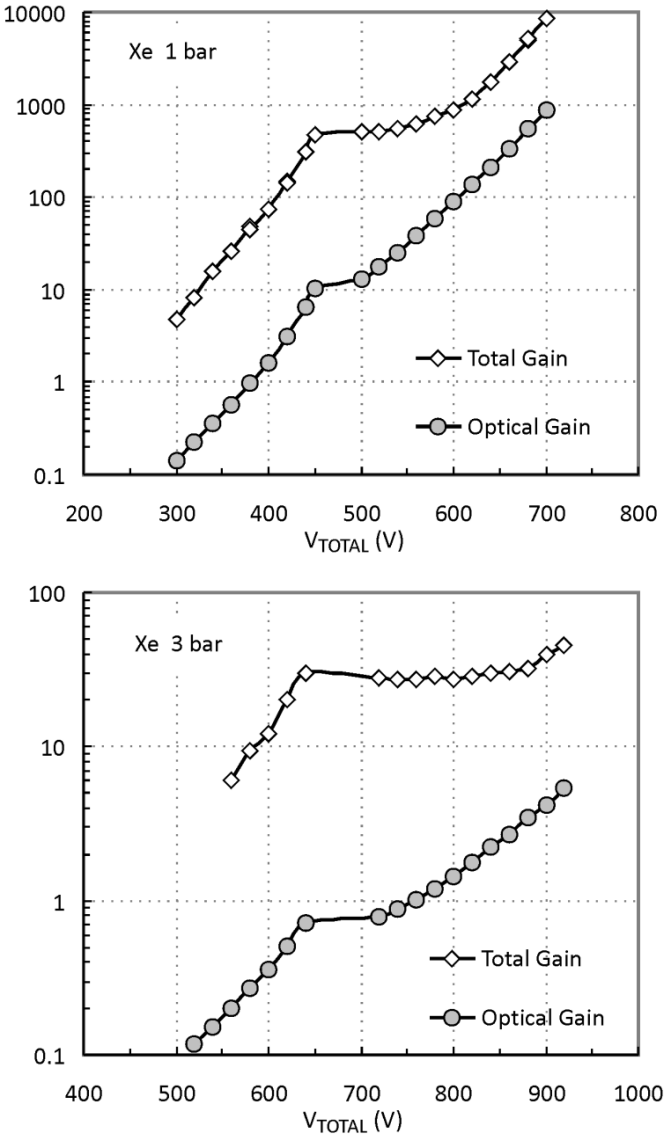

Figure 5.19 - Optical gain and charge gain of the PACEM detector at 1 and 3 bar in xenon. The charge gain was evaluated by adding the currents measured on the anode and cathode electrodes of the MHSP.

The favouring of the scintillation mechanisms over the ionization for low values of V_{A-C} is also visible in the charts of figure 5.19, that compare the total charge gain on the MHSP (evaluated by adding the currents measured at the anodes and cathodes) with the optical gain of the PACEM detector at 1 and 3 bar. At 3 bar, figure 5.19 b), the charge gain increases exponentially with V_{C-T} while this potential is raised but settles in a

plateau once V_{C-T} reaches its maximum value and V_{A-C} starts being increased (inflection point in the curves). The charge gain only increases exponentially again for high values of V_{A-C}. Contrarily to this behaviour, the optical gain presents an almost entirely exponential dependence on V_{TOTAL}, with only a small deviation from linearity for high values of V_{C-T} and for low values of V_{A-C} (data points around the inflection in the curves).

The maximum optical gain of 900, recorded at 1 bar, represents an increase by almost an order of magnitude relatively to the value previously obtained in the same experimental conditions (figure 5.7). This increase is attributed to technical changes done in the detector between the two set of measurements (evaporation of a new reflective photocathode and the replacement of the purifying getters) and in the use of an MHSP from a different batch for the measurements at high pressure.

The maximum optical gain measured drops quickly with increasing pressure, reaching values of 56 and 25 at 2.0 and 3.3 bar, respectively.

The maximum number of ions per primary electron reaching the drift region dropped from 13.5 at 1 bar to 2.3 at 2.9 bar.

Even considering the values measured for the maximum optical gain at 1 bar ($\approx 10^3$), the IBF (obtained by dividing N_{ION}/P_E by the total gain of the detector) is low, close to 10^{-3} for total cascade gains of 10^4, at 1 bar. This value is obtained assuming that the second stage of the PACEM detector is composed by a gaseous detector with a gain of only 10, a very un-restrictive condition. In fact, the high optical gain achieved allows the operation of the PACEM detector at lower V_{A-C} voltages, corresponding to lower values of N_{ION}/P_E. For instance, the operation of the PACEM detector at 1 bar and at an optical gain of 100 corresponds to a value of N_{ION}/P_E of only 8 (or only about 4 for an optical gain of ≈ 20). Operating the PACEM detector at a total gain of 10^4 (at the expense of using a gain of approximately 100 in the second stage of the PACEM) a total IBF of 8×10^{-4} is achieved, approaching the 10^{-4} value (G^{-1}) estimated as the required for the operation of TPC [73] [79].

At higher pressures the requirements on the charge gain of the second stage of the PACEM detector are more demanding, as a result of the lower optical gains achieved. Nevertheless an optical gain of 15 measured at 3.3 bar enables the operation of the PACEM detector at a total charge gain of 10^4, assuming that the second stage can be

operated at a charge gain of 10^3 (a value achieved in previous work done with the MHSP operating at high pressure [46]). For these values of total gain, an IBF of 2×10^{-4} is obtained dividing the value of ≈ 2 N_{ION}/P_E measured at 2.9 bar[a)] by the expectable total gain of the PACEM detector.

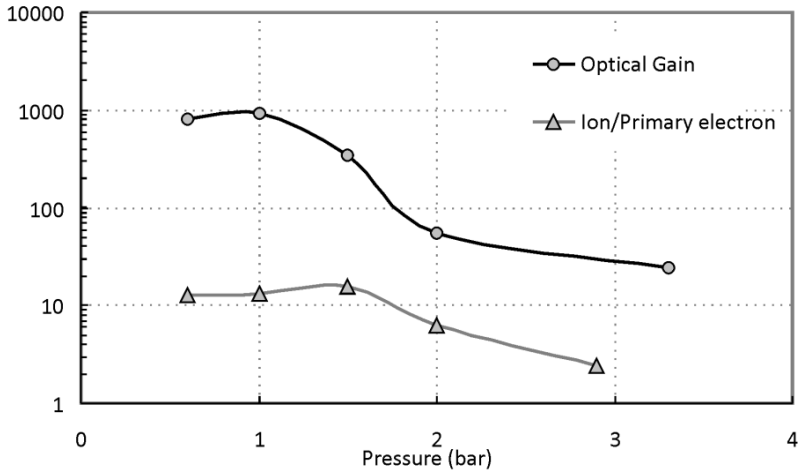

Figure 5.20 - Summary of the optical gain and N_{ION}/P_E, corresponding to the maximum values obtained for each pressure as presented in figures 5.17 and 5.18.

Figure 5.20 summarizes the results obtained for different pressures, presenting the maximum values obtained for the optical gain and N_{ION}/P_E of the PACEM.

5.6 Mixtures Xe-CF_4

As we've seen in the previous sections the performance of the PACEM detector is dependent on the electroluminescence produced in the gas and on the extraction of photoelectrons from the reflective photocathode. The gases studied so far present high scintillation output (xenon) and good photoelectron extraction efficiency from the CsI photocathode (CF_4) and have showed to present similar performance concerning the optical gain achieved.

[a)] The lack of data points for the N_{ION}/P_E at 3.3 bar prevented us to do the direct comparison. Nevertheless the use of the value measured at 2.9 bar is conservative, since N_{ION}/P_E decreases with pressure.

In a recent Monte-Carlo simulation work done by the authors of [64] it was suggested that the inclusion of small quantities of CF_4 (up to 5% of the total mixture) to xenon would increase the photoelectron extraction efficiency by factor of 3. The increase in the photoelectron extraction from the CsI photocathode caused by the inclusion of CF_4 in the gas mixture combined with the high scintillation output in xenon could lead to an increase in the optical gain of the PACEM detector.

5.6.1 Results

The PACEM detector was operated at a total pressure of 1 bar, with binary gas mixtures containing xenon as the primary component and with the inclusion of small quantities of CF_4 corresponding to 1.25, 2.5 and 5% of the total gas volume.

The gas mixtures were prepared from high purity gases (99.999% for CF_4 and 99.99% for xenon). The detector and the circulating system depicted in figure 3.4 (page. 48) were used to prepare the desired mixtures from the pure gases. The volume between valves 6 and 7 (comprising part of the circulating system and the getters container) represents 20% of the volume going from valves 4 to 7 (with valve 5 closed and valve 6 open) and were the detector main body is located. The knowledge of this relation allowed us to prepare the desired mixture by placing the required amount of gas necessary to obtain the final concentrations in each volume.

The detector setup used was the same as described in section 5.3 and the calculation of the IBF and optical gain were done according to equations 5.4 and 5.5, respectively.

The electric field in the drift region and in the extraction region (between the ion blocking grid and the reflective photocathode) of the PACEM detector were, respectively, of 0.1 $kV \times cm^{-1}$ and 1.0 $kV \times cm^{-1}$ for the measurements presented in this section that were done at atmospheric pressure.

The results obtained for the optical gain measured in Xe-CF_4 mixtures are presented on figure 5.21 as a function of the total voltage on the electrodes of the MHSP. As expected [100] the increase in the concentration of CF_4 in the gas mixture allows the increase of V_{TOTAL}. For comparison the values obtained for pure xenon and pure CF_4, obtained on sections 5.5 and 5.4 are also displayed on the chart. The results indicate that, for the same MHSP polarization voltage, the optical gain decreases with the increase in the amount of CF_4 on the mixture, and that higher optical gains are achieved

for pure xenon. Nevertheless, the maximum allowed voltage also increases, leading to similar maximum optical gains when a small quantity of CF_4 is added to xenon.

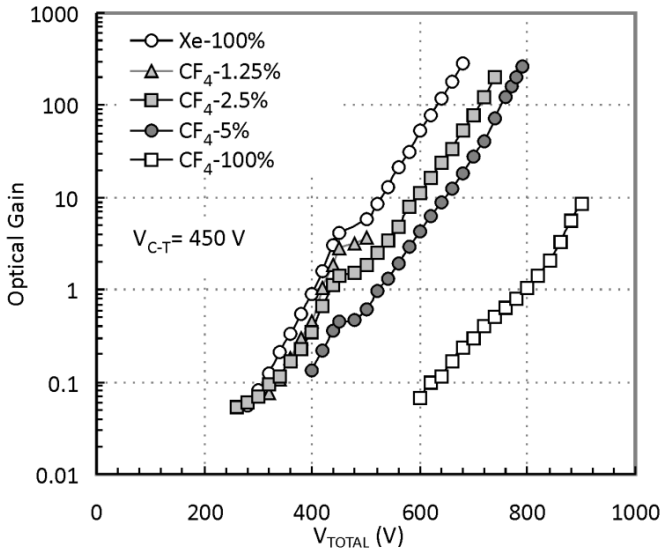

Figure 5.21 - Optical gain as a function of the total voltage on the MHSP for different Xe – CF_4 mixtures. E_{EXTR}=1.0 kV×cm^{-1}

During the measurements presented on figure 5.21 the currents on the anodes and cathodes of the MHSP were also evaluated, allowing the calculation of the total charge gain on this micro-structure. The optical gain of the detector as a function of the total charge gain on the MHSP is represented on figure 5.22. The inclusion of CF_4 in the gas mixture has the effect of, for a given charge gain, increasing the corresponding optical gains relatively to pure xenon.

This is an indication that the photoelectron extraction indeed increases with the addition of CF_4 to xenon, as indicated by the simulation results presented on [64]. The results obtained here show that an optical gain of 10 can be achieved with the mixture Xe - 5% CF_4 for a total charge gain of 100, while, in pure xenon, a charge gain of ≈600 is necessary to achieve the same optical gain. The reduction on the total charge produced on the first stage of the PACEM detector is convenient in order to decrease the ion back flow to the drift region and the use of Xe - CF_4 mixtures can reduce the total charge gain while maintaining the optical gain at a comfortable value, necessary to operate the PACEM with efficiency.

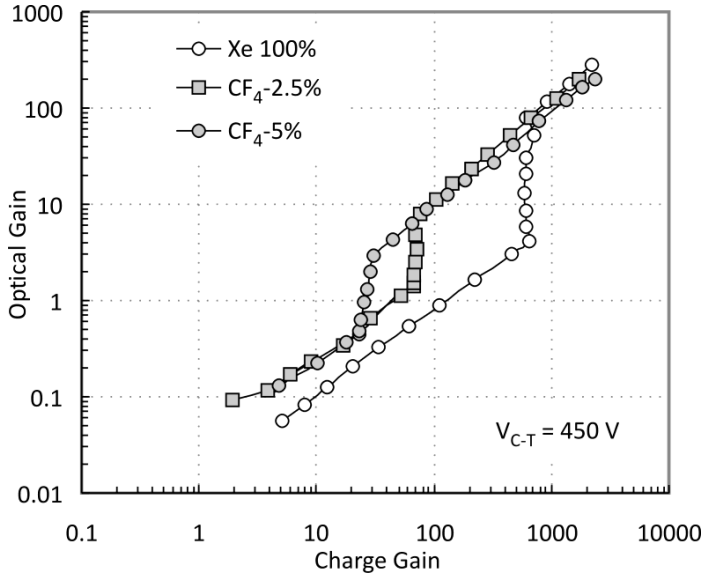

Figure 5.22 - Optical gain obtained as a function of the total charge gain evaluated at the anodes and cathodes of the MHSP. E_{EXTR} = 1.0 kV×cm^{-1}.

The inflection points in the curves of figure 5.22 represent the point were the increase in V_{C-T} stopped and from were V_{A-C} started being increased, as usual done when polarizing the MHSP. The points after the inflection point are obtained for low values of V_{A-C}. For these values, the major effect that occurs in the region between the strips is the transference of the charge from the cathode to the anode, without production of additional charge. Nevertheless during this transference from the cathode to the anode, the drifting electrons acquire enough energy to excite the atoms of the gas medium and produce the secondary scintillation, with the consequent increase on the optical gain of the detector, while the charge gain remains approximately constant.

For high values of V_{A-C}, the curves on figure 5.22 merge in a common trend, denoting a linear relation between the optical gain and the charge gain. In this region the determinant factor for the optical gain is the amount of charge produced and the photoelectron extraction increase achieved with the inclusion of CF_4 to xenon becomes less relevant.

The same effects are present on the curves of figure 5.23 were the number of ions per primary electron, N_{ION}/P_E, is presented as a function of the optical gain of the PACEM detector. The points following the inflection point in the curves are obtained for low values of V_{A-C} for which the charge multiplication on the strips of the MHSP is not very

significant. For these points the increase in the N_{ION}/P_E is very moderate when comparing with the increase in the optical gain.

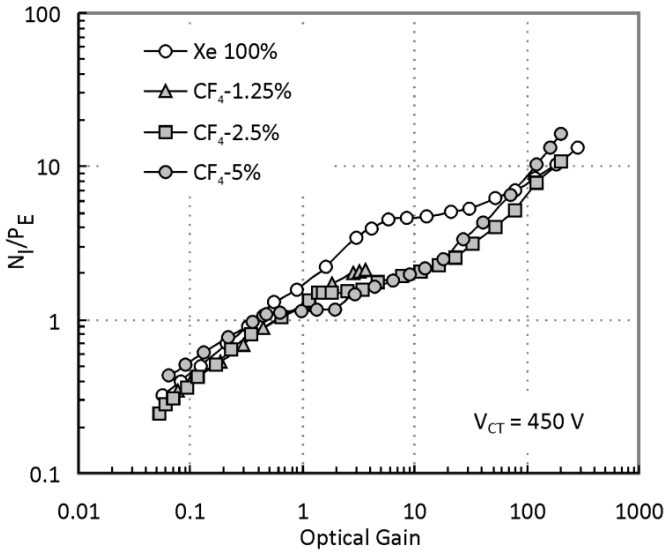

Figure 5.23 - IBF to the drift region of the detector as a function of the optical gain. E_{DRIFT} = 0.1 kV×cm^{-1}.

Figure 5.23 shows that N_{ION}/P_E as low as 2 is obtained for optical gains of 10 for CF_4 concentrations above 2.5%. This can present an advantage relative to the operation of the PACEM in pure xenon.

5.7 Zero ion back-flow detector

The secondary scintillation produced in noble gases, in a uniform field scintillation gap having reduced electric fields close to the gas ionisation threshold, i.e. with negligible charge multiplication, can be used to develop a detector presenting full IBF suppression. In this *Zero IBF Detector* all the charge multiplication is suppressed in the first stage of the detector and the only ions produced in the drift/conversion region are the ones resulting from the production of the primary charges by the ionizing radiation, none resulting from the signal amplification.

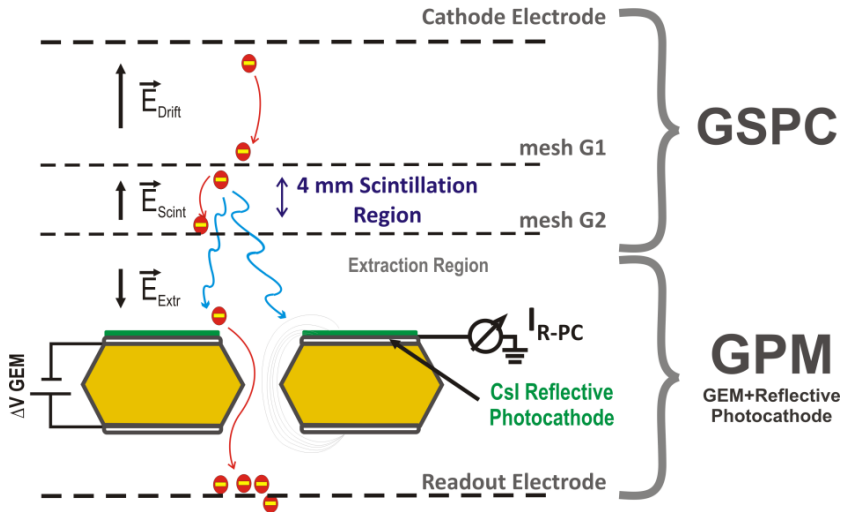

Figure 5.24 - Schematic view of the detector. Mesh G1 and G2 limit the proportional scintillation region, 4 mm deep. The scintillation produced in this region is readout by a Gas Avalanche Photomultiplier (GPM), composed by a GEM coupled to a reflective CsI photocathode.

The *Zero IBF Detector*, figure 5.24, can be pictured as a cascade of a GSPC (section 2.2.3) with a GPM (section 2.4) separated by a grounded metallic mesh, G_2, which acts as blocking grid for the ions produced on the avalanches in the GEM.

The primary electron cloud produced in the drift region of the GSPC will drift through this region under the influence of E_{DRIFT}, defined by the voltage difference between the cathode electrode and mesh G1. The value for the reduced electric field in the drift region is under the gas scintillation threshold.

Once the primary electron cloud transverses the metallic mesh G_1 it enters a region of electric field E_{SCINT} with intensity between the thresholds for secondary scintillation and for ionization in the gas. During the drift in this region the primary electrons will excite (but not ionize) the atoms of the gas medium with consequent production of secondary scintillation, emitted isotropically.

A fraction of this scintillation will promote the extraction of photoelectrons from the CsI reflective photocathode placed on the top surface of the GEM at the second stage of the detector, in a process analogous to the PACEM detector. The photoelectrons extracted will be focused into the holes of the GEM and, by means of an appropriate

extraction field, produce a measurable signal at the readout electrode placed after the GEM.

In the operation of the *Zero IBF Detector* no ions are produced by charge multiplication, an improvement over the PACEM detector and the R-MHSP, where the ions produced in the first stage of the detector also contribute to the IBF.

One of the crucial operational parameters in the *Zero IBF Detector* is its optical gain, defined in the PACEM detector, as the number of photo-electrons extracted from the CsI photocathode for each primary electron produced in the drift/conversion region. In the *Zero IBF detector* the optical gain is dependent on the scintillation yield in the gas (xenon), on the optical transmission of the metallic mesh G_2, on the effective area of the photocathode and on the photoelectron extraction and focusing into the GEM holes.

In order to measure the optical gain, the *Zero IBF Detector* was operated in current mode and only the photoelectron current extracted from the reflective photocathode was measured but, unlike the PACEM detector, a semi-transparent photocathode could not be used as a source of primary electron: the *Zero IBF Detector* is an open geometry detector and the scintillation produced would indubitably cause positive photon feedback, in case a photocathode would be used to directly produce the primary charge in the drift region. Instead a GEM, placed 3 mm above mesh G_1 on figure 5.24, was used as source of "primary electrons" for the *Zero IBF Detector*. This GEM was operated with a semi-transparent photocathode, placed 3 mm above it, to produce the primary charge. The GEM efficiently acted as a screener, optically blocking[a] the semi-transparent photocathode from the scintillation region and therefore preventing the occurrence of photon-feedback.

5.7.1 Optical gain of the zero IBF detector

The results obtained for the optical gain are presented in figure 5.25 for an extraction field of 1.7 $V \times cm^{-1} \times torr^{-1}$ in the region between the reflective photocathode and mesh G_2. The optical gain was calculated as the ratio between the number of photoelectrons

[a] The optical transparency of a typical GEM (140 mm pitch and 50 mm diameter holes in the kapton) is of approximately 12%. Mesh G_1 also contributes, although with higher transparency, to optically block the semi-transparent photocathode from the scintillation region.

extracted from the reflective photocathode and the number of primary electrons. For these measurements the electrodes of the GEM on figure 5.24 were grounded and the current extracted from the reflective photocathode was measured with an electrometer. The metallic mesh G_2 was polarized at negative voltage, setting the electric field intensity in the extraction region, at 1.7 $V \times cm^{-1} \times torr^{-1}$.

The optical gain achieved with the *Zero IBF Detector* (figure 5.25) reveals the linear dependence on the number of photons emitted with the electric field in the scintillation region. Optical gains of 4 were achieved for values of E_{SCINT} of approximately 9 $V \times cm^{-1} \times torr^{-1}$.

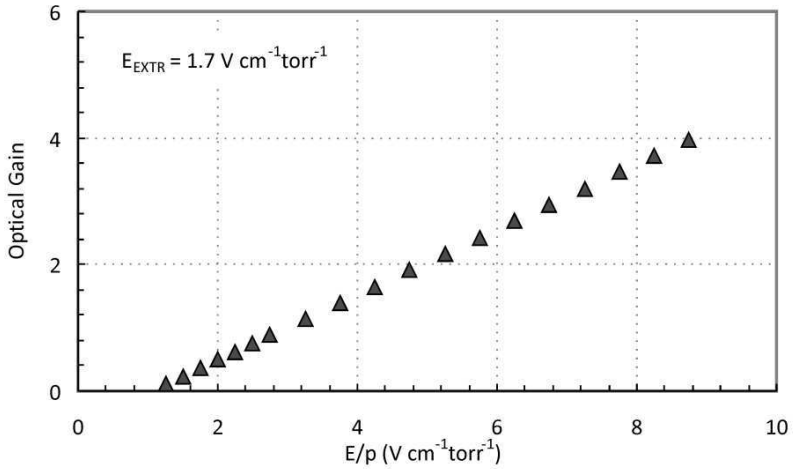

Figure 5.25 - Optical Gain of the Zero IBF Detector, as a function of the electric field in the scintillation region.

The values measured could be used to calculate the scintillation yield (the number of photo-electrons emitted by each primary electron); however the imprecision in this calculation would be dominated by the uncertainties in the determination of the quantum efficiency of the CsI photocathode.

The optical gains presented above are primarily influenced by the quantum efficiency of the CsI photocathode, the dimension of the drift region, the active area of the photocathode and the extraction efficiency from the CsI photocathode. An immediate way of increasing the optical gains presented above would be by enlarging the scintillation region: the electroluminescence emitted by the electrons in the scintillation

region increases linearly with the dimension of this region and this effect would reflect itself on the optical gains achievable. An enlargement of the scintillation gap to 1 cm would increase the optical gains to values close to 10. The increase in the active area of the photocathode (deposited on top of a GEM with 28×28 mm^2) would also translate in an increase in the optical gain, as a result of the larger solid angle coverage.

5.8 Conclusions

The validity of the PACEM concept was initially proven by the operation a detector composed of 2 MHSP in pure xenon. The detector was irradiated with 5.9 keV X-rays and the signal was transmitted to the second MHSP using the electroluminescence produced in the first MHSP. Maximum optical gains of ≈ 60 were achieved and no energy resolution degradation was observed between the signals recorded on both MHSP.

Following the measurements with X-rays we've focused on the measurement of the optical gain and N_{ION}/P_E for different mixtures, as a function of the total voltage applied to the MHSP. The results were promising, having achieved optical gains well above 10 for all the mixtures studied and demonstrating that the total charge gain of the PACEM detector can be increased (by increasing the charge gain of the second stage of the detector) without any increase in the number of ions backflowing to the drift region.

The measurements in xenon showed that approximately 10 ions backflow to the drift region for each primary electron at an optical gain of 10 and at E_{DRIFT} = 0.5 kV×cm^{-1}. This figure drops to ≈3 ions per primary electron at a drift field of 0.1 kV×cm^{-1} for the same optical gain.

The operation in CF_4 revealed that maximal optical gains comparable to the ones measured in xenon are achievable in this gas, reflecting its higher photoelectron extraction efficiency. For a drift field of 0.5 kV×cm^{-1} and an optical gain of 10 we've measured ≈25 ions backflowing to the drift region of the detector for each primary electron and only 2 ions at a drift field of 0.1 kV×cm^{-1} and similar optical gain.

The operation of the PACEM at pressures above the atmospheric pressure has showed that optical gains well above 10 are achievable in xenon for pressures up to 3 bar. The optical gains achieved are combined with a decrease in the number of ions reaching the drift region of the detector with increasing pressure.

The operation in $Xe-CF_4$ mixtures was tested, taking advantage of an increase in the photoelectron extraction with the inclusion of small quantities of CF_4 in xenon. For the same operational voltages on the MHSP, the operation of the PACEM detector with small (up to 5 %) concentrations of CF_4, translates in a reduction of the number of ions backflowing to the drift region relatively to the pure xenon operation. At an optical gain of 10 the N_{ION}/P_E measured in the $Xe-5\%CF_4$ mixture was of ≈ 2, versus a value of ≈ 5 for pure xenon, for the same operational voltages on the detector.

The ion back flow suppression was taken to its maximum with the *zero IBF detector*, that operates as a GSPC, with the secondary scintillation produced by the primary electrons used to promote the extraction of the photoelectrons from a photocathode that are further multiplied via charge avalanche mechanisms. In this detector only the primary ions reach the drift region. The operation of the *zero IBF detector* with a scintillation region of 4 mm and a 28×28 mm^2 photocathode yielded optical gains as high as 4. This value can be increased with larger scintillation region and/or larger photocathode coverage.

6 THICK ELECTRON MULTIPLIERS

6.1 The THCOBRA

The development of the family of thick electron multipliers and the interesting properties of these devices suggested the implementation of an MHSP based in the same technology. A thick-version of the MHSP could potentially combine the excellent operational properties of the MHSP with the simplicity and easiness of production of THGEM. This triggered the experimental tests of a THGEM with one of its faces presenting two independent sets of electrodes (figure 6.1). The winding shape of these electrodes is a distinctive characteristic of the THCOBRA, a thick-electron multiplier that incorporates 3 independent electrodes on its structure.

A first set of THCOBRA was manufactured[a] and the results of the first tests done are presented here. The THCOBRA are made of a G10 plate with an active area of 15×15 mm^2. One of the sides, the *top*, presents a continuous electrode, similar to the electrodes of the THGEM of figure 2.8 with a small rim etched around each hole, while the other side, the *bottom*, is structured in two independent electrodes, as it is showed in figure 6.1. The presence of the small rim around the holes in thick electron multipliers

[a] Print Electronics, Israel (http://www.print-e.co.il).

provides increased stability to these devices and allows for higher charge gains to be achieved [51].

The THCOBRA was, similarly to the THGEM, produced with the holes disposed in a honeycomb pattern and is made out of a 0.4 mm thickness G10 plate. The electrodes that surround the holes are, similarly to the MHSP, designated by cathodes, and are 0.1 mm wide. The cathodes are separated form the holes by the rim, also with 0.1 mm. The other set of electrodes, the anodes, are approximately 0.3 mm wide and are separated from the cathodes by a small region with 0.1 mm of bare G10.

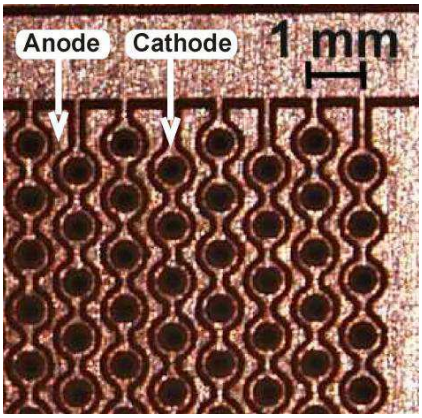

Figure 6.1 - Detailed photo of the bottom side of the THCOBRA. The electrodes in this side of the THCOBRA have circular shape: the cathodes, 0.1 mm wide, are concentric with the holes (0.3 mm diameter). The space between each pair of cathodes is filled with the anode electrode, 0.3 mm wide. A small, 0.1 mm, gap of exposed G10 separates the anodes from cathodes. The rim, 0.1 mm wide, is etched around the holes for increased stability.

The presence of the anodes and cathodes electrodes, in combination with the one on the opposite surface of the THCOBRA allows the creation of two independent charge multiplication regions on the THCOBRA: one of these regions (equivalent to the one in the THGEM), in the region inside the holes, and another in the region between the two electrodes on the bottom side of the THCOBRA. The voltages differences between these three electrodes control the electric field in these two regions and the electron avalanches on the THCOBRA. Similarly to the MHSP, the voltage difference between the cathode and the top electrode ($V_{C\text{-}T} = V_{CATHODE} - V_{TOP}$) controls the multiplication inside the holes of the THCOBRA while the voltage difference between anode and cathodes ($V_{A\text{-}C} = V_{ANODE} - V_{CATHODE}$) controls the multiplication that takes place in the

region between these two electrodes. The total voltage across the THCOBRA is the sum of this two voltage differences: $V_{TOTAL}=V_{A-C}+V_{C-T.}$

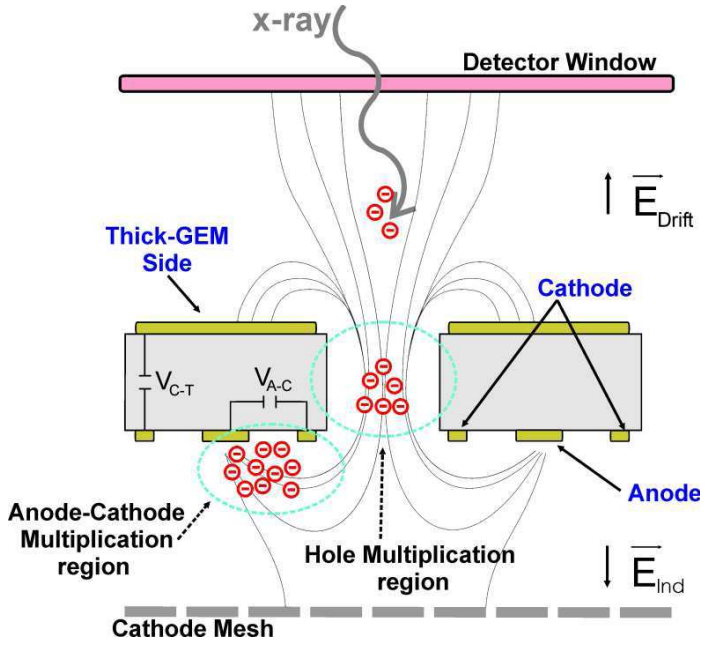

Figure 6.2 - Schematic representation of the THCOBRA operating properties.

The electric field in the drift region, E_{DRIFT}, ensures that the primary electrons deposited in this region by the ionizing radiation are transported to the THCOBRA, were they are focused into its holes by an appropriate combination of low drift field and high field in the holes of the THCOBRA.

The value of the electric field inside the holes of the THCOBRA is controlled by the V_{C-T} voltage and determines the amount of charge multiplication that takes place inside the holes of the THCOBRA. The resulting net charge is extracted from the holes and, due to the potential difference between cathode and anode, V_{A-C}, is further multiplied in the region close to the anodes were the total charge is finally collected.

6.2 Electric field intensity and charge transport simulations

To prove that, as described above, a two-step multiplication can occur within the THCOBRA multiplier (despite the large dimensions of the electrodes on the bottom

surface) we've used the software packages GARFIELD [104] and MAXWELL [105] to perform electric field intensity and charge transport simulations.

For values of V_{A-C} = 300 V the electric field intensity in the region between anodes and cathodes (calculated with the Maxwell software package) reaches values of several tents of kV×cm^{-1}, being particularly intense in the vicinity of the anodes (figure 6.3). An electron extracted from the holes of the THCOBRA drifts through the region between anodes and cathodes under the influence of a large electric field, experiencing additional gas multiplication, until the collection at the anode strips.

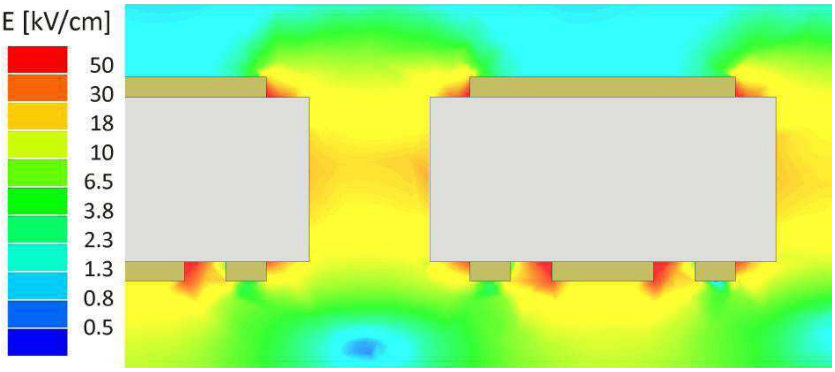

Figure 6.3 - Maxwell [105] electrostatic simulation of the electric field intensity on the THCOBRA. V_{CT} = 1180 V and V_{AC} = 300 V. E_{DRIFT} = 0.1 kV×cm^{-1} E_{IND} = 4 kV×cm^{-1}. In this configuration the electric field intensity in the vicinity of the anodes reaches values above 20 kV×cm^{-1}.

The charge multiplication in the vicinity of the anode strips was also evaluated with the GARFIELD software package: the path of an electron created in the second, strip multiplication region, and collected at the anodes, was simulated for V_{A-C} = 60 V and V_{A-C} = 280 V (figure 6.4). The results, obtained for argon at the pressure of 1 bar, indicate that the increase in V_{A-C} causes additional charge multiplication in the region near the anodes, which does not occur at lower voltages (V_{A-C} = 60 V) to take place in the region near the anode strips.

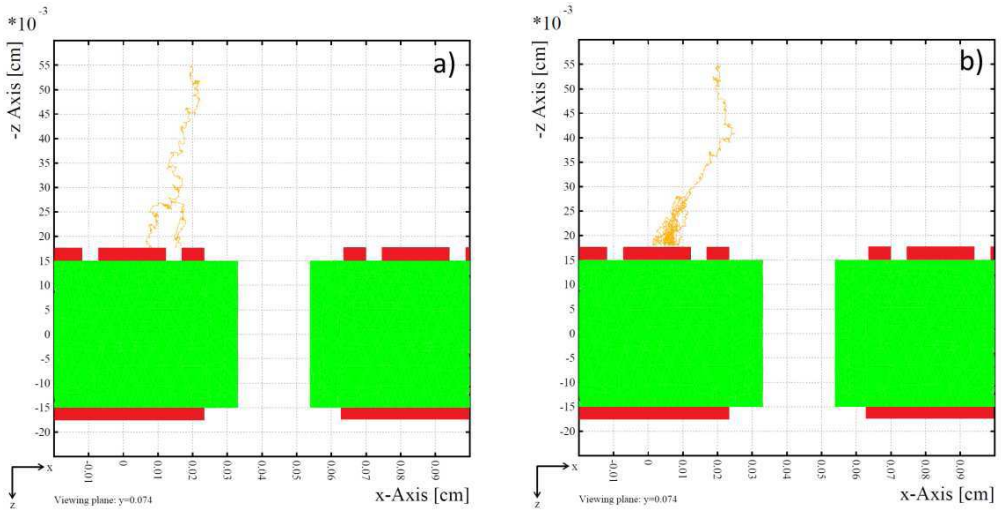

Figure 6.4 - Simulated path and multiplication of an electron created on the strip side of the THCOBRA (and not crossing the holes) for V_{A-C} = 60 V (a) and V_{A-C} = 280 V (b). Additional charge multiplication occurs for higher values of V_{A-C}. Simulations were calculated for V_{C-T} = 180 V, E_{DRIFT} = 0.5 kV×cm^{-1} and E_{IND} = 8.0 kV×cm^{-1}.

6.3 Charge gain measurements

To test the charge multiplication properties of the THCOBRA we've used the detector and the gas admission line already described in the Experimental Methods chapter. Only small modifications were required in order to accommodate the THCOBRA inside the vacuum chamber. All the electrodes of the detector were independently polarized using current limited (100 nA) CAEN N471A power supplies. During the measurements the detector was operated both in pulse (with argon and argon based mixtures) and in current mode (in neon).

The charge gains obtained in argon and P10 (a mixture composed by 90% argon and 10% CH_4) at 1 bar, and in neon, at 1.7 bar, are presented in figure 6.5 as a function of the total voltage (V_{TOTAL}=V_{A-C}+V_{C-T}) applied to the THCOBRA electrodes.

The results in neon were obtained operating the detector in current mode: a semi-transparent photocathode was deposited on a UV transparent window and placed at 10 mm distance from the top electrode of the THCOBRA. The photocathode was irradiated with UV photons and a drift field of 0.1 kV×cm^{-1} was used to promote the extraction of the photo-electrons and their focusing at the holes of the THCOBRA. V_{C-T}

was first raised to 340V while V_{A-C} was kept at 0 V by raising simultaneously the potentials of the anodes and cathodes. Following that, V_{C-T} was kept at 340 V and V_{A-C} was raised up to 140 V; this was achieved by keeping the cathode voltage constant while increasing the anode voltage, resulting in a total voltage across the THCOBRA of 480 V. For values of $V_{A-C} = 0$ V (corresponding to the situation where only V_{C-T} was being increased) the current on the anode was zero and the total gain of the detector was obtained by dividing the cathode current by the primary current, I_{PC0}. The increase on V_{A-C} led to an increase in the anode current and to a rapid decrease of the current measured on the cathode; the latter dropped to zero for $V_{A-C} > 80$ V.

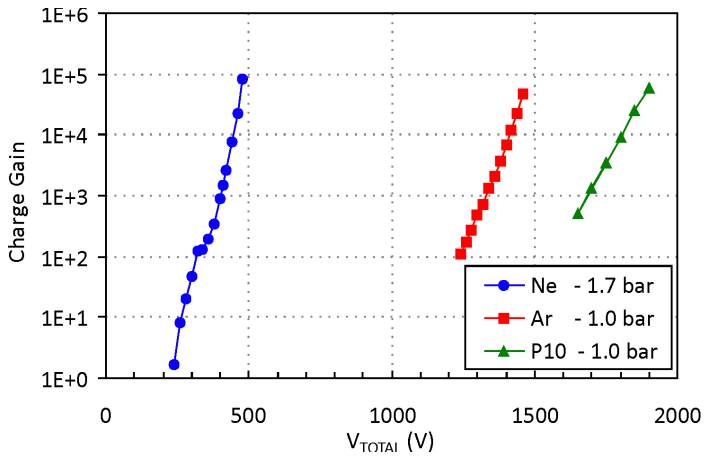

Figure 6.5 - Charge gain obtained in Argon, P10 and Neon, as a function of the total voltage at the THCOBRA.

The results presented for argon and P10 were taken in pulse-counting mode, using X-rays from a ^{109}Cd source to induce the primary charge in the drift region of the detector. The electric field in this region (E_{DRIFT} = 0.1 kV×cm^{-1}) was responsible for the collection and focusing of the primary electrons in the holes of the THCOBRA. The final charge produced by each event was collected at the anodes of the THCOBRA using a Canberra 2006 preamplifier (with the sensitivity set to 1.5 mV/pC) and feed to a Tennelec TC 243 linear amplifier (4 μs shaping time). The output of the amplifier was connected to a Nucleus PCA2 1024 multichannel analyzer. The electronic chain sensitivity was calibrated by injection of a known charge into the preamplifier input.

The voltage across the holes, $V_{C\text{-}T}$, was 1180 V for the measurements in Ar and 1475 V for the ones in P10. The maximum gains obtained in these gases were similar: 5×10^4 in Ar and 6×10^4 in P10, at respective total voltages of 1460 V and 1900 V.

The charge gain measurements presented in figure 6.5 were obtained by collecting the final charge multiplied on the anodes of the THCOBRA. In a standard THGEM the electric field extends itself outside the holes and reaches values above the threshold for charge multiplication in the region beyond the exit of the holes [50][106]. The high charge gains recorded with the THCOBRA could, despite the high values obtained and of the results of the simulations presented above, be a product not of additional charge multiplication mechanisms taking place in the region between anodes and cathodes but simply of a better collection efficiency of the electrons multiplied inside the holes of the THCOBRA.

In order to experimentally establish the occurrence of charge multiplication in the region between the anodes and cathodes of the THCOBRA, the charge gain was independently evaluated in these two electrodes, operating the detector in pulse mode. For this we've simultaneously measured the pulse signals from both anode and cathode electrodes, feeding the charge collected at the cathode of the THCOBRA to another charge sensitive pre-amplifier.

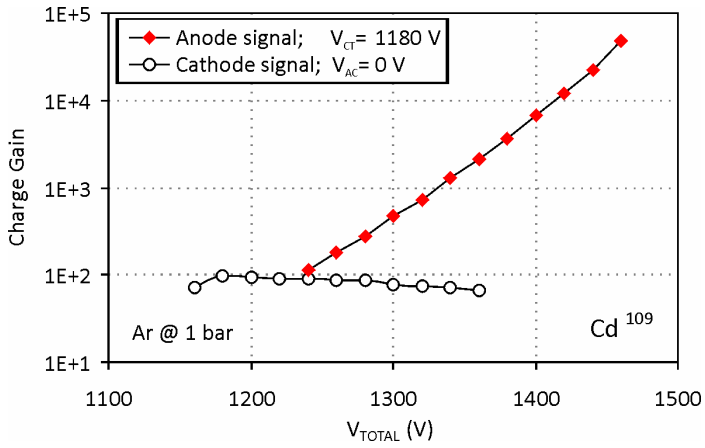

Figure 6.6 - Charge gain measured simultaneously at the anodes and cathodes of the THCOBRA. The first point in the anode-signal curve was obtained for $V_{A\text{-}C}$ = 60 V. Below this value, the signal recorded in the pre-amplifier connected to the anode was within the noise, i.e. absolute gain less than 70.

In the operation of the THCOBRA with $V_{A-C} = 0$ V (figure 6.6) the voltage at the cathode was raised until V_{C-T} reached 1180 V. At this point the charge gain measured at the cathode was of ≈100 and the signal on the anode electrodes was below the detection threshold (≈ 70). The increase in V_{A-C} from 0 V to 280 V lead to a total gain (measured at the anodes of the THCOBRA) of 5×10^4, representing an increase by a factor of 500 relatively to the charge gain measured at the cathode of the THCOBRA for $V_{A-C} = 0$ V. This increase can be partly attributed to an improvement on the charge collection at the anode strips but is mostly caused by the additional charge multiplication (due to the increase in V_{A-C}) that, according to the electric field intensity simulation, takes place along the electron path and in the vicinity of the anodes.

Figure 6.7 presents a typical pulse height distribution obtained with the THCOBRA operating in P10. The distribution features the Ag kα and kβ X-rays, the Cu k-fluorescence lines from the copper electrodes and the respective escape peaks. An energy resolution of 12.2% FWHM was measured for the 22.1 keV energy X-rays and 19.2% for the 8 keV Cu fluorescence line.

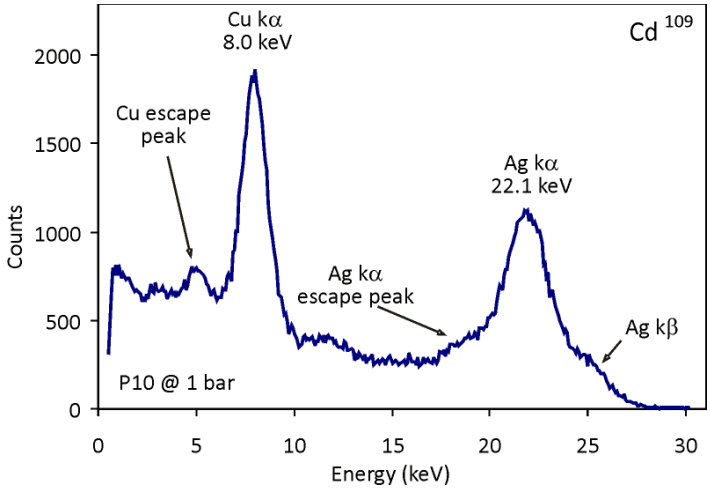

Figure 6.7 - Energy distribution of a Cd^{109} radioactive source. 12.2 % energy resolution was measured for the 22.1 keV kα peak. The energy resolution values were obtained by fitting a Gaussian curve superimposed on a linear background to the region of interest around the peaks. Spectra obtained at charge gain of 10^4.

6.3.1 Charge gain stability

The G10 substrate used in the production of the THCOBRA has a high resistivity and the charges that end up on its surface tend to accumulate and distort the local electric field, affecting the operational properties of the THCOBRA. Other factors, particularly temperature changes in the gas, can also affect the gain stability with time. We've measured the gain of the THCOBRA, as a function of time and found that after an initial decrease, probably caused by the charging up effects of the G10 described above, no further change in the gain was recorded during the period of observation (up to 5 hours). For these measurements the THCOBRA was irradiated with the 22.1 keV X-rays from a Cd^{109} X-ray source, with a collimated beam of approximately 6 mm^2. The counting rate was approximately 25 Hz/mm^2 and the THCOBRA was operated at a total gain of 10^4.

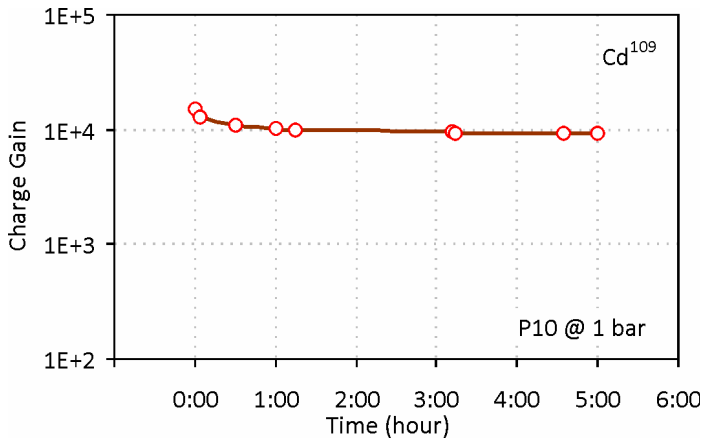

Figure 6.8 - Charge gain as a function of time. After and initial decrease, the charge gain remains stable. The line serves only as a guide to the eyes: data was only taken at the open marks.

6.3.2 Single photoelectron measurements

The charge gains recorded with the THCOBRA could permit, with the use of proper electronics, the detection of single photoelectrons. The response to single photoelectrons was investigated with the THCOBRA coupled to a semitransparent CsI photocathode. The detector was irradiated by a strongly collimated UV beam from the Hg(Ar) UV lamp and operated in pulse-counting mode, with a charge pre-amplifier

connected to the anode and recording the pulses caused by the photoelectrons emitted from the CsI photocathode.

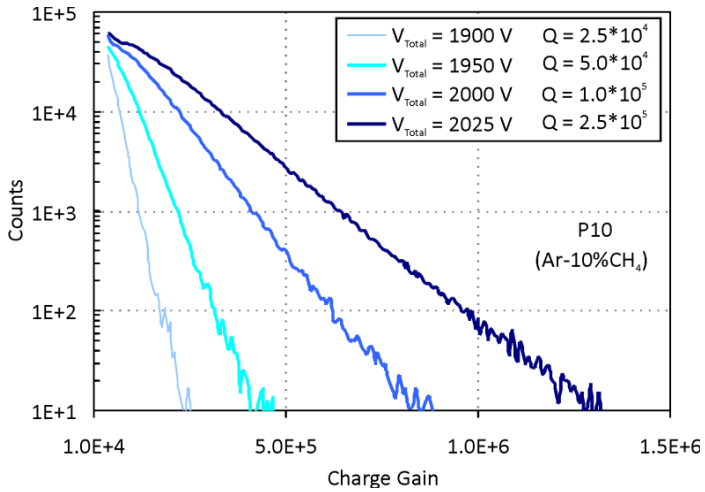

Figure 6.9 - Single photoelectron spectra obtained with the THCOBRA in P10 at 1 bar. The maximum average gain, extracted from the curves obtained was 2.5×10^5.

The single photoelectron pulse-height distributions are presented in figure 6.9 for different V_{TOTAL} values. The average charge gain for each distribution, Q, was obtained by fitting the single photoelectron spectra to a normalized Polya distribution [3] [84],

$$P(q)=\frac{1}{Q}e^{\frac{-q}{Q}} \tag{6.1}$$

were q is the individual gain of each avalanche.

The average charge gains reached in single-photoelectron conditions are, for the same V_{TOTAL}, similar to those obtained with X-rays (figure 6.5) but higher biasing voltages are reached in single-photoelectron conditions. This effect is explained by the higher onset of the Raether limit: the 22.1 keV X-rays emitted from the Cd^{109} source and absorbed in the P10 mixture produce in average approximately 830 primary electrons for each interaction (w values for Argon and CH_4 are 26 and 27.3 eV/ion, table 2-1). For the maximum gain of 10^5 obtained with the Cd^{109} X-ray source (and assuming full detection efficiency) the final charge collected at the THCOBRA is of $\approx 10^8$, a value matching the Raether limit [107] which states that the limit number of electrons-ions pair in an avalanche cannot exceed the 10^7-10^8. When operating the THCOBRA in

single photo-electron conditions, where the primary charge is about 3 orders of magnitude lower that when the Cd^{109} X-ray source is used, the Raether limit appears for higher voltages across the detector and higher maximum charge gains are achieved.

6.4 Application of the Thick-MHSP to the PACEM Detector

Following the operation of the THCOBRA in pure argon we've implemented a PACEM detector operating with a THCOBRA as the first stage of the detector.

The expanded dimensions of the THCOBRA should, in principle, favour the production of secondary scintillation on the THCOBRA, as the path travelled by the electron cloud increases relatively to the MHSP.

To evaluate the scintillation output of the THCOBRA this device was incorporated as the first element of the PACEM detector depicted in figure 6.10:

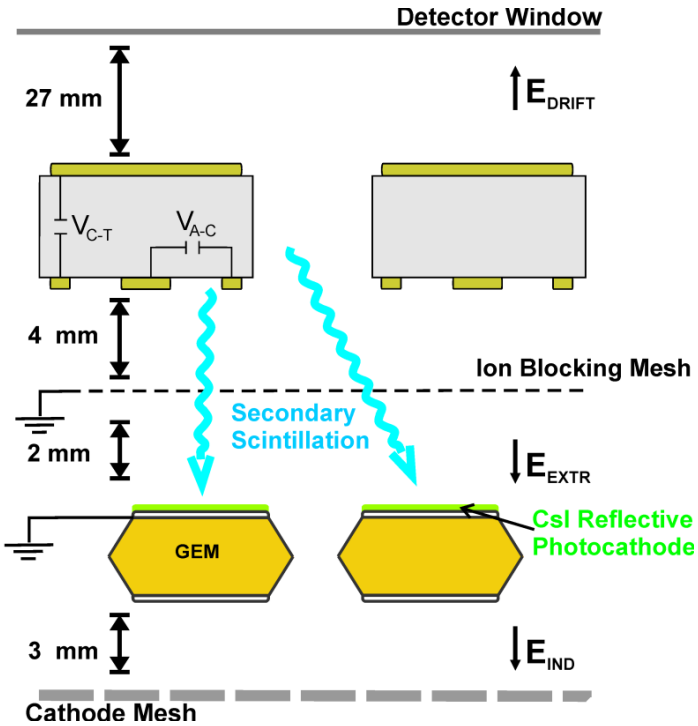

Figure 6.10 - Schematic operation of the PACEM detector used to test the THCOBRA.

A fresh CsI reflective photocathode (2500 Å thick) was vacuum evaporated on the surface of a gold plated GEM with standard dimensions. The detector was vacuum

evacuated to 10^{-6} mbar and then filled with high purity argon. The final charge was collected at the cathode mesh plate placed 3 mm below the GEM using a charge sensitive pre-amplifier.

A total distance of 6 mm was used between the anode/cathode plane of the THCOBRA and the top surface of the GEM were the CsI photocathode was deposited.

6.4.1 Results in Argon

The results obtained in Argon are presented in the chart of figure 6.11:

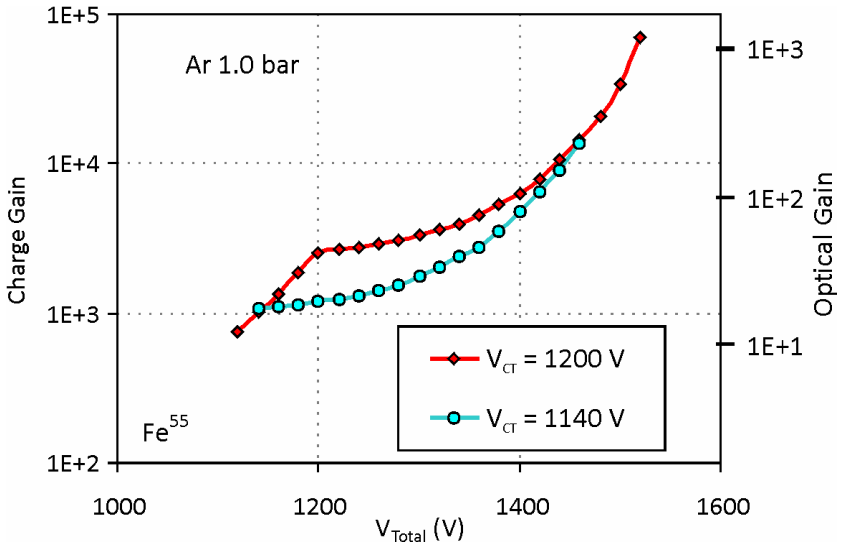

Figure 6.11 - Charge and optical gain measured of the PACEM detector operating with a THCOBRA as the first element of the cascade, for different values of $V_{C\text{-}T}$. The PACEM detector was composed by the THCOBRA and GEM and the signal was measured at the cathode mesh, placed 3 mm under the GEM.

The detector was irradiated with the 5.9 keV X-rays from a Fe^{55} X-ray source, producing in average 215 ion/electron pairs for each event fully absorbed in the gas medium (table 2-1). The final charge was collected at the cathode mesh, placed 3 mm distance from the bottom electrode of the GEM. The induction field in this region was of 2.0 kV×cm^{-1}, a value below the ionisation threshold for Argon [21]. The gain of the detector was changed by first raising the $V_{C\text{-}T}$ voltage on the THCOBRA, up to the value indicated in the charts (corresponding to the inflection point in both curves) while

keeping $V_{A-C} = 0$ V. After this point, V_{C-T} was kept constant and V_{A-C} was raised until the limit imposed by the occurrence of discharges in the detector.

The voltage across the GEM was of 290 V, a value that corresponds roughly to a gain of ≈ 60 [102]. The optical gain presented in figure 6.11 (right axis) was calculated dividing the total gain of the PACEM detector (measured at the cathode mesh and also presented in figure 6.11, left axis) by the above mentioned GEM charge gain. The optical gain reached maximum values in the range 10^2-10^3, depending on the total voltage at the THCOBRA.

The behavior of the gain curves of the PACEM detector operating in pulse mode reflects the production of the secondary scintillation at the holes and between the anodes and cathodes of the THCOBRA. For $V_{A-C} = 0$ V (before the inflection point on the curves) the exponential increasing on the charge and optical gain with V_{C-T} reflects the avalanches that take place inside the holes of the THCOBRA. For low values of V_{A-C} (the points on the curves immediately after the inflection points) the electrons extracted from the holes of the THCOBRA drift to the anodes, without additional charge avalanche mechanisms. For these values of V_{A-C} the charge and optical gain of the PACEM detector only moderately increase with V_{TOTAL}. It is only for high values of V_{A-C} that the electric field intensity in the region between anodes and cathodes reaches values above the ionization threshold in argon and that the charge multiplication mechanisms start to take place, leading to an exponential increase in the optical gains and charge gain of the PACEM detector.

The high gains measured show that the THCOBRA can be efficiently incorporated in the PACEM detector and other gaseous detectors based on secondary scintillation mechanism.

6.5 Conclusions

On this chapter we've described a new THGEM-like thick hole-multiplier, which introduces the novelty of an additional patterned electrode on one of its faces. Charges are multiplied in the holes, with additional multiplication of the avalanche electrons on the region between the holes and the anode strips. Charge gains of 5×10^4 and of 6×10^4 were attained with 22.1 keV X-rays at atmospheric pressure in Ar and P10. Charge

gains of 10^5 were measured in Neon at 1.7 bar with UV photons, in current mode. An energy resolution of 12.2% was obtained with 22.1 keV kα X-rays in P10.

These results indicate the possibility of reaching reasonable charge gains with robust single-element patterned hole-multiplier. One major advantage of the THCOBRA is the relatively low voltage required to obtain gains similar to the ones achieved with other thick electron multipliers operating at higher voltages. This feature can be of great interest in applications in dense gases (such as high-pressure and cryogenic detectors).

The use of the THCOBRA as the first element of the PACEM demonstrates also the advantage of having high charge gains and, therefore high scintillation gains, important to achieve high optical gains.

Similarly to the standard MHSP, the THCOBRA, can operate as a standalone detector or can be incorporated in a cascade of electron multipliers. Applications of this device to the ion back-flow reduction in cascaded gaseous multipliers are currently underway [108] with the operation of the THCOBRA in reverse mode.

7 FINAL CONCLUSIONS

We've developed a set of techniques for the reduction of the ion back flow in cascaded gaseous detectors that take advantage of the properties of the Micro Hole and Strip Plate. On a first approach the MHSP was operated in reverse mode and placed as the first element of a cascade of gaseous electron multipliers. The thin anode strips were polarized at lower voltage than that of the thicker cathodes and acted as collecting electrodes for the ions produced in the following stages of the cascade. A first setup, comprising only of one R-MHSP, was implemented resulting in excellent ion suppression but at the cost of poor electron transparency due to the high requirements on the voltage difference between the thinner and thicker strips necessary for efficient ion blocking. This requirement was partially relieved with the inclusion of another R-MHSP in the detector that allowed the reduction of the voltage difference between anodes and cathodes with a consequent increase on the electron transparency of R-MHSP. The IBF achieved in this configuration was reduced to 0.0006, by polarization of the anode strips of the R-MHSP with -80 V relatively to the thicker cathode strips. Despite the record breaking values obtained these were achieved for low voltages at the holes of the R-MHSP, corresponding to gain of only 0.6. At the time of these measurements the lack of good quality MHSP prevented us from completing the studies and operating the R-MHSP at higher voltages across the holes. The work that we've started was later completed and expanded with the operation of the F-R-MHSP that led to improved ion back-flow suppression and finally to the long awaited operation of high gain GPM sensitive to the visible region of the spectra.

Following the R-MHSP studies we've decided to follow a different line of approach and innovated once again by developing a detector based on the secondary scintillation mechanisms on the MHSP when operated in pure noble gases. The PACEM detector uses the electroluminescence produced along the electron avalanches on the MHSP to propagate the signal through the detector. The MHSP is employed as the first element of the detector being separated from the remaining elements by a metallic mesh that completely blocks both the electrons and ions while allowing the passage of the emitted photons. These photons promote the extraction of photoelectrons from a CsI reflective photocathode deposited on the top electrode of the next element of the cascade.These photoelectrons are further multiplied until they are finally collected at the anode of the detector. We've operated the PACEM detector in xenon and confirmed the efficiency in the transmission of the signal by means of the electroluminescence, achieving optical gains of 80 without any degradation on the energy resolution measured for 5.9 keV X-rays. Once the PACEM concept was demonstrated we've focused on optimizing the optical gain and in measuring the number of ions produced on the MHSP that reached the sensitive region of the detector. Several gas mixtures were successfully tested: xenon (at atmospheric pressure and at pressures up to 3 bar), CF_4 and Xe-CF_4 mixtures. The operation at high pressure has showed that optical gains above 10 were achievable at ≈ 3 bar with a strong decrease in the number of ions reaching the drift region of the detector, of only 2 for each primary electron. The operation in CF_4 resulted, despite the lower scintillation yield of this gas, in similar optical gains as the ones achieved in xenon, due to the increase in the photoelectron extraction efficiency in this gas. The operation in xenon-CF_4 mixtures demonstrated that, for the same charge gain, there was an increase in the optical gain of the PACEM relative to the operation in pure xenon, with the addition of CF_4 in the mixtures.

The concept of the PACEM was extended with the development of the zero IBF detector, a detector were the MHSP is replaced by an electroluminescence gap without any charge avalanche: two parallel metallic grids defining a region of the detector with an electric field between the thresholds for scintillation and ionization in the gas, in this case, xenon. The electrons drifting in this region emit secondary scintillation that, similarly to the PACEM, is read by a reflective CsI photocathode deposited on the first element of the remaining cascade. In the zero IBF detector no ions are produced that flow back to the sensitive region of the detector. The operation of the zero IBF detector

with a scintillation gap of 4 mm in xenon has showed that optical gains of 4 are achievable. These gains can be increased by enlarging the dimensions of the scintillation region and the area of the photocathode used.

Another exciting progress on this work was the development of a thick electron multiplier version of the MHSP. The operation of the THCOBRA demonstrated the possibility to individualize the electrodes of a THGEM and increase its charge gain with an additional charge multiplication stage. The operation of the THCOBRA was successfully tested in argon, neon and P10 with high charge gains (above 10^4) achieved in these gases. The high gains measured and the relatively large distances between the anodes and cathodes on the THCOBRA are an advantage and immediately suggested the application of the THCOBRA to the PACEM concept. The THCOBRA has operated efficiently as the first element of a PACEM detector, reaching optical gains above 100 in argon.

As future developments, the work done here regarding the PACEM concept will be continued and expanded. The implementation of a double PACEM, with 2 consecutive electroluminescence stages, will take place and the operation of such detector will be tested at high pressure, taking advantage of the lower voltages required to operate the PACEM and of the optical gains achieved at pressures above the atmospheric.

The work related with the THCOBRA will also be continued. The operation of this device at high counting rate and its signal characteristics will be evaluated. The incorporation of the THCOBRA on the PACEM detector will continue, with the evaluation of the IBF and optical gain achievable in other gas mixtures.

The developments done in this work are passive of being incorporated in the plans for the future development of high energy physics detectors (TPC and calorimeters) based on the electroluminescence of noble gases [109]. The zero IBF detector, with its full ion backflow suppression, and the THCOBRA, due to its high optical gain, are natural candidates to the implementation of such devices.

8 BIBLIOGRAPHY

[1] M. Salete S.C.P. Leite "Radioluminescence of Rare Gases" Portgal. Phys. vol. 11, fasc. 1-2 (1980) 53-100.

[2] XCOM: Photon Cross Sections Database, NIST Standard Reference Database. http://www.nist.gov/physlab/data/xcom/index.cfm.

[3] Glenn F. Knoll "Radiation Detection and Measurement" 2nd Edition, John Wiley & Sons, 1989.

[4] X-RAY DATA BOOKLET, Center for X-ray Optics and Advanced Light Source, Lawrence Berkeley National Laboratory, 2001.

[5] Ix-B García Ferreira, J García Herrera and L Villaseñor "The Drift Chambers Handbook, introductory laboratory course (based on, and adapted from, A H Walenta's course notes)" Journal of Physics: Conference Series 18 (2005) 346–361.

[6] B. Saudolet "Fundamental processes in Drift Chambers" Physica Scripta vol. 23 (1981) 434-445.

[7] Masayo Suzuki, Shinzou Kubota "Mechanism of Proportional Scintillation in Argon, Krypton and Xenon" Nuclear Instruments and Methods in Physics Research 164 (1979) 197-199.

[8] C. A. N. Conde, A. J. P. L. Policarpo "A gas proportional scintillation counter" Nuclear Instruments and Methods 53 (July 1967) 7-12.

[9] Policarpo A. J., Alves M. A. F., Conde C. A. N. "Argon-Nitrogen Proportional Scintillation Counter" Nuclear Instruments and Methods 55 (1967) 105.

[10] J. M. F. Dos Santos, A. C. S. S. Bento, C. A. N. Conde "A simple, inexpensive gas proportional scintillation counter for x-ray fluorescence analysis" X-Ray Spectrometry vol. 22-4 (1993) 328-331.

[11] J. F. C. A. Veloso, J. M. F dos Santos, C. A. N. Conde "Gas proportional scintillation counters with a CsI-covered microstrip plate UV photosensor for high-resolution X-ray spectrometry" Nuclear Instruments and Methods in Physics Research A 457 (2001) 253-261.

[12] M. Alegria Feio, A. J. P. L. Policarpo, M. A. F. Alves "Thresholds for secondary light emission by noble gases" Japanese Journal of Applied Physics vol. 21- 8 (1982).

[13] D.E. Cumpstey, D.G. Vass "The Scintillation Process in Gas Proportional Scintillation Detectors with Uniform Electric Fields" Nuclear Instruments and Methods in Physics Research 171 (1980) 473-478.

[14] T.H.V.T. Dias, F.P. Santos, A.D. Staufer, C.A.N. Conde "Monte Carlo Simulation of x-ray absorption and electron drift in gaseous xenon" Physical Review A vol. 48-4 (1993).

[15] A. J. P. L. Policarpo "Light Production and Gaseous Detectors" Physica Scripta vol. 23 (1981) 539-549.

[16] H. M. Anderson "Xenon 147-nm resonance f value and trapped decay rates" Physical Review A vol. 51- 1 (January 1995) 211-217.

[17] H. Lange, F. Leipold "Effective Radiative Lifetimes" Contrib. Plasma Phys. vol. 37-4 (1997) 377-387.

[18] C.M.B. Monteiro, L.M.P. Fernandes, J.A.M. Lopes, L.C.C. Coelho, J.F.C.A. Veloso, J.M.F. dos Santos, K. Giboni, E. Aprille "Secondary scintillation yield in pure xenon" JINST 2 P05001 (2007).

[19] Tetsuhiko Takahashi, Susumu Himi, Masayo Suzuki, Jian-zhi Ruan, Shinzou Kubota "Emission Spectra form Ar-Xe, Ar-Kr, Ar-N_2, Ar-CH_4, Ar-CO_2 And Xe-N_2 Gas Scintillation Proportional Counters" Nuclear Instruments and Methods in Physics Research A 205 (1983) 591-596.

[20] F.I.G.M Borges, J.M.F. dos Santos, T.H.V.T. Dias, F.P. Santos, P.J.B.M. Rachinhas, C.A.N. Conde "Operation of gas proportional scintillation counters in a low charge multiplication regime" Nuclear Instruments and Methods in Physics Research A 422 (1999) 321-325.

[21] C.M.B. Monteiro, J.A.M. Lopes, J.F.C.A. Veloso, J.M.F. dos Santos "Secondary scintillation yield in pure argon" Physics Letters B 668 (2008) 167–170.

[22] http://hyperphysics.phy-astr.gsu.edu/hbase/tables/photoelec.html.

[23] William R. Leo "Techniques for Nuclear and Particle Physics Experiments" Springer-Verlag, 1987.

[24] Michael T. Ronan "Early TPC History and Recent Developments" Second "Rare-Event" TPC Workshop Paris, 20-21 Dec. 2004.

[25] D. Attié "TPC review" Nuclear Instruments and Methods in Physics Research A 598 (2009) 89–93.

[26] CERN Courier vol. 46 no. 6: July/August 2006.

[27] A. Bagulya, A. Blondel, S. Borghi, G. Catanesi, P. Chimenti, U. Gastaldi, S. Giani, V. Grichine, V. Ivanchenko, D. Kolev, J. Panman, E. Radicioni, R. Tsenovg and I. Tsukermanh "Dynamic distortions in the HARP TPC: observations, measurements, modelling and corrections" 2009 JINST4 P11014.

[28] D. Friedrich, G. Melchart, B. Saudolet, F. Sauli "Positive Ion Effects in Large-Volume Drift Chambers" Nuclear Instruments and Methods in Physics Research 158 (1979) 81-88.

[29] F. Sauli. "GEM: A new concept for electron amplification in gas detectors" Nuclear Instruments and Methods A 386 (1997) 53 l-534.

[30] CERN Gas Detectors Development Group, http://gdd.web.cern.ch/GDD/

[31] Thomas Hott "MSGC development for the Inner Tracker of HERA-B" Nuclear Instruments and Methods A 408 (1998) 258-265.

[32] A. Bressan, A. Buzulutskov, L. Ropelewski, F. Sauli, L. Shekhtman "High gain operation of GEM in pure argon" Nuclear Instruments and Methods in Physics Research A 423 (1999) 119-124.

[33] A. Breskin, T. Boutboul, A. Buzulutskov, R. Chechik, G. Garty, E. Shefer, B.K. Singh "Advances in gas avalanche photomultipliers" Nuclear Instruments and Methods in Physics Research A 442 (2000) 58-67.

[34] D. Mörmann, A. Breskin, R. Chechik, P. Cwetanski, B.K. Singh "A gas avalanche photomultiplier with a CsI-coated GEM" Nuclear Instruments and Methods in Physics Research A 478 (2002) 230–234.

[35] A. F. Buzulutskov "Physics of multi-GEM structures" Nuclear Instruments and Methods in Physics Research A 494 (2002) 1648-155.

[36] D. Mormann, A. Breskin, R. Chechik, D. Bloch "Evaluation and reduction of ion back-flow in multi-GEM detectors" Nuclear Instruments and Methods in Physics Research A 516 (2004) 315–326.

[37] A. Bondar, A. Buzulutskov, L. Shekhtman, A. Vasiljev "Study of ion feedback in multi-GEM structures" Nuclear Instruments and Methods in Physics Research A 496 (2003) 325–332.

[38] J. F. C. A. Veloso, J. M. F. dos Santos, C. A. N. Conde, "A proposed new microstructure for gás radiation detectors: The microhole and strip plate" Rev. Sci. Instrum. vol. 71 (2000) 2371-2376.

[39] J.F.C.A. Veloso, J.M. Maia, L.F. Requicha Ferreira, J.M.F. dos Santos, A. Breskin, R. Chechik, Rui de Oliveira "Recent advances in X-ray detection with micro-hole and strip plate detector" Nuclear Instruments and Methods in Physics Research A 524 (2004) 124–129.

[40] J. M. Maia, D. Mörmann, A. Breskin, R. Chechik, J. F. C. A. Veloso, and J. M. F. dos Santos "Progress in MHSP Electron Multiplier Operation" IEEE Transactions On Nuclear Science vol. 51- 4 (2004) 1503-1508.

[41] J.M. Maia, D. Mörmann, A. Breskin, R. Chechik, J.F.C.A. Veloso, J.M.F. dos Santos "Avalanche-ion back-flow reduction in gaseous electron multipliers

based on GEM/MHSP" Nuclear Instruments and Methods in Physics Research A 523 (2004) 334–344.

[42] Pedro Hugo Ferreira Natal da Luz "Development of neutron and X-ray imaging detectors based on MHSP" PhD Thesis, Aveiro University, 2009.

[43] J.F.C.A. Veloso, F. D. Amaro, J.M.F dos Santos, A. Breskin, A. Lyashenko, R. Chechik "The Photon-Assisted Cascaded Electron Multiplier: a concept for potential avalanche-ion blocking" JINST 1 P08003.

[44] J.F.C.A. Veloso, F. D. Amaro, J.M. Maia, A. Breskin, A. Lyashenko, R. Chechik, J.M.F dos Santos, O. Bouianov, M. Bouianov "MHSP in reversed-bias operation mode for ion blocking in gas-avalanche multipliers" Nuclear Instruments and Methods in Physics Research A 548 (2005) 375–382.

[45] J.F.C.A. Veloso, C.C. Caldas, C.A.B. Oliveira, C.D.R. Azevedo, J.M.F. dos Santos, A. Breskin, R. Chechik ,"High-rate operation of the Micro-Hole and Strip Plate gas detector" Nuclear Instruments and Methods in Physics Research A 580 (2007) 362-365.

[46] F.D. Amaro, J.F.C.A. Veloso, A. Breskin, R. Chechik and J.M.F. dos Santos," Operation of MHSP multipliers in high pressure pure noble-gas" 2006 JINST 1 P04003.

[47] R. Chechik, A. Breskin, C. Shalem, D. Mörmann "Thick GEM-like hole multipliers: properties and possible applications" Nuclear Instruments and Methods in Physics Research A 535 (2004) 303-308.

[48] C. Shalem, R. Chechik, A. Breskin, K. Michaeli "Advances in Thick GEM-like gaseous electron multipliers—Part I: atmospheric pressure operation" Nuclear Instruments and Methods in Physics Research A 558 (2006) 475–489.

[49] M. Cortesi, R. Alon, R. Chechik, A. Breskin, D. Vartsky, V. Dangendorf "Investigations of a THGEM-based Imaging Detector" 2007 JINST 2 P09002.

[50] R. Alon, J. Myamoto, M. Cortesi, A. Breskin, R. Chechick, I. Carne, J.M. Maia, J.M.F. dos Santos, M. Gai, D. McKinsey, V. Dangerdorf "Operation of a Thick Gas Electron Multiplier (THGEM) in Ar, Xe and Ar-Xe" JINST 3 P01005 (2008).

[51] A. Breskin, R. Alon, M. Cortesi, R. Chechik, J. Myamoto, V. Dangendorf, J.M. Maia, J.M.F. dos Santos "A Concise Review on THGEM Detectors" Nuclear Instruments and Methods in Physics Research A 598 (2009) 107-111.

[52] Derek L. Livesey "Atomic and Nuclear Physics" Blaisdell Publishing Company, 1966.

[53] W.E. Spicer, A. Herrera-Gómez "Modern Theory and Applications of Photocathodes" SLAC-PUB-6306 (1993).

[54] P. Miné "Photoemissive materials and their application to gaseous detectors" Nucl. Instrum. Meth. A 343 (1994) 99-108.

[55] A. Breskin "CsI UV photocathodes: history and mystery" Nuclear Instruments and Methods in Physics Research A 371 (1996) 116-136.

[56] C. Lu, K.T McDonald "Properties of reflective and semitransparent CsI photocathodes" Nucl. Instrum. Meth. A 343 (1994) 135-151.

[57] A. Breskin, R. Chechik, D. Vartsky, G. Malamud, P. Miné "A correction of the quantum efficiency of CsI and other photocathodes due to the recalibration of the reference photomultipliers" Nuclear Instruments and Methods A 343 (1994) 159-162.

[58] L. Periale, V. Peskov, C. Iacobeus, T. Francke, B. Lund-Jensen, N. Pavlopoulos, P. Picchi, F. Pietropaolo "The development of gaseous detectors with solid photocathodes for low temperature applications" Nuclear Instruments and Methods in Physics Research A 535 (2004) 517-522.

[59] L. Periale, V. Peskov, A. Braem, Di Mauro, P. Martinengo, P. Picchi, F. Pietropaolo, H. Sipila "Development of new sealed UV sensitive gaseous detectors and their applications" Nuclear Instruments and Methods in Physics Research A 572 (2007) 189–192.

[60] F. Piuz "CsI Photocathode and RICH detector" Nuclear Instruments and Methods in Physics Research A 371 (1996) 96–115.

[61] A. F. Buzulutskov "Gaseous Photodetectors with Solid Photocathodes" Physics of Particles and Nuclei vol. 39-3 (2008) 424–453.

[62] A. Breskin, A. Buzulutskov, R.Chechik, A. Di Mauro, E. Nappi, G. Paic, F. Piuz "Field-dependent photoelectron extraction from CsI in different gases" Nuclear Instruments and Methods in Physics Research A 367 (1995) 342-346.

[63] A. Di Mauro, E. Nappi, F. Posa, A. Breskin, A. Buzulutskov, R. Chechik, A. S.F. Biagi, G. Paic, F. Piuz "Photoelectron Backscattering effects in photoemission form CsI into gas media" Nuclear Instruments and Methods in Physics Research A 371 (1996) 137-142.

[64] J. Escada, P. J. B. M. Rachinhas, T. H. V. T. Dias, J. A. M. Lopes, F. P. Santos, C. A. N. Conde, A. D. Stauffer "Photoelectron Collection Efficiency in Xe-CF4 Mixtures" 27 October – 3 November, Honolulu, Hawaii, U.S.A., IEEE Nucl. Sci. Symp. Med. Image Conf. 1 (2007) 585.

[65] A. Breskin, A. Buzulustkov, R. Chechik "GEM photomultiplier operation in CF_4" Nuclear Instruments and Methods in Physics Research A 483 (2002) 670.

[66] L.C.C. Coelho, H.M.N.B.L. Ferreira, J.A.M. Lopes, T.H.V.T. Dias, L.F.R. Ferreira, J.M.F. dos Santos, A. Breskin, R. Chechik "Measurement of the photoelectron-collection efficiency in noble gases and methane" Nuclear Instruments and Methods in Physics Research A 581 (2007) 190–193.

[67] A. Breskin, A. Buzulutskov, R. Chechik, G.Garty, F.Sauli, L.Shekhtman "The CsI Multi-GEM Photomultiplier" Proc. of the Int. Workshop on Micro-pattern Gas Detectors, Orsay France, June 1999, 107

[68] A. Buzulutskov, A. Breskin, R. Chechik, G. Garty, F. Sauli, L. Shekhtman "The GEM photomultiplier operated with noble gas mixtures" Nuclear Instruments and Methods in Physics Research A 443 (2000) 164-180.

[69] R. Chechik, A. Breskin, G.P. Guedes, D. Mormann, J.M. Maia, V. Dangendorf. D. Vartsky, J.M.F. dos Santos, J.F.C.A Veloso "Recent Investigations of Cascaded GEM and MHSP detectors" IEEE Trans. Nucl. Sci. 51 (2004) 2097-2103.

[70] Dirk Mormann "Study of novel gaseous photomultipliers for UV and visible light" PhD Thesis, Weizmann Institute of Science, Rehovot, Israel, June 2005.

[71] D. Mormann, A. Breskin, R. Chechik, B.K. Singh "On the efficient operation of a CsI-coated GEM photon detector" Nuclear Instruments and Methods in Physics Research A 471 (2001) 333–339.

[72] G. Charpak "Electronic Imaging of Ionizing Radiation with Limited Avalanches In Gases" Noble Lecture, December 8 1992.

[73] F. Sauli, L. Ropelewski and P. Everaerts "Ion Feedback Suppression in Time Projection Chambers" Nuclear Instruments and Methods in Physics Research A 560, Issue 2, (2006) 269-277.

[74] Q. Weitzel, F. Bohmer, C. Hoppner, T. Huber, B. Ketzer, I. Konorov, A. Mann, S. Neubert, S. Paul and C. Simonetto "Development of a High-Rate GEM-Based TPC for PANDA" 2007 IEEE Nuclear Science Symposium Conference Record N12-1.

[75] A. Breskin, D. Mörmann, A. Lyashenko, R. Chechik, F.D. Amaro, J.M. Maia, J.F.C.A. Veloso, J.M.F. dos Santos "Ion-induced effects in GEM & GEM/MHSP gaseous photomultipliers for the UV and the visible spectral range" Nucl. Instrum. Meth. A 553 (2005) 46.

[76] A.V. Lyashenko, A. Breskin, R. Chechik, J.F.C.A. Veloso, J.M.F. Dos Santos, F.D. Amaro "Advances in ion back-flow reduction in cascaded gaseous electron multipliers incorporating R-MHSP elements" 2006 JINST 1 P10004.

[77] A. Breskin, A.Lyashenko, R.Chechik, F.D.Amaro, J.Veloso, J.M.F. Dos Santos "Progress in gaseous photomultipliers for the visible spectral range" Nuclear Instruments and Methods in Physics Research A, in press.

[78] A.V. Lyashenko, A. Breskin, R. Chechik, J.F.C.A. Veloso, J.M.F. Dos Santos, F.D. Amaro "Development of high-gain gaseous photomultipliers for the visible spectral range" 2009 JINST 4 P07005.

[79] A. Buzulutskov, A. Bondar "Electric and Photoelectric Gates for ion backflow in multi-GEM structures" Journal of Instrumentation 1 P08006, 2006.

[80] TRA-CON, Ellsworth Adhesives.

[81] F. Fernandez-Lima, V.M. Collado, C.R. Ponciano, L.S. Farenzena, E. Pedrero, E.F. da Silveira "Laser ablation of CsI analyzed by delayed extraction" Applied Surface Science 217 (2003) 202–209.

[82] S. Roth "Charge transfer of GEM structures in high magnetic fields" Nuclear Instruments and Methods in Physics Research A 535 (2004) 330-333.

[83] R. Bellazzini, M. A. Spezziga "Electric Field, Avalanche Growth and Signal Development in Micro-Strip Gas Chambers and Micro-Gap Chambers" Rivista del Nuovo Cimento vol.17-12 (1994).

[84] J. Va'vra "Photon detectors" Nuclear Instruments and Methods in Physics Research A, vol. 371 (1996) 33-56.

[85] Sven Lotze "Ion Backdrift Minimization in a GEM-based TPC readout" PhD Thesis, RWTH Aachen, 2006.

[86] A.V. Lyashenko, A. Breskin, R. Chechik, J.F.C.A. Veloso, J.M.F. Dos Santos, F.D. Amaro "Further progress in ion back-flow reduction with patterned gaseous hole - multipliers" 2007 JINST 2 P08004.

[87] Alexey Lyashenko "Development of gas-avalanche photomultipliers sensitive in the visible spectral range" PhD thesis (2009) Weizmann Institute of Science, Rehovot, Israel.

[88] A. Lyashenko, A. Breskin, R. Chechik, F.D. Amaro, J.F.C.A. Veloso, J.M.F. Dos Santos "High-gain DC-mode operated Gaseous Photomultipliers for the visible spectral range", Nuclear Instruments and Methods in Physics Research A 610 (2009) 161-163.

[89] H. Natal da Luz, J.F.C.A. Veloso, F.D. Amaro, L.F. Requicha Ferreira, J.M.F. dos Santos, A Breskin, R. Chechik "MHSP operation in pure xenon" Nuclear Instruments and Methods in Physics Research A 552 (2005) 259-262.

[90] F.D. Amaro, J.F.C.A. Veloso, A. Breskin, R. Chechik, J.M.F. Dos Santos "Operation of MHSP multipliers in high pressure pure noble-gas" Journal of Instrumentation 1 P04003 (2006).

[91] V. A. Alekseev "Vacuum Ultraviolet Absorption in Xe + CF_4 and Kr + CF_4 Mixtures" Optics and Spectroscopy, Vol. 96, No. 4, 2004, pp. 492-496.

[92] A. Pansky, A. Breskin, A. Buzulutskov, R. Chechik, V. Elkind, J. Va'vra "The Scintillation of CF_4 and its relevance to detection science" Nuclear Instruments and Methods in Physics Research A 354 (1995) 262-269.

[93] A. Morozov, M.M.F.R. Fraga, L. Pereira, L.M.S. Margato, S.T.G. Fetal, B. Guerard, G. Manzin, F.A.F. Fraga "Photon yield for ultraviolet and visible emission from CF_4 excited with a-particles" Nuclear Instruments and Methods in Physics Research B 268 (2010) 1456–1459.

[94] Hugo Natal da Luz, Ana S. Conceição, Joao F.C.A. Veloso, Joaquim M.F. dos Santos, Antonio C.S.S.M. Bento, Jamil A. Mir, Luis F. Requicha Ferreira "GEM operation in CF4: studies of charge and scintillation properties" 2008 IEEE Nuclear Science Symposium Conference Record.

[95] C. Broggini "Detection of the scintillation light induced by α particles in pure CF_4" Nuclear Instruments and Methods in Physics Research A 361 (1995) 543-547.

[96] K. A. Blanks, K. Becker "Optical emissions in the wavelength region 2000-6000 produced by electron impact dissociation of NF_4, CF_4 and SF_4" J. Phys. B: At. Mol. Phys. 20 (1987) 6157-6163.

[97] J. E. Hesser, Kurt Dressler "Radiative Lifetimes of Ultraviolet Emission systems excited in BF_3, CF_4 and SiF_4" The Journal of Chemical Physics 47-9 (1967) 3443-3450.

[98] R. Gernhauser, B. Bauer, J. Friese, J. Homolka, A. Kastenmiiller, P. Kienle, H.-J. Krner, P. Maier-Komor, M. Miinch, R. Schneider, K. Zeitelhack "Photon detector performance and radiator scintillation in the HADES RICH" Nuclear Instruments and Methods in Physics Research A 371 pp. 300-304, 1996.

[99] H. Natal da Luz, J. A. Mir, J. F. C. A. Veloso, J. M. F. dos Santos, N. J. Rhodes, E. M. Schooneveld "Micro-Hole and Strip Plate (MHSP) operation in CF_4" Nuclear Instruments and Methods in Physics Research A 580-1 (2007) 286-288.

[100] M. Deptuch, T. Z. Kowalski "Gas multiplication process in mixtures based on Ar, CO2, CF4" Nuclear Instruments and Methods in Physics Research A 572 (2007) 184–186.

[101] D. Mörmann, M. Balcerzyk, A. Breskin, R. Chechik, B.K. Singh, A. Buzulutskov "GEM-based gaseous photomultipliers for UV and visible photon imaging" Nuclear Instruments and Methods in Physics Research A 504 (2003) 93-98.

[102] F.D. Amaro, A.S. Conceição, J.F.C.A. Veloso, L.C. Coelho, L.M.P. Fernandes, L.F. Requicha Ferreira, J.A.M. Lopes, and J.M.F. dos Santos "Operation of a single-GEM in noble gases at high pressures" Nuclear Instruments and Methods in Physics Research Section A, vol. 579 (2007) 62-66.

[103] A. Bondar, A. Buzulutskov, L. Shekhtman "High pressure operation of the triple-GEM detector in pure Ne, Ar and Xe" Nuclear Instruments and Methods in Physics Research A 481 (2002) 200-203.

[104] Garfield – simulation of gaseous detectors. http://garfield.web.cern.ch/garfield

[105] MAXWELL 3D Version 10, Ansoft Corporation. Pittsburg, PA, U.S.A.

[106] M. Cortesi, V. Peskov, G. Bartesaghi, J. Myamoto, S. Cohen, R. Chechik, J.M. Maia, J.M.F. dos Santos, G. Gambarini, V. Dangendorf, A. Breskin "THGEM Operation in Ne and Ne/CH_4" 2009 JINST 4 P08001.

[107] F. Sauli "Gas detectors: achievements and trends" Nuclear Instruments and Methods in Physics Research A 461 (2001) 47-54.

[108] J.F.C.A. Veloso, C. Santos, F. Pereira, C. Azevedo, F.D. Amaro, J.M.F. dos Santos, A. Breskin, R. Chechik "Ion Back Flow Reduction in THGEM Cascades using a THCOBRA" 5th RD51 Collaboration Meeting, Friburg, Germany 2010.

[109] Markus Ball, F. D. Amaro, P. Bechtle, J. Kaminski, T. Lux, J.M.F. dos Santos "A common proposal for an electroluminescence TPC and tracking calorimeter", submitted for funding to Marie Curie Projects.